Reduced Model for Particle Laden Flow

by

Junjie Zhou

B.S., Mechanical Engineering

Cornell University, 2003

Submitted to the Department of Mechanical Engineering
in partial fulfillment of the requirements for the degree of

Master of Science in Mechanical Engineering

at the

MASSACHUSETTS INSTITUTE OF TECHNOLOGY

June 2004

Author . . . .
Department of Mechanical Engineering
May 7, 2004

Certified by . . . .
Anette Hosoi
Assistant Professor of Mechanical Engineering
Thesis Supervisor

Accepted by . . . .
Ain Sonin
Chairman, Department Committee on Graduate Students

Reduced Model for Particle Laden Flow

by

Junjie Zhou

Submitted to the Department of Mechanical Engineering
on May 7, 2004, in partial fulfillment of the
requirements for the degree of
Master of Science in Mechanical Engineering

Abstract

The flow of thin liquid films on solid surfaces is a significant phenomenon in nature and in industrial processes where uniformity and completeness of wetting are paramount in importance. It is well known that when a clear viscous fluid flows down an inclined surface under gravity, after some time, the initially straight contact line becomes unstable with respect to transverse perturbations. Clear fluid is easier to use in experiments, but industrial processes usually involve particulates in the form of either suspensions or dry granular flows.

In this work, we study the flow of a thin film down an inclined plane. The particle-fluid mixture is modeled as a single fluid with effective density and viscosity, depending on the concentration of the particles. Since the flow is slow and the fluid layer is very thin, inertial effects are ignored and a lubrication approximation is applied to simplify the analysis. It is assumed that there is no variation in the transverse direction before the onset of instability, and the fluid properties and velocity are depth averaged to remove the height-dependence. The settling velocity of the particles is hindered by the presence of neighboring particles; this phenomenon is captured by the hindered velocity function that decreases with increasing concentration. The normal component of the settling velocity is neglected in this work and the resulting model is a system of two equations accounting for the film thickness and particle concentration changes as the mixture flows down the plane.

Numerical simulations are performed and it is found that the mixtures with higher concentration flow more slowly. Compared to the clear viscous fluid, particle laden flow results in a bump that is much bigger and the size of the bump increases with concentration. We also observe that the front edge of the bump travels faster than the trailing edge and the bump width increases. Numerical simulations reveal that an intermediate plateau structure due to the presence of particles is formed behind the smaller bump due to surface tension. This intermediate state depends on the inclination angle and the initial concentration. When the higher order terms in our derived model are dropped, we discover that the resulting reduced model is still able to capture the bulk characteristics of the flow. The reduced model is a 2X2 system of conservation laws, in which the solutions can be obtained through classical shock theory analysis. It is found that our system involves a 1-shock at the trailing edge connected by an intermediate state to a 2-shock at the leading edge. The intermediate state as well as the shock speeds can be solved by shock theory analysis, and their values are found to agree very well with the simulations.

Thesis Supervisor: Anette Hosoi
Title: Assistant Professor of Mechanical Engineering

Acknowledgments

I would like to thank the following people for their help in the creation of this thesis from the research to the final formulation.

First and formost, I would like to express my deepest gratitude and appreciation to my thesis advisor Prof. Anette Hosoi for introducing me to the subject and for sharing with me her vast knowledge. She provided a motivating and enthusiastic atmosphere during the discussions I had with her. It was a great pleasure to conduct this thesis under her supervision.

I am highly indebted to Prof. Andrea Bertozzi, Professor at University of California, Los Angeles. During many phone conservations we had in the course of this work, I received valuable suggestions and guidance on solving system of conservation laws from her. This thesis certainly would not be possible without her help.

Needless to say, I am grateful to my fellow colleagues in the research group. Their hospitality has made my stay in MIT a pleasant one. Special thanks to Benjamin Dupuy for sharing with me his experimental results and knowledge on this particular research problem.

I would also like to thank my parents for their love and endless support throughout the year.

Contents

List of Figures

List of Tables

Chapter 1

Introduction

The flow of thin films is relevant in a number of different fields, such as microchip production, the lining of mammalian lungs, and the flow of surface active materials. Such "coating" flow is also relevant to painting and to situations in which thin liquid layers are used to maximize heat or mass transfer across an interface. In the case of granular flow and suspension flow (particle laden flow), thin films are often encountered in geophysical situations such as avalanches and landslides. These flows can be driven by gravitational (flow down an incline plane), centrifugal (spin coating), or Marangoni forces. In all of these different settings, the front dynamics are not completely understood. In many situations, the fluid fronts become unstable, leading to finger-like rivulets, triangular saw-tooth patterns or, in the case of surfactant flow, dentritic tip-splitting petals. These instabilities are often undesirable in technological applications, since they may lead to the formation of dry regions. From a more fundamental viewpoint, one wishes to understand the dynamics of these strongly nonlinear systems, and reach general conclusions concerning instabilities.

In this work, we concentrate on the flow of a thin film of particle-fluid mixture flowing down an inclined plane under gravity. There have been extensive studies, experimentally, theoretically or numerically, on clear viscous thin film flowing down an inclined surface under gravity. Although some of the issues still remain to be understood, many interesting features of the flow have been found and successfully explained. On the other hand, people have also looked into granular flows and found that granular thin films exhibit similar behaviors to the viscous fluid in terms of leading edge instability. There are also unique features associated with dry granular flows.

Since granular materials and viscous fluid exhibit both similar and distinct behaviors when they flow down an inclined surface under gravity, it is interesting to examine a regime where particles and viscous fluid flow down together in the form of a well mixed suspension. In this chapter, we will first summarize some of the important results reported in previous studies on viscous fluid flows and granular flows.

1.1 Viscous Fluid Flow

The leading-edge instability of a sheet of viscous fluid moving under gravity down an inclined plane was first reported by Huppert [33]. When a fixed volume of fluid is spread uniformly across the plane and released, after the leading edge of the fluid has spread a certain distance down the plane, the edge spontaneously distorts in the spanwise direction. The structure of the distortion develops nonlinearly in two different ways as shown in Figure 1-1. For certain fluid-solid combinations, a series of straight rivulets or fingers of fairly uniform width is formed. These rivulets continue to grow downstream. However, the upslope troughs between the fingers stop and the regions between the fingers remain dry. In this scenario, the fluid never completely wets the surface. For other fluid-solid combinations, a sawtooth-like pattern is observed. In this case, both the downslope tips and the upslope troughs continue to flow downhill, although at different rates, and the surface is ultimately completely coated by the liquid [33].

During the initial stage, when the front is straight, the dynamics of the fluid in the thinning film is controlled by a balance between the viscous and gravitational forces. Using the lubrication approximation, neglecting surface tension and contact line effects, Huppert derived an expression for the film thickness prior to the onset of instability. He predicted that the position of the fluid front x_N advances like $t^{1/3}$ and

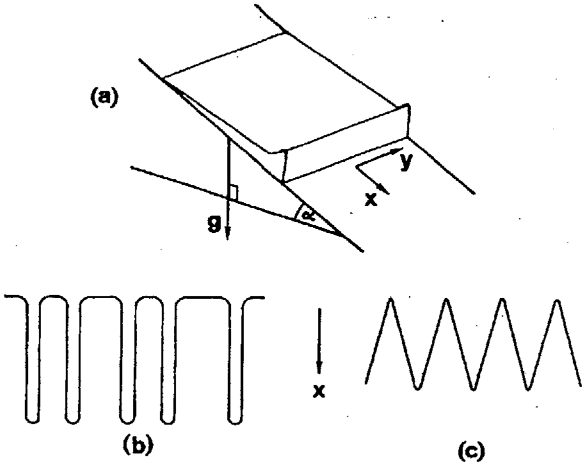

Figure 1-1: ***Top:*** *Sketch of the experimental setup and flow profile before the onset of instability.* ***Bottom left:*** *Parallel-sided finger pattern.* ***Bottom right:*** *Sawtooth-like pattern (Source: Jerret and de Bruyn [37])*

the height of the fluid front h_N varies like $t^{-1/2}$, where t is the time.

$$\begin{aligned} h_N &= (\nu/g\sin\alpha)^{1/2}x^{1/2}t^{-1/2} \\ x_N &= (9A^2g\sin\alpha/4\nu)^{1/3}t^{1/3} \end{aligned} \tag{1.1}$$

where A is the initial cross-sectional area of the fluid (and is therefore proportional to the fluid volume), α is the angle of inclination and g is the gravitational acceleration.

Experimental data shows that the wavelength of the instability is a function of surface tension, but it is independent of viscosity and is only weakly dependent on the initial cross-sectional area A. Based on scaling arguments, Huppert argued that the pattern wavelength λ is on the order of

$$\lambda \sim (A^{1/2}\sigma/\rho g\sin\alpha)^{1/3} \tag{1.2}$$

where σ is the surface tension and ρ is the density. His data is consistent with this relationship, with a constant of proportionality of 7.5. For the rivulet instability observed with glycerin, the position of the tips of the rivulets moves downhill like $t^{0.6}$, and the upslope troughs are virtually stationary. For the sawtooth pattern, the tips move like $t^{0.35}$ and troughs like $t^{0.28}$ [33].

Silvi and Dussan V [60] studied the same problem but with an emphasis on the contact line at the front of the advancing fluid. From Huppert's study, the contact line does not seem to be playing a role in the stability, since the value of λ does not depend on the value of the contact angle. Silicon oil and glycerin give rise to different fingering shapes in Huppert's experiment. However, since silicon oil and glycerin have significantly different contact angles on Perspex as well as viscosities, it is difficult to differentiate with certainty the effects caused by the surface tension from those caused by the contact angle. To differentiate, Silvi and Dussan performed experiments involving only one fluid, glycerin, flowing down glass and Plexiglas surfaces. Therefore, the contact angles between the liquid surface and the solid at the contact line are different in their two cases, but the fluid properties are fixed. They concluded that, while contact line effects are not the cause of the instability, they play an important role in selecting the ultimate flow pattern. For small contact angles, the instability develops into the sawtooth pattern and the fluid eventually wets the surface completely. For large contact angles, the rivulets pattern forms.

Schwartz [59] performed numerical simulations of the flow of a thin layer of viscous fluid down a plane, using equations derived in the lubrication approximation and including the effects of surface tension.

$$h_t = \nabla \cdot [h^3(\cos\alpha \nabla h - B^{-1}\nabla\nabla^2 h - \mathbf{i}\sin\alpha)] \tag{1.3}$$

Where the unit vector $\mathbf{i}$ points downhill. With L as the characteristic length, the inverse Bond number is defined as $B^{-1} = \sigma/(\rho g L^2)$. When a no-slip boundary condition is imposed at the edges of the plane (corresponding to the experimental constraint of a wall at the edges), Schwartz observed an instability of the contact line driven by the boundary conditions, which propagates inward from the edges and leads to the formation of more or less periodic fingers. The longest of these fingers is markedly wedge shaped, in agreement with experimental results for liquids that strongly wet the surface. The number of fingers formed is reduced with increasing surface tension.

In the absence of the no-slip condition, fingering can also result from the imposition of a small perturbation on the uniformly propagating two-dimensional flow down the plane. The disturbance first decays until the curvatures become sufficiently large at the front. Then lateral flow, caused by greater curvature, hence higher pressures resulting from surface tension, at the troughs, leads eventually to steady growth of the fingers. This behavior disappears if surface tension effects are neglected. This result confirms the prediction of Huppert that surface tension is the destabilizing force.

Schwartz concluded that fingering on a finite slope is an inherent phenomena caused by surface tension and that, even with perfect wetting, it must ultimately occur. For slopes less than vertical, without gross perturbations such as a confining side wall, some or all disturbances will first be damped. Eventually, however, the evolving profile will develop sufficiently high curvature at the moving front that small disturbances will initiate fingering.

Numerical Simulations by Schwartz reveal the fact that surface tension effects control the instability. Surface tension is irrelevant in the fluid region far from the front, but it dominates near the contact line. The mechanism for the instability actually involves a subtle interplay between these two regions. In his original work, Huppert only characterized the flow far from the front. Troian *et al.* [57] first described the surface tension dominated region at the contact line and presented a theoretical mechanism for the instability. The calculations of Troian *et al.* can be briefly summarized as follows. Working in the lubrication approximation, they calculated the flow profile in an outer region, away from the contact line, where surface tension effects are negligible. The resulting flow profile ends abruptly at position x_N, where the film has a thickness $H_N = 3x_N/2A$ as presented in Huppert's work. Here, A is the volume of fluid per unit length in the cross-slope direction. They then calculated a solution in the inner region, where surface tension must be included, and matched these two solutions away from the contact line. They set the contact line as the origin of the coordinate system and rescaled the height H as $H(x,y,t) = H_N(t)h(\xi,t)$. H_N is the height at the contact line $x = x_N$. The dimensionless length, ξ, is the distance along x measured from the contact line and scaled by $l = H(3Ca)^{-1/3}$. The capillary number is defined as $Ca = \mu U_0/\sigma \ll 1$, where μ is the viscosity and $U_0 = dx_N/dt$.

With these rescaling, Equation 1.3 becomes

$$h_t + h^2 h_x + \nabla \cdot [h^3 \nabla \nabla^2 h - \cot(\alpha)(3Ca)^{1/3} h^3 \nabla h] = 0 \tag{1.4}$$

Near the contact line, the dynamics must take into account the singularity which arises [14] [17] [27] because of the no-slip boundary condition. Two possible mechanisms can be applied to relieve the singularity: introduce a thin film ahead of the contact line [15] or replace the no-slip condition with slip at the contact line region [31]. Troian *et al.* chose to match the solution at the contact line region to a thin film of thickness bH_N, and they found a quasi-steady solution $h(\xi, t) = h_0(\xi)$.

$$h_0^2(1 - h_{0\xi\xi\xi}) = \frac{1 - b^3}{1 - b} - (1 + b)\frac{b}{h} \tag{1.5}$$

Solutions to the above equation show that height of the maximum is a weak (logarithmic) function of b.

Troian *et al.* went on to develop a stability analysis of solutions to the quasi-steady two-dimensional lubrication equations in the limit of small contact angle using long wave approximations. They found that the straight front is unstable to periodic perturbations over a range of wave numbers. The perturbations grow like $\exp(\beta\tau)$, where τ is the scaled time. The maximum growth rate corresponds to a pattern wavelength of $\lambda = 14l$. This value compares well with the value $\lambda = 18l$ estimated from Huppert's data. They also pointed out that the base state has, near the contact line, a thick "bump" that is responsible for the linear instability. These calculations are valid for small Ca, and are also restricted to films thin enough that $H_N/l \ll \tan\alpha$.

Let us take a closer look at Equation 1.4. $h^2 h_x$ is a convective term that reflects the quadratic dependence of the velocity on its height. The two other terms are diffusive and tend to flatten the profile. The inner region is a consequence of the competition between these two types of terms; as the convective term tends to form a shock, and the diffusive terms smooth it out. The "bump" is a consequence of the balance between curvature gradients and viscous stress.

In neither the analysis of Troian *et al.* nor the work of Schwartz was the macroscopically observable advancing contact angle used as a boundary condition in the determination of the shape of the free surface. Goodwin and Homsy [23] proposed a different scaling to allow one to prescribe a contact angle boundary condition. They also noted in their work that the scaling and boundary conditions chosen by Troian *et al.* caused problems involving three singularities at the origin (the contact line). A no-slip boundary condition implies that the shear stress at the plate grows as x^{-1} as the contact line is approached. The scalings also lead to a free surface with infinite slope at the contact line. Although Troian *et al.* circumvented the infinite rate of change of curvature singularity at the contact line as described previously by requiring that the free surface match a precursor film of finite thickness at the apparent contact line, the resulting solution depends upon a modeling parameter which cannot be determined a priori.

Goodwin and Homsy again chose the characteristic length scale normal to the slope to be h_N. However, they scaled the down-slope coordinates as $x\ h_N/\tan(\phi)$. Also, they followed Greenspan [24] and replaced the no-slip boundary condition with a Navier-like slip model. The slip velocity was taken to be proportional to the product of the velocity gradient at the wall and a function $S(h)$, which depends on the local thickness of the fluid.

$$u = \frac{S(h)}{3}\frac{\partial u}{\partial y} - (\frac{1+S(h)}{3}), \quad \text{at} \quad y=0 \tag{1.6}$$

They arrived at the following differential equation for the shape of the free surface:

$$h_{xxx} = \{[1+S(h)]/[S(h)h+h^2]\} - 1 \tag{1.7}$$

Through the choice of $S(h)$ which is $O(h^{-1})$, as $h \to 0$ they could eliminate the stress singularity at the contact line. However, this model still has a singularity in the rate of change of curvature at the contact line. They concluded that the flow near the contact line cannot be modeled by the lubrication approximation if a nonzero contact angle is imposed as boundary condition, without requiring infinite velocities at the contact line. Further more, they noted that while a lubrication approximation model can be devised which permits one to satisfy a contact angle boundary condition, the model is only valid for a small region in the (Ca, ϕ) parameter space, where ϕ is the contact angle. They overcame these shortcomings by deriving and numerically solving Stokes flow equations for the region near the contact line. Figure 1-2 shows the flow profile simulated by Goodwin and Homsy under different parameter values.

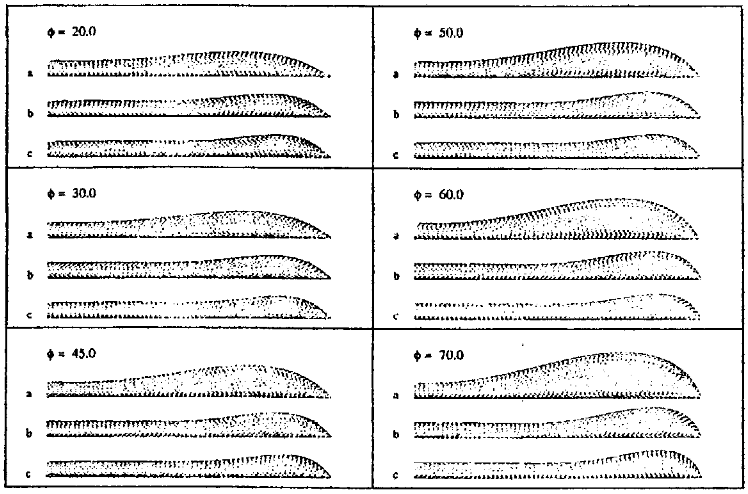

Figure 1-2: *Height profile over a range of Ca and* ϕ *with the inclination angle* α *held fixed at 45. Curves labeled a, b, and c represent Ca* $= 0.03, 0.10,$ *and* 0.15. *(Source: Goodwin and Homsy [23])*

A few observations can be made based on their simulation results. The magnitude of the principal hump increases as the capillary number decreases and as the contact angle increases. This is because the position of the free surface is a result of the interaction of the interfacial forces with the stress field interior to the fluid. The force exerted by the interface on the fluid is given by the product of the Gaussian mean curvature of the interface and the surface tension of the fluid interface. Therefore, for any fixed stress field interior to the fluid, the curvature of the interface must increase as the surface tension decreases. consequently, the interface of a fluid with high capillary number will have a high curvature. A high curvature means that the rate of change of the slope of the interface is high. Thus, the slope of the interface changes rapidly from the initial slope, as prescribed by the contact angle, to essentially zero slope, as dictated by the upstream asymptotic boundary condition. This will result in a small slope. Next, consider two free surfaces which start at two different slopes but have more or less similar curvatures. The interface which starts out with the highest slope has to effect the greatest change in slope in order to become horizontal. Because the slopes of the two lines are changing at about the same rate, the one with the larger initial slope will have the larger hump.

Jerret and de Bruyn [37] and de Bruyn [13] carried out more experimental studies to compare with the theoretical results obtained by Troian *et al.* as well as to further quantify the instability by measuring the manner in which the fingering patterns grow. A wider range of slope inclinations, including small angles were studied. The first paper by Jerret and de Bruyn characterized the flow of a strongly nonwetting fluid. Recall that for a strongly nonwetting fluid, long parallel-sided rivulets form, the troughs stop moving, and the regions of the surface between the rivulets remain dry. Huppert found both experimentally and theoretically that, prior to the onset of the instability, the position of the contact line moves downhill like $x \sim t^{1/3}$ (Equation 1.1). Jerret and de Bruyn found that at all but the smallest angles studied, their data is consistent with power-law behavior, but with exponents somewhat larger than 1/3. The exponents they determined for the flow before and after the instability are the same - about 1/2 for HMO ("heavy" mineral oil) and about 2/3 for glycerin. They also noted that the behavior observed at the smallest angles for both fluids is transient, and that the flow of the uniform contact line approaches $t^{1/3}$ at long times. Their studies on development of the fingers about instability show that the growth of the fingers is well described by a power law in time, and the troughs display an exponential slowing down to a final velocity close to zero. The wavelength of the pattern decreases with increasing inclination angle in reasonable agreement with the predicted $(\sin\alpha)^{-1/3}$ behavior, while the width of the fingers decreases more steeply with increasing α.

A separate study by de Bruyn studied the flow of a thin sheet of silicone oil down an inclined plane. Silicon oil wets the glass surface and a sawtooth like pattern forms. Despite the fact that the measurements were performed at low inclination angles while the theoretical predictions by Troian *et al.* are valid only at large angles, there is substantial qualitative agreement between the two. In particular, when the finger length is scaled by $l = H(3Ca)^{-1/3}$ and time by l/U_0, where U_0 is the average front speed, the data collapses on a universal curve.

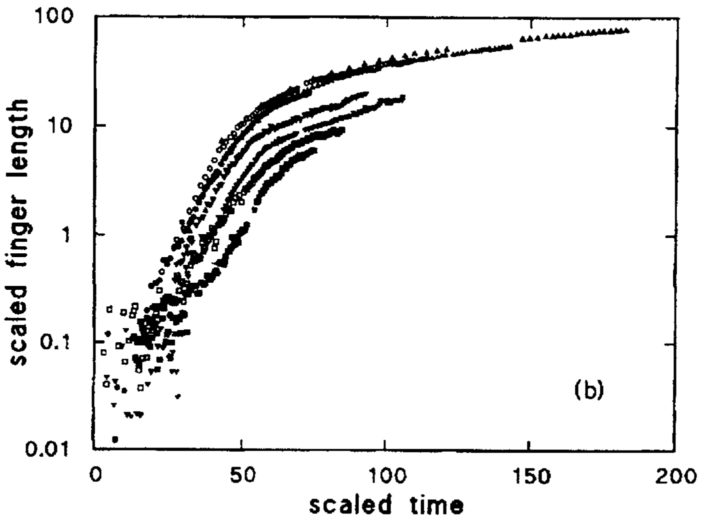

Figure 1-3: *A semilogarithmic plot of finger length (scaled by l) vs time (scaled by l/U_o) for eight inclination angles:* $2^o, 3^o, 4^o, 5^o, 6^o, 8^o, 12^o, 21^o$ *(Source: de Bruyn [13])*

The scaled flow rates are in all cases well described by exponentials out to scaled time $\tau \approx 40$. The mean averaged growth rate $\bar{\beta}$, over inclination angles α from 2^o to 21^o, is $\bar{\beta} = 0.110$. The growth rate predicted by the calculations of Troian *et al.* depends weekly on the precursor film assumed in their calculations, but is approximately 0.5, somewhat larger than found from de Bruyn's experiments. Furthermore, the wave number averaged over all angles is $q = 0.675 \pm 0.060$, which is approximately 50% higher than calculated most unstable wave number $q \sim 0.45$.

Experimental results by de Bruyn clearly showed discrepancies from the theoretical predictions. This triggered more theoretical studies on the instability mechanism. Spaid and Homsy [61] showed that the stability of the advancing capillary ridge is governed by rearrangement of fluid in the flow direction, whereby thicker regions of fluid advance more rapidly in the streamwise direction. Stabilizing capillary pressure gradients arising from variations in the spanwise curvature of the free surface determine the cutoff wave number above which all modes are stable. They used two methods for relieving the contact line singularity: matching the free surface profile to a precursor film, and introducing slip at the solid substrate. They obtained very similar results from two different methods. They also reported that the two models compare quantitatively when the precursor film thickness b is numerically equal to the slip parameter α.

Bertozzi and Brenner [8] [7] attempted to resolve the discrepancies seen in de Bruyn's experiments and extended the analysis to include low inclination angles. Their analysis addressed the case of completely wetting fluids and used a precursor film of thickness b as the boundary condition at the contact line. They noted that the base state before the instability [57] [30] is a traveling wave solution $h(x,y,t) = h_0(x - Ut)$ of Equation 1.4. The function $h_0(x)$ satisfies

$$-Uh_0 + (h_0^3 h_{0xxx} - D(\alpha) h_0^3 h_{0x}) + h_0^3 = d \tag{1.8}$$

where d is a constant of integration, and $D(\alpha) = \cot(\alpha)(3Ca)^{1/3}$. Matching the front onto the rest of the solution specifies the integration constant d and the velocity U of the traveling wave. as $x \to -\infty$, the front matches onto $h_0 \to 1$. As $x \to \infty$, the front must match onto the contact line. These two matching condition fix both U and d to be

$$U = \frac{1-b^3}{1-b}, \quad d = -b\frac{1-b^2}{1-b} \tag{1.9}$$

which uniquely fix the traveling wave solution.

When $D = 0$, corresponding to $\alpha = 90^o$, their results agree with those of Troian *et al.*. However, when D is increased, the size of the bump is substantially diminished, and at certain value of b, the bump essentially disappears. Therefore, the height of the bump is a strong function of D and b. For each value of b, there is a critical value of D for which the bump completely disappears.

They went on to prove that when the bump disappears, the front is linearly stable. Their linear stability analysis is briefly outlined here. Consider a perturbation, $\epsilon g(x,y,t)$, to the front h_0. g is taken as $O(1)$ and $\epsilon \ll 1$. Using a reference frame traveling with the speed of the traveling wave U, plugging $h = h_0 + \epsilon g(x,y,t)$ into

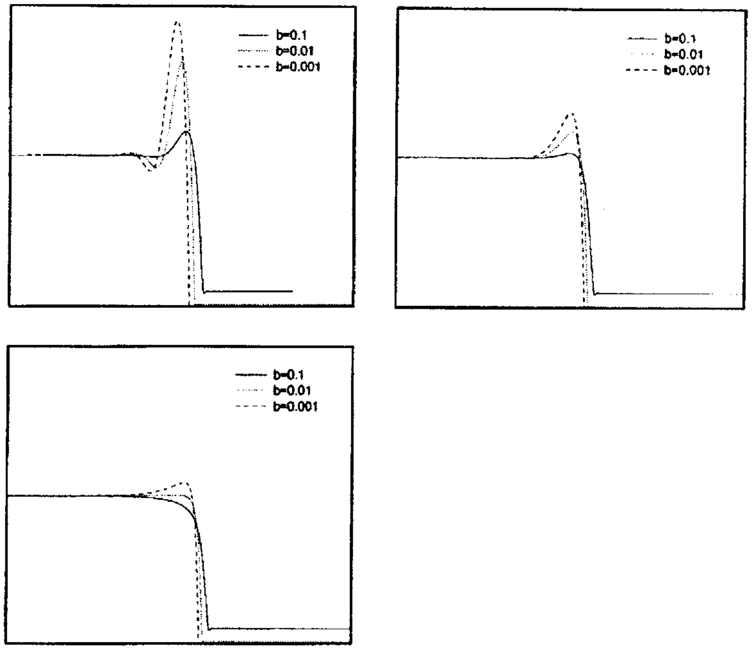

Figure 1-4: *Profiles for* $b = 0.1, 0.01$ and 0.001. *The maximum thickness of the bump is a logarithmic function of* b. *The first graph shows the case* $D = 0$, *the second* $D = 2.5$ *and the third* $D = 5$. *Note that in each successive graph, the heights of bumps are substantially diminished. (Source: Bertozzi and Brenner [7])*

Equation 1.4 and saving only those terms that are $O(\epsilon)$, the equation for the perturbation profile g is

$$g_t + \nabla \cdot (3h_0^2 g(\nabla\nabla^2 h_0 - D(\alpha)\nabla h_0)) + \nabla \cdot (h_0^3(\nabla\nabla^2 g - D(\alpha)\nabla g)) + 3(h_0^2 g)_x - U g_x = 0 \tag{1.10}$$

Since the steady solution, h_0, does not depend on the transverse variable y, Equation 1.10 can be Fourier transformed in y

$$\begin{aligned} g(x,q)_t &+ \partial_x(3h_0^2 g(\partial_x^3 h_0 - D(\alpha)\partial_x h_0)) + \partial_x(h_0^3(\partial_x^3 g - D(\alpha)\partial_x g)) - q^2 h_0^3 g_{xx} \\ &+ D(\alpha) q^2 h_0^3 g - q^2 \partial_x(h_0^3 \partial_x g) + q^4 h_0^3 g + 3(h_0^2 g)_x - U g_x = 0 \end{aligned} \tag{1.11}$$

where q is the wave number. If $g(x,q) = e^{\beta t}\varphi(x,q)$, the spacial dependence $\varphi(x) \approx h_{0x}$ for sufficiently long wavelength disturbances. To leading order in q^2, the growth rate is then

$$\beta(q) = \frac{q^2}{1-b}\int_{-\infty}^{\infty}(h_0 - 1)(h_0 - b)(h_0 + 1 + b)dx \tag{1.12}$$

The most important feature of Equation 1.12 is that if $h_0 < 1$, then $\beta(q) < 0$ at long wavelength. Thus, for the profile to be linearly unstable, the bump must have a finite size. For $D = 0$, maximum growth rate occurs at $q \sim 4.5$, which agrees with the computations of Troian *et al.*. However, Bertozzi and Brenner found that a moderate value of $D(\alpha)$ modifies the growth rate considerably. In this case, the inclined surface is at an angle to the vertical. The normal component of gravity to the inclined surface shifts the mode of maximum growth to longer wavelength. A more important observation is that the profile is linearly stable when b is larger than a critical value $b^*(\alpha)$ depending on the inclination angle. This confirms the previous predictions that the presence of the bump in the profile is responsible for linear instability. Figure 1-5 is a plot of growth rate with different simulation parameters.

$b^*(\alpha)$ decreases with decreasing α. Bertozzi and Brenner pointed out that a typical experimental surface has microscopic imperfections on the scale of μm, which translates to $b \sim 10^{-3} - 10^{-4}$. At this range of b, D in the range of $5 - 8$ can suppress the bump. The corresponding critical angle is around $\alpha^* \approx 5 - 10$ degrees. The existence of critical angle suggests a paradox: although the inclination angles explored in de

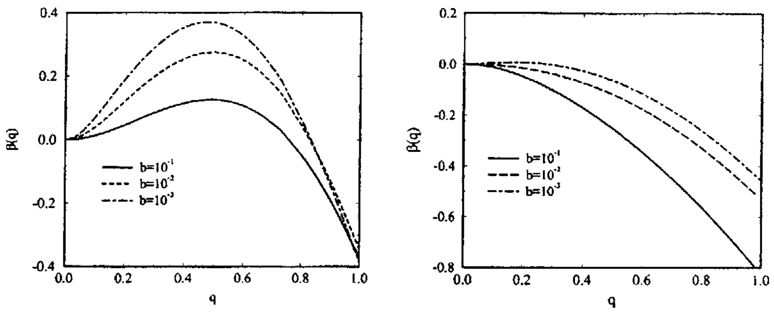

Figure 1-5: *The growth rate $\beta(q)$ computed from the long time behavior of solutions of the linear PDE (12) with $D(\alpha) = 0$ (left) and $D(\alpha) = 5$ (Source: Bertozzi and Brenner [7])*

Bruyn's experiments were in the range of 2-20 degrees, the experiments showed that the front destabilizes even at the smallest inclination angle. Bertozzi and Brenner presented a solution to this paradox by pointing out that even when the profile is linearly stable, there is always significant transient growth in which small perturbations near the contact line can grow by a factor of $10^3 - 10^4$. They explained that the transient growth is a result of the singular dependence of the outer flow on the microscopic scale at the contact line. For instance, as the fluid flows across a rough surface, fluctuations in the microscopic scale translate into large fluctuations in the outer flow. This transient growth triggers nonlinearities that result in a fingering instability.

In the analysis described so far, the flow has been assumed to be low Reynolds number flow and the inertial terms have been dropped. López, Miksis, and Bankoff [52] analyzed the effect of neglected inertial terms using Kármán-Pohlhausen method. From the steady state equation they derived, it is clear that the inertial terms only affect the dynamics of the main body of the fluid film, but are not relevant in the neighborhood of the contact line. They also observed that if the Reynolds number is retained in the momentum equations, the steady-state profile gradually loses its oscillatory structure in the direction parallel to the flow as the Reynolds number increases. It is also clear that the inertial terms have rather weak influence on the instability, even for O(1) Reynolds numbers. More recent experimental works by Veretennikov, Indeikina, and Chang [34], Hocking, Debler, and Cook [41], and Johnson, Schluter, Miksis, and Bankoff [44] revealed more interesting features of the flow and showed that the problem is more complicated than previously thought.

Veretennikov *et al.* [34] reported that a partially wetting fluid characterized by a larger contact angle can form an overhanging "nose" at the contact line, in contrast to the "wedge" profile typical of more wetting fluids. They found that a nose always appears when the front is sufficiently thick and the driving force is sufficiently large. If the liquid is pushed forward with higher speed than the largest possible speed of molecular wetting by some external forces, the front protrudes beyond the contact line and forms a nose. Gravity is one such external force. In this case where an overhanging nose is formed, liquid wettability becomes inconsequential, and there is then no need for a contact angle condition in the numerical simulations as suggested by Goodwin and Homsy [23]. Veretennikov *et al.* were able to describe the motion of a nose front from their dye tracking experiments. They reported that there is a recirculating vortex with a multi-valued nose, and the contact line itself does not move at all. Instead, a new contact line is created at every instant in time and liquid simply falls down onto the plane.

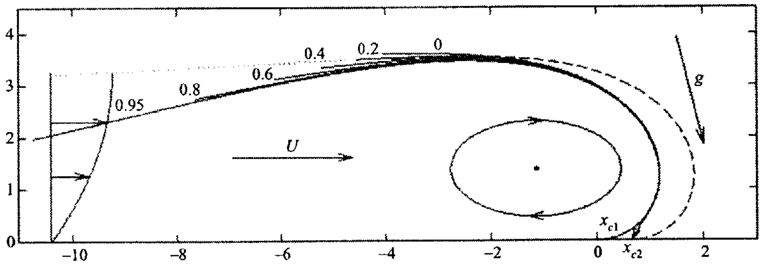

Figure 1-6: *Schematic representation of the vortex motion of the liquid within the multi-valued nose (Source: Veretennikov, Indekina and Chang [34])*

Their observations on nose fronts also suggest that nose fronts are very common for thick films advancing on a dry plane. The nose fronts are not sensitive to surface noise and do not possess a bump at small inclination angles. Therefore, such fronts do not finger by the proposed instability or transient growth mechanism for wedge fronts discussed before. Veretennikov *et al.* proposed a physical mechanism for fingering from a nose front. They suggested that the nose front is only possible if the liquid thickness near the front is sufficiently high. Due to the conservation of the total liquid volume, the nose height decreases as the front spreads forward. As a result, the apparent contact angle also decreases until it reaches $\theta_c = \pi/2$. The front is very unstable when the contact angle is close to $\pi/2$ because any infinitesimal local disturbances of the front shape along the contact line will change the local mechanism of spreading from vortex motion with low resistance to a unidirectional flow with high resistance. The front segments with $\theta > \pi/2$ will continue to advance with the original front speed and hence will accelerate relative to segments with $\theta < \pi/2$ which begin to decelerate. Hence, the front suffers high frequency transverse modulations due to the above amplification of small-amplitude noise.

Veretennikov *et al.* performed experiments on both dry and prewetted surfaces and obtained different patterns as shown in Figure 1-7. A nose front is likely to be formed on a dry surface. In this case, even though Castor oil is a highly wetting fluid, its fingering behavior is qualitatively similar to that of glycerin with smooth minima. However, when the surface is pre-wetted, a wedge front forms. A thick pre-wetted film can prevent fingering altogether while sawtooth patterns as expected from wetting fluid form in the case of thin pre-wetted film. Therefore, fingering from wedge fronts is triggered by a mechanism different from nose fronts and the final pattern formed is sensitive to the thickness of the pre-wetted film.

Hocking *et al.* [41] observed both triangular and finger shaped patterns with a single fluid-solid configuration. They used silicon oils of a range of kinematic viscosities (10cSt-100cSt), volumes (40 to 120 cm^3), and plate angles ($10^o - 45^o$). In nearly all the cases, they observed sawtooth-shape disturbances, with only a single example of the parallel-sided pattern. They reported that the parallel-sided pattern only occurs for the highest slope and lowest volume, but for a viscosity in the center of the range examined. The result is rather peculiar because the range of capillary numbers in this case is similar to that found in all the other cases in which sawtooth pattern is

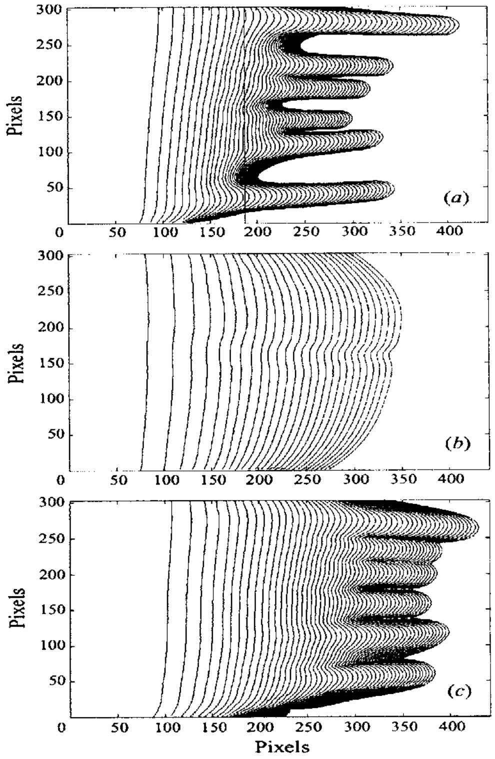

Figure 1-7: *(a) Highly wetting Castor oil on a dry plane. (b,c) The plane is first covered with a prewetting film of Castor oil. (b) The film is drained for 2h. (c) Drainage takes place for 12h. (Source: Veretennikov, Indekina and Chang [34])*

formed. Moreover, neither the static nor the dynamic contact angle for the fingers is outside the ranges covered by those for the sawtooth patterns. This is contradictory to the hypothesis by Silvi and Dussan [60] that sawtooth shapes are associated with small contact angles and parallel-sided rivulets with larger contact angles. They also mention that the exponent for the roots sometimes has a value larger than that for the corresponding tips.

Johnson *et al.* modified the experimental setup to allow for a continuous flow of fluid, known as a "constant flux" configuration. Previous experimental, theoretical and computational studies on the problem had focused on the "constant volume" configuration. With this configuration, the value for the theoretical fluid depth d_0 is defined as

$$d_0 = (3Q\nu/g\sin\beta)^{1/3} \tag{1.13}$$

where Q is the volumetric flow rate per unit width, ν is kinematic viscosity and β is angle of inclination. The measured values from their experiments are consistently larger than the calculated value by an average of 5%. They explained that this difference is attributed to small surface waves which disspate energy, resulting in a slightly thicker film than calculated from Equation 1.13.

In their study, the fluid depth profiles show that the back side of the hump has a smaller slope as β decreases. The flow profile is shown in Figure 1-8. This leads to a related question of whether a critical angle exists below which the hump disappears for a two-dimensional front. To answer the question, Johnson *et al.* conducted experiments on a slope of $\beta = 1.8^o$, which is well below the calculated critical angle of 5^o by Bertozzi and Brenner. At this low angle of inclination, they still observed a pronounced hump and the leading edge became unstable. This result suggests that the linear instability mechanism associated with the presence of a hump is still dominant at this low inclination for their experimental configuration.

Johnson *et al.* derived a relationship between the dynamic contact angle θ and speed of the finger tips U. The relationship is approximately linear. They also systematically varied the Renynolds number in their experiments, the results obtained showed relatively little effect of fluid inertial on the pattern formation process. Wave-

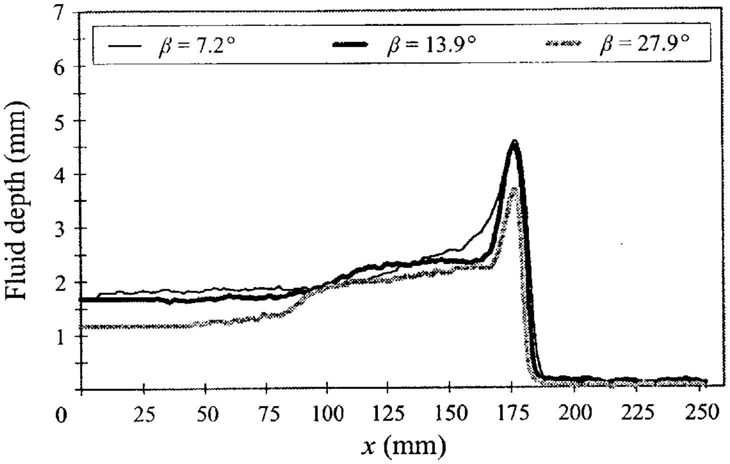

Figure 1-8: *Plot of fluid depth as a function of distance in the direction of flow for* $Re = 0.13$, $\beta = 7.2^o$, 13.9^o *and* 27.9^o *with corresponding* $Ca = 0.010$, 0.012 *and* 0.015 *(Source: Johnson, Schluter and Bankoff [44])*

length λ was found to increase with a decrease in β. The most unstable wavelength λ_{max} was found for experiments with different parameters, and fitted into a function of $d_0/(3Ca)^{1/3}$. This length $d_0/(3Ca)^{1/3}$ was chosen because the scaling argument by Huppert implies that

$$\lambda_{max} = Kd_0/(3Ca)^{1/3} \tag{1.14}$$

where K is a constant. A least-square fit of the data gives $K = 13.9$. The same constant k was found experimentally to be approximately 18 by Huppert and numerically to be 14 by Troian *et al.* If the power of the capillary term is not fixed, a better fit to experimental data is given by

$$\lambda_{max} = 9.2d_0/(3Ca)^{0.45} \tag{1.15}$$

which suggests a dependence of λ_{max} on $Ca^{-1/2}$ instead of $Ca^{-1/3}$.

In general, the patterns formed exhibit a dependence on the angle of inclination of the plate and the capillary number of the flow. Johnson *et al.* also raised a question regarding the appropriateness of comparing their experimental results from those using constant volume, because significantly different fingering behavior takes

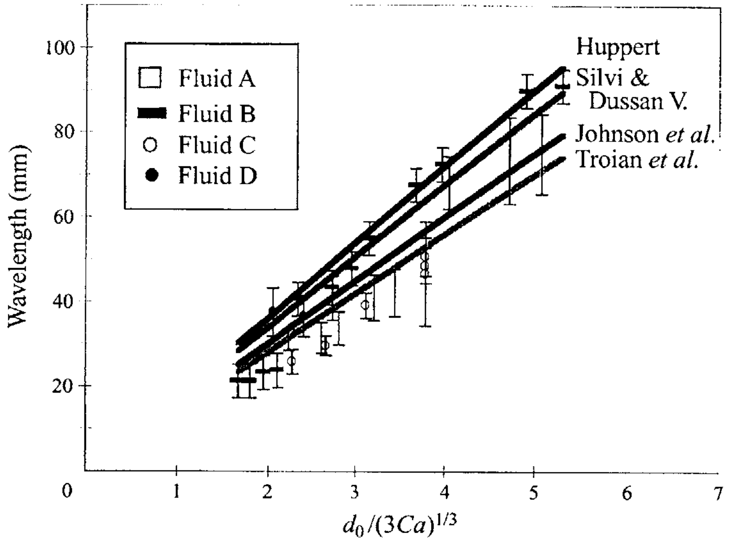

Figure 1-9: *Comparison of experimental wavelength data with the predictions of several models (Source: Johnson, Schluter and Bankoff [44])*

place in these two distinct configurations.

Despite years of study on the problem, there are still areas that are yet to be understood. Recently, more computational work has been done, which mainly focus on nonlinear instabilities of the contact line as well as the long time evolution of the instabilities.

Kalliadasis [38] relaxed some restrictions imposed on the linear stability analysis by incorporating a weakly nonlinear analysis on the instability. A linear stability analysis can only deal with the linear stage of the instability and hence is only strictly valid for infinitesimal disturbances of a truly nonlinear system. Using methods from dynamical systems, he derived a partial differential equation for the evolution of the fingers in the weakly nonlinear stage of the instability. The equation is accurate to third order in the amplitude of the disturbances. The instability is proved to be a phase instability associated with the translational invariance of the system in the direction of flow. Through numerical simulation with a constant thickness precursor film, he was able to show that the fingering instability develops into a saw-tooth pattern qualitatively similar to that observed for completely wetting fluids on a dry surface. The parallel-sided fingers for partially wetting fluids on dry surfaces were never observed in his numerics. Thus, he postulated that the precursor film model cannot be used to model spreading of partially wetting fluids on dry surfaces. The numerics show that large values of the precursor film thickness correspond to a small number of fingers. This is consistent with the experimental results reported by Veretennikov.

Eres, Schwartz and Roy [45] performed simulations and successfully reached a nontrivial traveling wave for the flow of a completely wetting fluid down a vertical plane. A nontrivial traveling wave is a steady flow configuration characterized by a nonuniform structure in the spanwise direction. They generalized the behavior and stated that for motions on a prewetted substrate of sufficient surface energy and negligible contact angle effects, finger profile will eventually achieve a steady-state configuration.

L. Kondic and J. Diez [39] studied the flow of a completely wetting fluid, and analyzed the influence of the inclination angle on the two most relevant aspects of the instability: shape of the patterns and surface coverage. In their simulations, the fluid thickness was kept constant far behind the apparent contact line, which resembles the experimental configuration used by Johnson *et al.*. They made two important conclusions in their work. First, the inclination angle can significantly influence the stability of the contact line in the case of spreading of a completely wetting fluid on an inclined plane. Large inclination angles (measured from the horizontal) lead to fingers with almost straight sides, while smaller inclination angles lead to patterns with much more oblique sides, resembling experimentally observed saw-tooth patterns. This was not previously reported by Kalliadasis because his study had been mainly focusing on small inclination angles. Second, the question of surface coverage is not necessarily related to the shape of the emerging patterns. In all of their simulations, the roots of the patterns move, leading to a complete surface coverage. However, the shape of the patterns can vary considerably. This result is consistent with many past experiments that partially wetting fluids are required for partial surface coverage.

Their computations also revealed several interesting features. A nontrivial traveling wave solution may exist for the flow down an inclined plane, with the steady-state

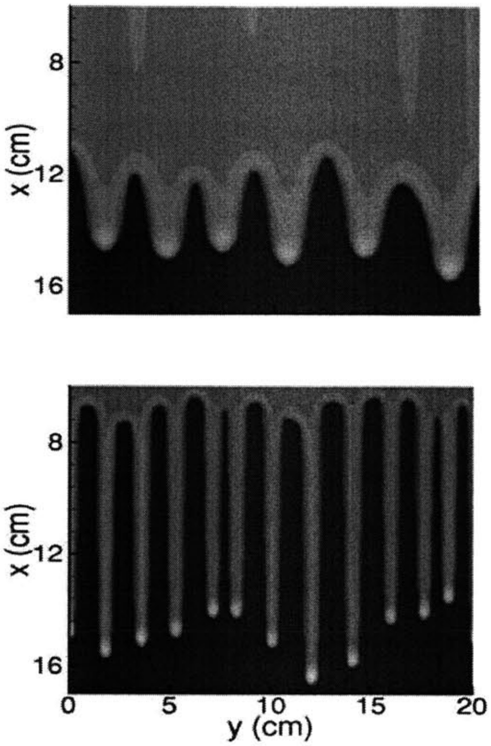

Figure 1-10: *Contour plots of fluid profiles for (top) large inclination angle, (bottom) small inclination angle, plotted when the fluid traveled the same distance downslope. (Source: Kondic and Diez [39])*

lengths of the pattern depending on the precise values of the flow and fluid parameters. Ignoring contact line instability and removing the transverse-direction dependence of the fluid profile, Figure 1-11 shows snapshots of the fluid profiles at equal time intervals. After initial transients, the flow develops a traveling wave profile, that moves with the constant velocity $v_f = 1 + b + b^2$.

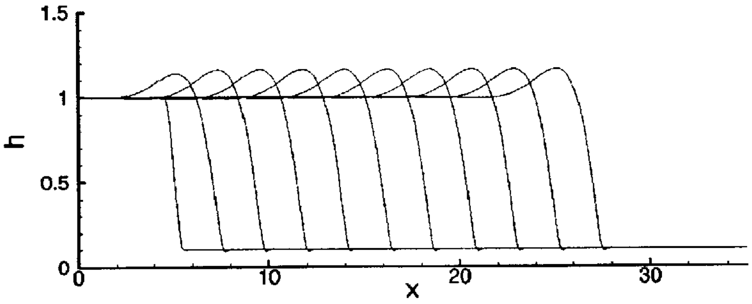

Figure 1-11: *Profile of a film flowing down an inclined plane (Source: Kondic and Diez [39])*

The fluid also forms a depression ahead of the front region, which leads to a local negative velocity field. Kondic and Diez explained that the fluid within the precursor film (which is flowing down with the velocity equal to b^2) is sucked into the bulk region due to a decrease in capillary pressure, and later pushed in the positive direction again.

1.2 Granular and Suspension Flow

Many industrial processes involve particulates, whether in the form of suspensions or dry granular flows. Granular and suspension flows are often very complex, and they present an engineering challenge that has so far been met empirically and with only partial success. In the last 2 decades, there has been interest in studying the behaviors of granular and granular-fluid flow. Among the interesting facets of granular flow behavior is a large set of instabilities, including oscillons formed in vertically vibrated containers (Umbanhowar, Melo & Swinney [51]), fingering instabilities in suspensions and dry granular flows (Lange *el al.* [3]; Pouliquen, Delour & Savage [50]), segregation of neutrally buoyant particles in suspensions (Tirumkudulu, Mileo & Acrivos [47]), wave patterns in sand (Fried, Shen & Thoroddsen [18]), and longitudinal vortices in granular flows (Forterre & Pouliquen [20]). Some of these instabilities associated with gravitational flow down an inclined plane are presented below.

1.2.1 Granular Flow

The flow of granular materials on inclined planes is of interest within the context of both industrial processing of powders and geophysical instabilities such as landslides and avalanches. Besides these important industrial and geophysical applications, granular chute flows down inclines are also of fundamental interest: A layer of granular material flowing on a surface is a simple and well controlled system which allows a precise study of the rheological properties of particulate systems.

The characteristics of granular flow are mainly controlled by the balance between the gravity force and the friction force exerted at the surface. Many chute flow experiments have been carried out and different configurations have been investigated: changing the bed condition from smooth to rough, using materials of different density and size, and varying the entrance conditions. When the inclined plane is smooth, it is found that fully developed uniform flows only exist at a critical inclination angle. Below this angle, the material stops. Above this angle, the material continuously accelerates along the plane. Such a system is well described by a constant friction coefficient [25]. When the bed is rough, similar accelerating flows are observed at high inclination angles. In this high velocity regime, direct or indirect measurements of the shear force of the bed [32] have shown that the material rheology is well described by a constant coulomb friction coefficient independent of the velocity. For intermediate values of the inclination angle in the rough bed configuration, steady uniform flows can be observed over a wide range of inclinations. In this range, the friction force is able to balance the gravity force, indicating a shear rate dependence. This intermediate regime exhibits many interesting features, and it has been extensively studied in experiments by Pouliquen *et al.* [50] and Pouliquen [55], and in theory by Pouliquen [54].

Pouliquen *et al.* first described an instability that occurs when a front of granular material propagates down a rough inclined plane. The front, which is initially uniform in cross-section, rapidly breaks up into fingers. Although this is similar in appearance to the instability seen in viscous fluids flowing down an inclined surface, in the case of viscous fluids, the instability is driven by surface tension as described in the previous section,whereas granular materials have no surface tension.

They performed their experiments using granular materials of different quality and the results indicate that the polidispersity of the granular medium plays an important role in the instability. In fact, a necessary condition for the occurrence of fingering in their experiments is the presence of coarse irregular particles in the material. Past studies have showed that in inclined chute flows of polydispersed media, the coarse particles come to the free surface, and it can be explained by a statistical sieving mechanism [58, 62]. In the case of propagating fronts, the vertical segregation occurring far from the front gives rise to a complex recirculation zone at the front [62]. Pouliquen *et al.* noted that this recirculation is exactly the origin of the fingering instability. At the outlet of the reservoir, the large particles rapidly segregate and arrive at the front flowing on the free surface where velocity is higher. These large particles reach the front and stop on the bed, while the front continues to propagate down the slope. The large particles are thus reinjected in the material. The particles then rise up again to the free surface as the segregation process takes place, giving rise to a recirculation motion in a frame moving with the front.

Pouliquen *et al.* also proposed an instability mechanism initiated from the recirculation. Suppose a small perturbation occurs at the front, the trajectories of the large particles arriving at the front are deflected toward the dip of the deformation, following the steepest slope of the free surface. However, the return trajectories of the coarse particles when they have just left the front remain approximately straight lines. A uniform concentration of large particles arriving at the free surface thus leads to a non-uniform distribution at the bed with high concentration at the dip of the

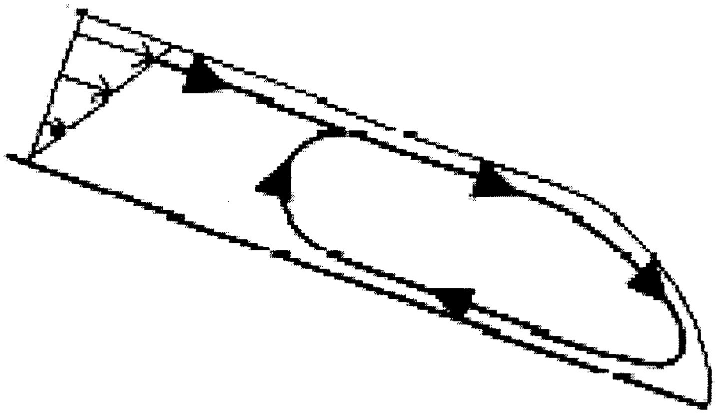

Figure 1-12: *Sketch of the recirculation of the large particles at the front (Source: Pouliquen, Delour and Savage [50])*

deformed front. This local increase of the concentration of large particles, together with the fact that they are irregular particles having a larger coefficient of friction, leads to a local increase of the friction. The material thus locally slows down which amplifies the deformation and ultimately leads to the formation of fingers.

In a separate paper, Pouliquen [55] proposed a new scaling law for granular flows down rough inclined planes. The major difficulty in describing inclined granular chute flows is that they belong to an intermediate flow regime, where both the friction between the grains and the collisions play an important role. Pouliquen adopted a more empirical approach in his study. He systematically measured the mean velocity of the flow u as a function of the inclination of the surface θ and of the thickness of the layer h. All the data obtained for different systems of beads corresponding to different surface roughness conditions collapse into a straight line when expressed in terms of the Froude number as function of $h/h_{stop}(\theta)$:

$$\frac{u}{\sqrt{gh}} = \beta \frac{h}{h_{stop}(\theta)} \tag{1.16}$$

The constant of proportionality β is found to be 0.136. The function $h_{stop}(\theta)$, which contains all the information about the influence of the inclination, the bead size, and the roughness of the bed, is simply obtained by measuring the thickness of the layer

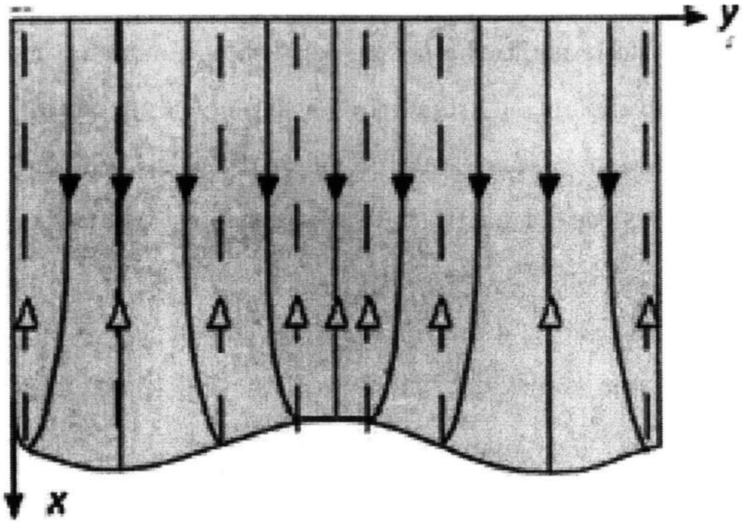

Figure 1-13: *Instability mechanism: the black (white) arrows represent the trajectories of the coarse particles on the top (bottom) of the avalanching material (Source: Pouliquen, Delour and Savage [50])*

remaining on the surface when a flow created at inclination θ stops.

Based on this scaling property, an empirical friction law can be proposed for the variation of the friction coefficient μ as a function of the mean velocity u and the thickness h:

$$\mu(u,h) = \tan\theta_1 + (\tan\theta_2 - \tan\theta_1)\exp(-\frac{\beta h}{Ld}\frac{\sqrt{gh}}{u}) \tag{1.17}$$

where d is the particle diameter, θ_1 corresponds to the angle where $h_{stop}(\theta)$ diverges, θ_2 to the angle where $h_{stop}(\theta)$ vanishes, and L is the characteristic dimensionless thickness over which $\theta_{stop}(h)$ varies. By introducing Equation 1.17, Pouliquen was able to quantitatively predict how the thickness of the avalanching layer goes to zero at the front for the whole range of inclination, thickness of the layer and roughness. Moreover, the measurements from experiments [54] agree well with the theoretical predictions without any fitting processes.

Forterre and Pouliquen observed a new instability different from the one described above in rapid granular flows down rough inclined planes [20]. In the regime of high inclinations and flow rates, the granular material flowing out from the reservoir accelerated along the slope while the thickness of the granular layer decreased. At a certain distance from the outlet (from 0.4 to 1.3m depending on the flow conditions), a regular pattern developed and longitudinal streaks parallel to the flow direction were observed. The streaked pattern was not stationary, but slowly drifted in the transverse y direction with a phase velocity small compared to the chute x velocity. They investigated the grain motions once the pattern was fully developed by measuring the longitudinal and transverse velocities $V_x(y)$ and $V_y(y)$. They found that the instability induces spatial velocity modulations which are correlated with the surface deformation. First, the longitudinal particle velocity V_x is no longer uniform across the bed, but becomes greater in the troughs than in the crests. The second result is that the instability also induces periodic modulations of the transverse velocity: particles no longer follow the bed slope, but also experiences lateral motions. These modulations imply a three-dimensional particle motion and the presence of longitudinal vortices in the bulk. Particles move upwards at the crests and downwards at the troughs. The longitudinal vortices are then counter rotating with one wavelength λ of the wavy surface corresponding to a pair of vortices as sketched.

From the experimental observations, Forterre and Pouliquen proposed a mechanism for the longitudinal vortex formation based on the concept of granular temperature. When the instability appears, the flow is rapid and dilute, and its dynamics are controlled by the particle-particle and particle-boundary collisions. In this regime, the granular material can be seen as a dissipative dense gas, and a granular temperature can be defined related to the fluctuating motion of the grains. In their experiments, the source of the fluctuating motion is the roughness of the bed. Hence, as the flow accelerates from the outlet of the reservoir, particles close to the plane become more and more agitated due to collisions with the rough bed. The bottom granular temperature then increases along the slope. Consequently, the density at the bottom decreases and eventually becomes smaller close to the plane than above. The flow is then mechanically unstable under gravity because the heavy material is above the light one yielding convective longitudinal rolls.

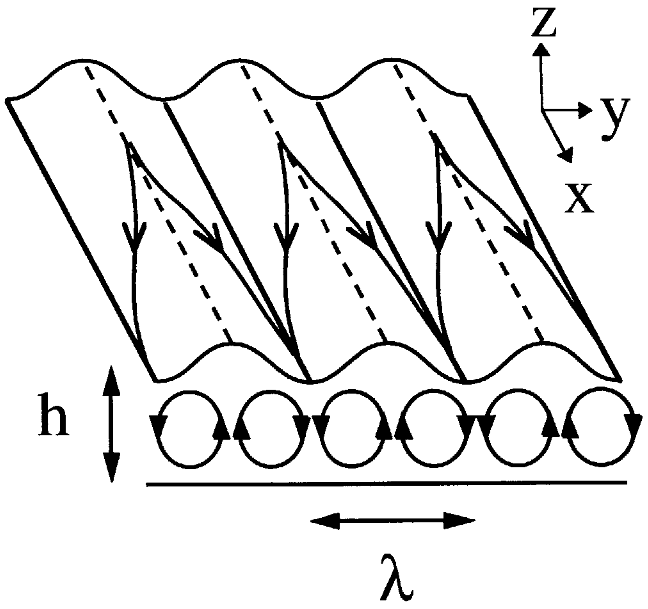

Figure 1-14: *Sketch of the particle trajectories showing the longitudinal vortices (Source: Forterre and Pouliquen [20])*

In order to investigate the relevance of the proposed mechanism, they performed a three dimensional linear stability analysis [20] of steady uniform flows down inclined planes using the kinetic theory of granular flows. They showed that in a wide range of parameters, steady uniform flows are unstable under transverse perturbations. The structure of the unstable modes is in qualitative agreement with the experimental observations. The agreement is only qualitative, because the experimental conditions of thin flow, semi-dilute regime with rather inelastic particles are beyond the domain of applicability of the simple kinetic theory. Nevertheless, their study showed that the kinetic theory is a relevant framework for the description of rapid granular flows. The kinetic theory is able to reveal the new instability mechanism specific to granular material: inelastic collisions trigger a self-induced convection yielding longitudinal vortices in chute flows. Since Rayleigh-Bénard convection is the paradigm for pattern forming instabilities in fluid mechanics, they raised a relevant question of whether the granular convection represents the starting point of a similar scenario towards more complex structures. Indeed, they reported that a new pattern was observed when the plane was strongly inclined ($\theta > 50^o$). Instead of longitudinal streaks, a regular square pattern looking like fish scales developed on the free surface.

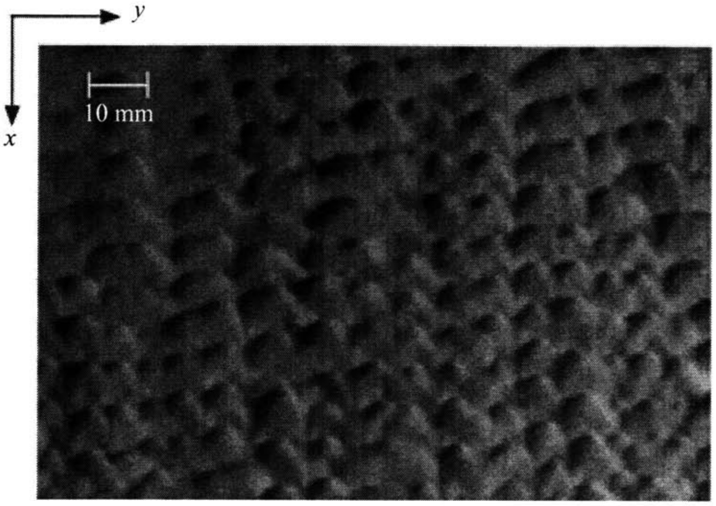

Figure 1-15: *Top view of the free surface of the flow showing the formation of 'scales' when the plane is strongly inclined (Source: Forterre and Pouliquen [20])*

1.2.2 Suspension Flow

A flow regime between the granular flow and the viscous fluid flow is the flow with particles embedded in an interstitial fluid. Such flow is dominated either by the effects of particle inertia or by effects of fluid viscosity. The Bagnold number B [4] expresses the ratio of collision forces between the grains to viscous forces in the fluid-grain mixture. A small Bagnold number, $B < 40$, characterizes the regime of the macro viscous flow. In this regime, the viscous interaction with the pure fluid is important. Examples for this type of flow are mud slides and the transport of water-sand mixtures in river beds. At large Bagnold numbers, $B > 450$, the flow is called grain-inertial regime where the grain-grain interactions dominate. Since our study involves small particles embedded in a very viscous fluid, where $B \approx O(1)$, it falls into the regime where viscous force dominates.

Most of the instabilities observed in suspension flows can be attributed to an instability known as the Rayleigh-Taylor instability. In flows with heavy particles, rapid shearing motion adjacent to a boundary can create a region of low density that supports the weight of a denser, slower shearing layer. This adverse density stratification can then be unstable to spanwise disturbances. A local increase in density or particle fraction will fall due to gravity and drag down material from above which is even denser, further enhancing the perturbation. In the case of a particle laden flow down an inclined plane under gravity, the particle volume fraction, and therefore the density, can increase with height in the velocity gradient direction due to a balance between shear-induced particle migration and buoyancy and thus be unstable.

Lange *et al.* [3] used a closed Hele-Shaw cell to study the fingering instability in a water-sand mixture. They found that the measured velocity for the largest finger is typically three times the Stokes velocity of a settling hard sphere. Furthermore, the velocity is nearly independent of the mass of the sand and diameter of the particles. This independence of particle properties encourages a fluid-like description of the water-sand mixture. They postulated that it is possible to model the water-sand mixture as a Newtonian fluid with effective properties depending on the concentration of the particles. However, such a simple model has its limitations. To use the model, one must assume that the particle concentration in the flowing mixture does not vary too much. Furthermore, the particles have to be large enough to neglect their Brownian diffusion.

In a separate study, Völtz *et al.* [9] performed numerical simulations on a glycerin-sand mixture in Hele-Shaw cell using the one-fluid model with effective properties and compared the numerical results with the experimental observations. They concluded that the one-fluid continuum model describes satisfactorily the experimental results. Their results showed convincingly that a simple hydrodynamic approach to diluted suspensions is reasonable and more refined theoretical models like two-fluid models seem to yield no additional insight. However, it should be noted that their experiments involved only low concentration suspension.

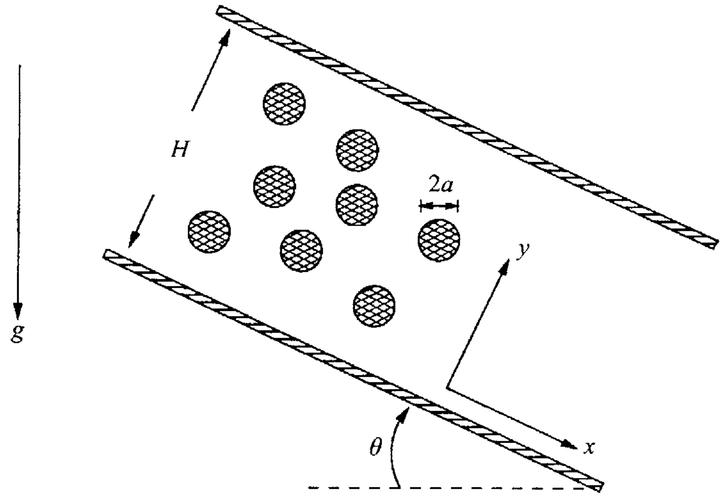

Figure 1-16: *Gravity-driven flow of a suspension through an inclined channel of height H in Carpen and Brady's experiment (Source: Carpen and Brady [11])*

Carpen and Brady [11] performed a comprehensive study on gravity-driven flow of a suspension down an inclined channel as shown in Figure 1-16. They modeled the system as a continuum viscous suspension and used the suspension-balance model of Nott and Brady [49] as modified by Morris and Brady [46]. Inertia effects were ignored and the suspension as a whole was taken as incompressible. Numerical simulation revealed that the velocity profile of the base state is blunted in comparison to the corresponding parabolic Newtonian velocity profile associated with channel flow. Moreover, decreasing inclination angle and increasing density ratio led to increasing sedimentation. Most importantly, simulation of the model showed that the system has an adverse density profile of heavier material over light, a driving force for instability.

They also performed a standard linear stability analysis on the base state and reported the existence of a maximum growth rate for spanwise instabilities on the order of the height of the channel, H. The instability is present whenever the flow-generated density gradient is aligned normal to gravity. The growth rate for the spanwise instability depends on particle-fluid ratios and channel inclination angles as

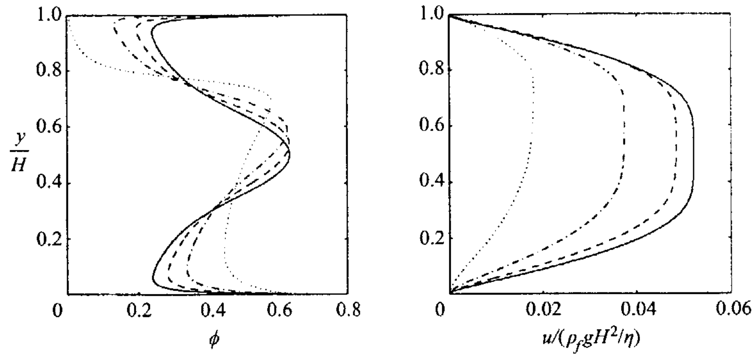

Figure 1-17: *Base state volume fraction* ϕ_b *and velocity profiles for* $\phi_b = 0.40$, *channel heigth to particle size ratio* $H/a = 30.54$. *Inclination angle* $\theta = 30^o, 50^o, 70^o, 90^o$. *Increasing* θ *results in increasing symmetry around the centre of the channel. (Source: Carpen and Brady [11])*

well as on the bulk particle volume fraction and to a much lesser extent on the ratio of particle size to channel height.

Chapter 2

Influence of Particles on Mixture Properties

2.1 Viscosity

Einstein's inaugural dissertation at Zurich [19] included the theory of the viscosity of a dilute dispersion of rigid spheres. With μ the viscosity of the suspension, μ_0 that of the medium, and c the volume fraction of spheres in the suspension, Einstein's result for the relative viscosity $\mu_r = \mu/\mu_0$ can be written as

$$\mu_r = 1 + 5c/2 + O(c^2) \tag{2.1}$$

The intrinsic viscosity $[\mu]$ defined as

$$[\mu] = \lim_{c \to 0} (\mu_r - 1)/c \tag{2.2}$$

is exactly 5/2, regardless of the size or size distribution of the spheres. Equation 2.1 only works for a dilute mixture. At finite concentration, the relative viscosity $\mu_r = h(c)$ is determined by the requirement that the slope of the function at the origin equal the intrinsic viscosity, while the behavior at high concentration is governed by the fact that beyond a volume fraction c_m, called the packing fraction, the dispersed particles lock into a rigid structure, and flow ceases.

The nature of the function $h(c)$ has been the subject of many studies, both experimental and theoretical. The generally accepted form derived from a semi-continuum approach is

$$\mu_r = [1 - (c/c_m)]^{-[\mu]c_m} \tag{2.3}$$

The viscosity of a suspension is comprehensively studied by Krieger [40], and he arrives at a rheological equation of state for rigid-sphere dispersions in steady flow in the form

$$\mu_r = \mu_{1r} + (\mu_{2r} - \mu_{1r})/(1 + 0.431\,|\tau_r|) \tag{2.4}$$

The viscosity of a suspension depends on shear stress τ_r and its value decreases from a zero-shear value μ_{2r} to a high-shear limit μ_{1r}. According to Krieger,

$$\mu_{1r} = (1 - c/0.68)^{-1.82} \tag{2.5}$$

$$\mu_{2r} = (1 - c/0.57)^{-1.50} \tag{2.6}$$

These expressions permit the prediction of the steady-state viscosity of a uniform hard-sphere suspensions of any diameter in a medium of any viscosity, at any volume fraction or shear stress.

2.2 Hindered Sedimentation

There have been numerous experimental and theoretical investigations of the sedimentation of particles in a fluid. One of the earliest of these is Stokes' analysis of the translation of a single rigid sphere through an unbounded quiescent Newtonian fluid at zero Reynolds number, which leads to his well-known law

$$V_{stokes} = \frac{2a^2(\rho_s - \rho)g}{9\mu} \tag{2.7}$$

where V_{stokes} is the settling velocity of the sphere, a is its radius, ρ_s is its density, ρ is the fluid density, μ is the fluid viscosity, and g is the gravitational constant. Since then, research has focused on extending Stokes' law by considering nonspherical rigid particles, drops and bubbles, non-Newtonian fluids, nonzero Reynolds numbers, the presence of a wall near the particle, and interactions between particles. In this paper, we do not attempt to present a complete review of the general subject of sedimentation, but rather we discuss a few important developments. In this section, we will focus on the theoretical and experimental determination of the average settling velocity of identical spherical particles in a suspension that is not infinitely dilute.

If the suspension is infinitely dilute, the particles settle with their Stokes velocity given by Equation 2.7. On the other hand, for particle volume fractions as small as 1%, the average settling velocity of the spheres is noticeably lower than that given by Stokes' law. This phenomenon can be represented by a hindered settling function $f(c)$ such that the average fall velocity of a sphere in the suspension is given by $V_s = V_{stokes} f(c)$. It is generally assumed that $f(c)$ depends only on the solids volume fraction c and that it is a monotonically decreasing function with $f(0) = 1$.

Different hindered settling functions have been proposed based on many sedimentation and fluidization experiments. In the limit of low volume fraction c, theories predict the sedimentation velocity as [6]

$$V_s = V_{stokes}[1 - 6.55c + O(c^2)] \tag{2.8}$$

The main assumptions in theories leading to the above prediction are: neglect inertia since the particle Reynolds number is small; consider only two body interactions between the spheres since the volume fraction is low; and the system size is infinite in the direction transverse to the settling. Experimental fits of the average settling velocity as a function of volume fraction have shown a roughly linear dependence on c in the limit of small volume fraction c, although with a prefactor that is systematically smaller than 6.55 [12].

A different settling function was proposed by Ham and Homsy [28] for suspensions with volume concentrations of 2.5%-10%.

$$V_s = V_{stokes}(1 - 4c + 8c^2) \tag{2.9}$$

Settling velocity may vary linearly with volume fraction when the mixture is very dilute. However, when volume fraction is increased, a more complicated function is needed to account for more complex interactions between the particles. Barnea and

Mizrachi [5] proposed a semi-empirical formula which provides the best fit to their experimental data for very small particle Reynolds numbers.

$$f(c) = \frac{(1-c)^2}{(1+c^{1/3})\exp(5c/3(1-c))} \tag{2.10}$$

On the other hand, the most commonly used empirical correlation is that attributed to Richardson and Zaki [56].

$$f(c) = (1-c)^n \tag{2.11}$$

where, according to Garside and Al-Dibouni [22], a value of $n = 5.1$ most accurately represents their data for small Reynolds number. It is evident that the two functions 2.10 and 2.11 behave quite differently, especially for small c. In the dilute limit, Equation 2.10 has the form $f(c) \sim 1 - c^{1/3}$, whereas Equation 2.11, with $n = 5.1$ becomes $f(c) \sim 1 - 5.1c$. Figure 2-1 plots the hindered settling velocity functions discussed above in the range $c = 0$ to $c = 0.5$. From the plots, it is clear that the function proposed by Zaki (Equation 2.11) has values close to the one proposed by Ham and Homsy and the linear function at low concentrations. However, the latter two are clearly only valid at concentrations lower than 10%. Although the function proposed by Barnea (Equation 2.10) behaves very different from the one by Zaki at low concentrations, they approach similar values at high concentrations.

In general, there have not been a standard hindered settling function for all ranges of volume fraction c. Functions derived from empirically fitting the experimental data take different forms depending on the particle size, volume fraction used and experimental conditions. Since Equation 2.11 has been widely used in other particle laden flow studies to account for the hindered settling velocity, and it is valid for large range of volume fractions, it will be used in our study.

2.3 Particle Velocity Fluctuation

In a colloidal suspension, when the particles are large enough, hydrodynamic interactions between particles prevail over brownian motion. In such a noncolloidal suspension of volume fraction c, the velocity of an individual particle fluctuates about the

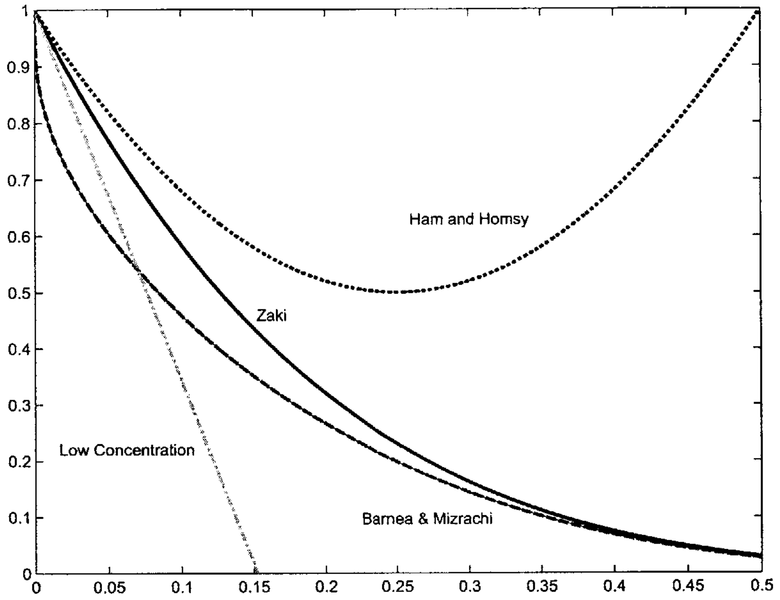

Figure 2-1: *Plots of hindered settling velocity functions against volume fraction of particles*

mean settling velocity. Differences in individual particle velocities about the mean settling velocity arise from local density fluctuations that occur during sedimentation.

In recent years, several apparently conflicting theories and experiments describing the amplitudes of the velocity fluctuations have been reported. On the one hand, simple theoretical arguments [10] as well as computer simulations [42] have indicated that the magnitudes of such fluctuations diverge with increasing cell size. The velocity fluctuation δV varies with cell dimension L as $\delta V \propto L^{1/2}$. On the other hand, two different types of experiments have been performed, both finding an independence of the fluctuations on system size. Ham and Homsy [28] and Nicolai *et al.* [26] studied the diffusion of a colored test particle during sedimentation, and the results demonstrated that the diffusivity did not vary with system size when the smallest dimension of the cell was varied by a factor of 4 at fixed c. A second type of experiment was performed by Segré, Herbolzheimer, and Chaikin [53], who used particle image velocimetry to record the velocity field in the center of the experimental cell. They found that by increasing the largest dimension of their cell, the size of the velocity fluctuations saturated, with an explicit dependence of fluctuations on the solid volume fraction c over three orders of magnitude in c. Their principal results are that: (1) the velocity fluctuations saturate at a scale of order $V_s c^{1/3}$; (2) the correlation length is of order $30ac^{-1/3}$, where a is the particle radius; and (3) velocity fluctuations saturate for systems larger than approximately ten times the correlation length.

The above brief discussions on velocity fluctuations demonstrate that the problem is very complex, and therefore it will be extremely hard to incorporate the effect in our analysis. For our simplified model, velocity fluctuations will not be taken into account.

2.4 Viscous Resuspension

When a fluid flows past an initially settled bed of heavy, non-Brownian particles, at least part of the sediment layer will resuspend and the flowing suspension will acquire a non-uniform concentration profile. This phenomenon, termed viscous resuspension, was first reported by Gadala-Maria [21] and was further investigated by Leighton and Acrivos [43].

Gadala-Maria reported the puzzling observation that, at very high solids concentration $c > 0.40$, the effective viscosity of the suspensions, as measured in the conventional Couette viscometer decreased slowly with prolonged shearing and eventually reached an equilibrium value which then remained time independent. According to Leighton and Acrivos, a test particle in a concentrated suspension being sheared undergoes a random walk as it interacts with neighboring particles and thereby acquires a net drift velocity from regions of high particle concentration to low and from regions of high shear to low. The resulting shear-induced particle flux opposes that due to gravity and a steady-state particle concentration profile is attained under proper conditions.

Acrivos, Mauri and Fan [1] studied the shear-induced resuspension in a couette device. They also derived a useful formula relating resuspended layer height and the height of the settled layer in the absence of shear and resuspension.

$$\frac{h}{h_0} = [1 + (BA^{1/3})^{0.93}]^{1/0.93} \tag{2.12}$$

where h_0 denotes the initial height of the settled layer, h denotes the height of the interface between the resuspended layer and the pure fluid, $B = 1/4(6c_m)^{2/3} \approx 0.574$, and A, a dimensionless parameter, represents the ratio between viscous and buoyancy forces.

$$A = \frac{9}{2}\frac{\mu\dot{\gamma}}{2g(\rho_s - \rho)h_0} \tag{2.13}$$

Here, $\dot{\gamma}$ is the shear rate.

In this chapter, some of the physical phenomena associated with particle concentrations have been presented. Some of the relationships discussed will be used in our formulation in the next chapter, others are too complicated to be included in our current study. Nevertheless, these results presented here may be useful for future considerations.

Chapter 3

Experimental Procedures and Results

Benjamin Dupuy [16] performed a series of particle laden flow experiments with an inclined plane with different inclination angles and particle volume concentrations.

3.1 Experimental Set-up

An acrylic sheet 120-cm long, 30-cm wide and approximately 1cm thick held by two horizontal aluminum bars was used. The sheet can be set at an angle between 0^o and 60^o from the horizontal. The choice of a wide channel helps to reduce the effect of the lateral boundaries on the flow. The suspension mixture flows from a reservoir through a gate whose opening can be precisely controlled. Different fluxes can be applied by adjusting the opening of the reservoir. Figure 3-1 shows a picture of the experimental setup.

Two fluids of different wetting properties were used in the experiments. Silicon oil, a wetting fluid, has viscosity $1000cSt$, density $970kg.m^{-3}$ and surface tension $21.2mN.m^{-1}$. The second fluid used was glycerin, which has a high static contact angle on plexiglass and is partially wetting. Compare to silicon oil, glycerin is able to absorb water from atmosphere and consequently change its viscosity. Therefore, its viscosity was carefully measured before each run. Glycerin used has a surface tension

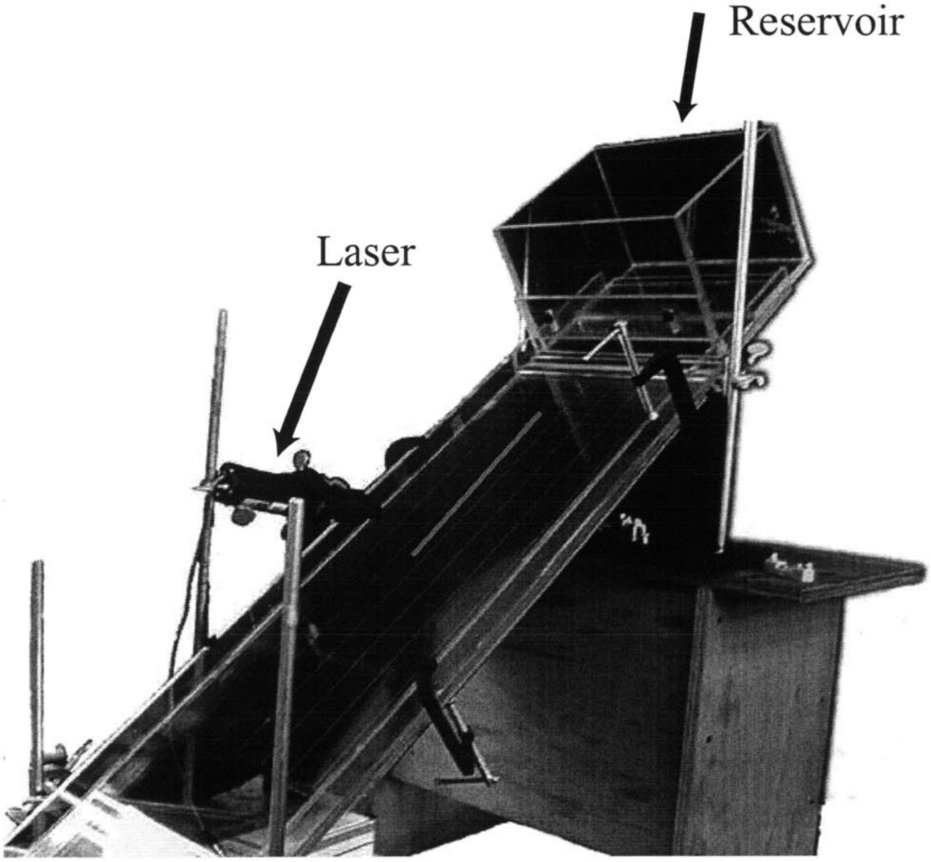

Figure 3-1: *Picture of the apparatus (Source: Benjamin Dupuy [16])*

of approximately $63.4 mN.m^{-1}$.

The particles used were glass spheres with different diameters, varying from 60 to 400 microns. These glass beads have a refraction index of 1.56, and a density of 2.6. Therefore, the particles are always heavier than either silicon oil or glycerin, and will tend to sediment when mixed. Details of experimental procedures and methods for data acquisition are described in Benjamin Dupuy's master thesis [16].

3.2 Results and Discussion

Benjamin Dupuy observed different flow regimes and instability behaviors, depending on the angle of inclination, particle size and volume fraction. This section summarizes the most important results and gives an insight into how these parameters can affect the flow.

Glass beads of sizes $60\mu m$ to $450\mu m$ were used in the experiments. It was found for small glass beads with diameters between $106\mu m$ and $212\mu m$, whatever the angle or volume fraction within the suspension, the ratio of wavelength over thickness always follows a $-1/3$ power law as predicted by Huppert for clear viscous fluids. Since glass beads are small, sedimentation is almost negligible and the beads are simply carried by the flow. Therefore, the suspension behaves like a clear fluid with only a shift in its density and viscosity.

On the other hand, if very big glass beads are used, over the timescale of the experiment, they sediment out. Fingers will then be formed from the resulting clear fluid. In general, two time scales are competing in these flows: the time for the particles to sediment, and the time for the fingers to develop. It was found from experiments that particles of sizes between $250\mu m$ and $425\mu m$ in diameter fall in this intermediate regime, where the two time scales are on the same order.

Sedimentation rate is faster for small volume fractions as explained in Section 2.2. It was observed that particles of $250\mu m$ to $425\mu m$ exhibit different flow patterns when the volume fraction is varied. For low concentrations (typically less than 30%), particles gradually sediment out as the suspension flows down the incline. At some point, the fluid loses all of its suspended particles and only the ambient fluid flows on the plane and finally breaks into fingers. For medium range of volume fraction, sedimentation time is longer, and fingers of the suspension form. In this case, beads are dragged into the fingers by the flow. Benjamin also noticed that the flow at which two fingers coalese is not as fast as the flow in the tip of a finger. For very high volume fraction close to the maximum packing concentration, the flow does not finger first but evolve into a ridge whose thickness can reach more thean twice the thickness of the upstream layer. The ridge starts to form after the flow has traveled a long distance, and when it forms, the flow slows down. Finally, the ridge reaches a crictical thickness and breaks into irregular large fingers. Figure 3-2 illustrates the different regimes observed in the experiments with different volume fraction.

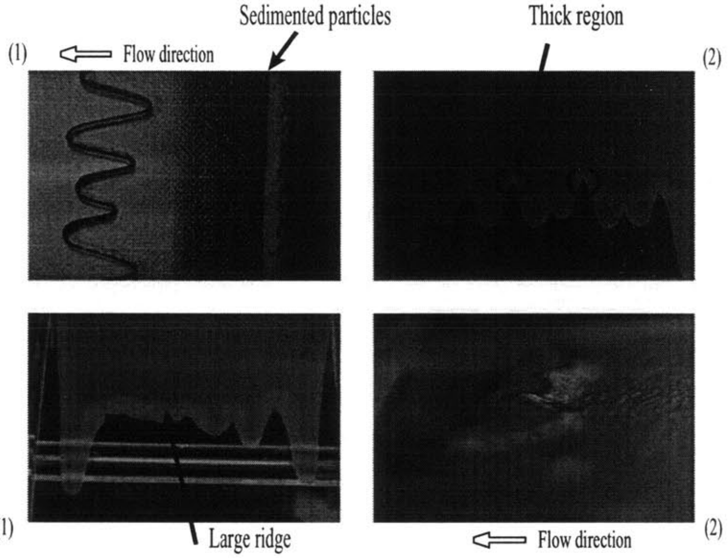

Figure 3-2: ***top:*** *(1) sedimentation and fingers of clear fluid, (2) fingers of suspension;* ***bottom:*** *(1) top view of ridge structure, (2) side view (Source: Benjamin Dupuy [16])*

As expected, not only volume fraction affects the flow; angle of the inclination also plays an important role. Flows are faster on slopes with large inclination angles while the sedimentation rate is unaffected by the slope angle. For high angles, mixture flow rate is faster than the particle sedimentation rate, and a ridge structure tends to be formed. On the other hand, the flow on slopes of low inclination is relatively slow and particles have ample time to sediment out. In this case, fingers of clear fluid are more likely to form.

Summing up the effects of both inclination angle and particle volume fraction, Benjamin produced a very nice phase diagram as shown in Figure 3-3. In general, below a given volume fraction, typically on the order of 25%, sedimentation occurs before the instability whatever the slope angle. For volume fractions between 25% and 30%, only two regimes are possible: instability of clear fluid and suspension. Above 30%, ridge structure can be formed on slopes of sufficiently large inclination.

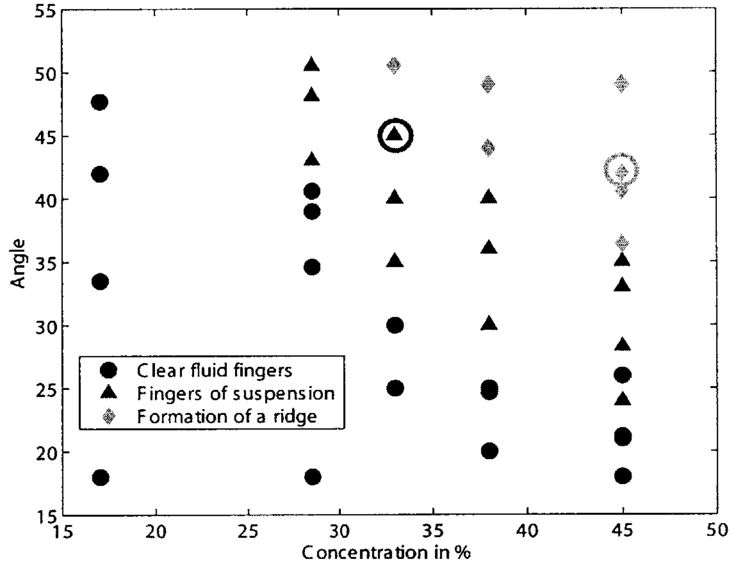

Figure 3-3: *Phase diagram of angle vs. concentration with corresponding flow regimes for 250-425 μm glass beads (Source: Benjamin Dupuy [16])*

Benjamin also commented on the depth profiles for different flow regimes based on his experimental data. In the suspension regime where sedimentation rate and mixture flow rate are comparable, an initially flat front quickly develops into hump which becomes more and more pronounced as fingers grow. However, Benjamin noted that because the range in the flow direction was limited due to the lens used, he did not observe a plateau just before the hump as reported in [44]. In the last regime where a ridge is seen, the height of the front can grow as high as three times the depth upstream. This height growth is remarkable, and it has never been observed in pure viscous fluid.

Chapter 4

Model Formulation

We study particle laden flow down an inclined plane under gravity. A sketch of the geometry of the problem is shown in Figure 4-1. The angle of inclination is denoted by β, and the particle volume fraction, or concentration is denoted by α. The flow is subject to gravitational force, which has a component normal to the plane and a component in the direction of the flow. As introduced earlier in Chapter 3, the particles are carried down by the mixture, and at the same time, they are settling down onto the bed. Therefore, the settling velocity also has two components: one parallel to the flow and one normal to the flow direction.

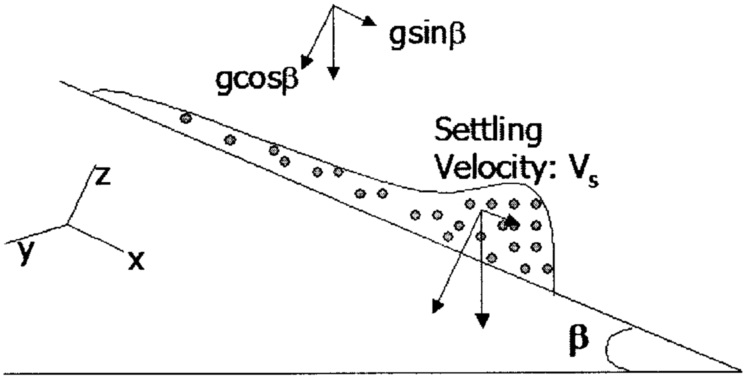

Figure 4-1: *Sketch of the particle laden flow down an inclined plane*

Fluid flowing down an inclined plane consists of two constituents: a dispersed phase made up of equally sized particles and a continuous phase which is taken to be an incompressible homogeneous fluid. Two possible continuum models can be applied to describe the macroscopic motion of the mixture. Both models rely on averaging techniques and are only able to resolve length and time scales much larger than those associated with the motion of a single particle. The "two fluid" model consists of two coupled sets of conservation laws for the dispersed and the continuous phases. On the other hand, the "mixture" model considers the entire particle-fluid system as a single fluid with an effective macroscopic viscosity and density. The "mixture" model is generally easier to implement and past studies on sand-water mixtures have successfully used the "mixture" model to capture the behavior of the system. Therefore, we choose to use the "mixture" model in our study.

4.1 Kinematic Relations

In Sec. 4.1 - Sec. 4.5, we follow the derivation outlined in M. Nigam's thesis work [48]. The equations are expressed in terms of volume averaged flux densities [48], which in short will be referred to as volume flux. In order to distinguish between volume averaged flux and mass averaged flux, the former are hereafter denoted by $\mathbf{j}$ and the latter by $\mathbf{v}$. Moreover, subscripts C, D and R refer to the continuous (homogeneous viscous fluid) phase,the dispersed (particle) phase, and the relative motion between the two phases respectively.

The density of the mixture is given by

$$\rho = \alpha\rho_D + (1-\alpha)\rho_C = (1+\Delta\alpha)\rho_C \tag{4.1}$$

where

$$\Delta = \frac{\rho_D - \rho_C}{\rho_C} \tag{4.2}$$

is the relative density difference between the two phases. Note that in Equation 4.1, $\alpha = 0$ represents the case where there are no particles, and the expression gives ρ_C, the density of the pure fluid. On the other hand, if there are only particles, $\alpha = 1$ gives the density of the particle ρ_D.

The volume flux and the mass flux are related by

$$\mathbf{j}_D = \alpha \mathbf{v}_D \tag{4.3}$$

$$\mathbf{j}_C = (1-\alpha)\mathbf{v}_C \tag{4.4}$$

The volume averaged flux and mass averaged flux of the entire mixture can then be expressed as

$$\mathbf{j} = \mathbf{j}_D + \mathbf{j}_C \tag{4.5}$$

$$\mathbf{v} = \frac{\alpha \rho_D \mathbf{v}_D + (1-\alpha)\rho_C \mathbf{v}_C}{\rho} \tag{4.6}$$

Flow quantities describing the relative motion between the two phases are defined by the following relationships

$$\mathbf{v}_R = \mathbf{v}_D - \mathbf{v}_C \tag{4.7}$$

$$\mathbf{j}_R = \alpha(1-\alpha)\mathbf{v}_R \tag{4.8}$$

Note that relative volume flux $\mathbf{j}_R$ and relative mass flux $\mathbf{v}_R$ are related by a factor $\alpha(1-\alpha)$. This reflects the fact that the relative motion is not associated with any single phase, but is affected by the volume fraction of both phases. $\mathbf{j}_R = 0$ when $\alpha = 0$ or $\alpha = 1$. This makes sense as there is no relative motion when only fluid or only particles are present. Another useful relationship relating relative volume flux, mixture total flux and particle flux is given by

$$\mathbf{j}_D = \mathbf{j}_R + \alpha \mathbf{j} \tag{4.9}$$

4.2 Continuity Relation

The conservation laws are presented using a fixed control volume **V** with surface **S** and outward surface normal $\hat{\mathbf{n}}$. Since there are no sources or sinks for the particles, the volume fraction of the dispersed phase in **V** changes only due to the flux of particles through the surface **S**.

$$\frac{\partial}{\partial t}\int_V \alpha dV = -\oint_S \alpha \mathbf{v}_D \cdot \hat{\mathbf{n}} dS \tag{4.10}$$

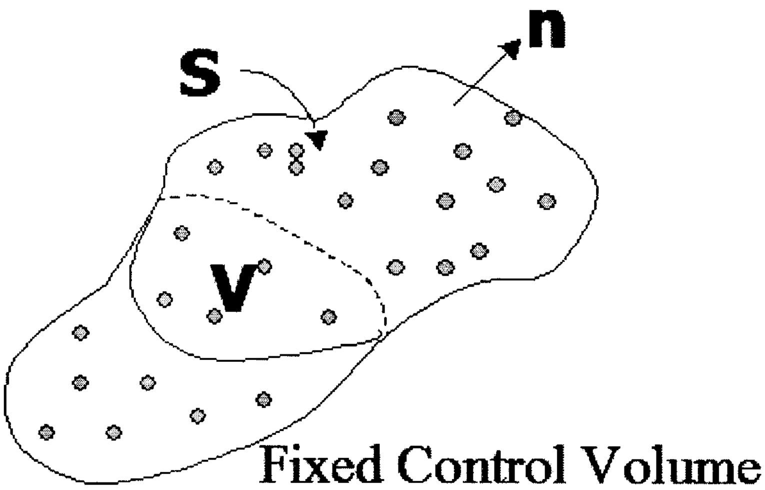

Figure 4-2: *Sketch of a fixed control volume*

Applying the divergence theorem to the surface integral and noting the fact that V is arbitrary, Equation 4.10 yields

$$\frac{\partial \alpha}{\partial t} + \nabla \cdot \mathbf{j}_D = 0 \tag{4.11}$$

Similarly, continuity of the continuous phase requires that

$$\frac{\partial}{\partial t}\int_V (1-\alpha)dV = -\oint_S (1-\alpha)\mathbf{v}_C \cdot \hat{\mathbf{n}}dS \tag{4.12}$$

Again, applying the divergence theorem to obtain the differential form

$$\frac{\partial(1-\alpha)}{\partial t} + \nabla \cdot \mathbf{j}_C = 0 \tag{4.13}$$

Adding Equations 4.11 and 4.13 gives the expression for the conservation of the mixture volume

$$\nabla \cdot (\mathbf{j}_D + \mathbf{j}_C) = 0 \longrightarrow \nabla \cdot \mathbf{j} = 0 \tag{4.14}$$

Equation 4.14 shows that the volume flux of the mixture is divergence free. In the single incompressible homogeneous fluid case, mass flux has the continuity relationship. In the particle-fluid mixture case, rather than the mass flux, continuity holds for the volume flux. For this reason, volume flux will be chosen as principal unknown variables in later part of the formulations.

4.3 Conservation of Mixture Momentum

The total momentum in the control volume V changes due to the flux of momentum through the surface S and due to the action of surface stress and body forces.

$$\begin{aligned}&\frac{\partial}{\partial t}\int_V(\rho_D\alpha\mathbf{v}_D+\rho_C(1-\alpha)\mathbf{v}_C)dV+\oint_S(\rho_D\alpha\mathbf{v}_D\mathbf{v}_D+\rho_C(1-\alpha)\mathbf{v}_C\mathbf{v}_C)\cdot\hat{\mathbf{n}}dS\\ =\;&\oint_S\underline{\underline{\Sigma}}\cdot\hat{\mathbf{n}}dS+\int_V(\rho_D\alpha+\rho_C(1-\alpha))\mathbf{g}\;dV \qquad (4.15)\end{aligned}$$

Here, $\underline{\underline{\Sigma}}$ is the surface stress acting on S, and $\mathbf{g}$ is the body force acting on the mixture, which in this case is gravity. The terms on the left side of the equation are inertial terms and are essentially negligible in low Reynolds number flow. Removing the inertial terms and applying the kinematic relations derived in Section 4.1, momentum equation is simplified to

$$\frac{1}{\rho_C}\nabla\cdot\underline{\underline{\Sigma}}+(1+\Delta\alpha)\mathbf{g} \qquad (4.16)$$

The stress tensor is specified by

$$\underline{\underline{\Sigma}}=-p\underline{\underline{I}}+\mu_C\mu(\alpha)[\nabla\mathbf{j}+(\nabla\mathbf{j})^T] \qquad (4.17)$$

Here, p is the pressure and $\mu(\alpha)$ is the effective suspension viscosity due to the presence of the particles. Depending on the shear rate, the maximum packing fraction α_M ranges from 0.57 to 0.68 (Refer to Equation 2.6 in Chapter 2). It should be emphasized that these expressions and constants are empirically derived and approximations are incurred when applying these relationships. In this paper, it is assumed that

$$\mu(\alpha)=(1-\frac{\alpha}{\alpha_M})^{-n} \qquad (4.18)$$

where α_M, the maximum packing fraction, is taken to be 0.67 and n is 2. Substituting equations 4.17 and 4.18 into equation 4.16, the final form of the momentum equation is

$$-\frac{1}{\rho_C}\nabla p+\nu_C\nabla\cdot[\mu(\alpha)(\nabla\mathbf{j}+(\nabla\mathbf{j})^T)]+(1+\Delta\alpha)\mathbf{g}=0 \qquad (4.19)$$

4.4 Closure for the Relative Volume Flux

Assuming that the particles in this gravity driven flow are in creeping motion relative to the fluid, a closure for the relative flux can be sought in terms of modified Stokes flow. General Stokes flow velocity can be derived by balancing the viscous force and the buoyancy force acting on a particle.

$$6\pi\mu_C r\mathbf{v}_R = (\rho_D - \rho_C)\frac{4\pi r^3}{3}\mathbf{G} \tag{4.20}$$

where r is the radius of the particle and **G** is the effective particle accel

Equation 4.20 is only able to describe the motion of a single particle. Results of many sedimentation experiments reported in the literature have shown that the settling velocity is related to a function $f(\alpha)$ involving volume fraction α. We have discussed some empirically determined hindered sedimentation functions in Section 2.2. For our low Reynolds number flow, we will use the most widely used empirical correlation proposed by Richardson & Zaki(1954) [56]

$$f(\alpha) = (1-\alpha)^k \tag{4.21}$$

where, k is taken to be 5. Although fifth power has generally been assumed in past studies on suspension flows, for example studies done by Brady et al [11], it should be kept in mind that this power constant can vary depending on volume fraction. Once again, this relation is largely empirical and is only an approximation.

So, instead of using the effective viscosity $\mu(\alpha)$ to model the increased viscous force on a single particle, we will treat the sedimentation rate of a cluster of particles by multiplying the sedimentation rate of a single particle by $f(\alpha)$ to obtain the hindered sedimentation rate. Combining the kinematic equation 4.8, The closure for the relative volume flux is obtained

$$\mathbf{j}_R = \frac{2\Delta r^2}{9\nu_C}\alpha f(\alpha)\mathbf{g} \tag{4.22}$$

Note that the $(1-\alpha)$ term in Equation 4.8 has been absorbed into $f(\alpha)$, and $f(\alpha) = (1-\alpha)^6$.

4.5 Summary of Kinematic Relations and Conservation Laws

We have derived a set of kinematic relations and conservation laws in the previous sections. In summary, below is the set of equations that have been derived and will be used for our model:

$$\begin{aligned}
-\frac{1}{\rho_C}\nabla p + \nu_C \nabla \cdot [\mu(\alpha)(\nabla \mathbf{j} + (\nabla \mathbf{j})^T)] + (1+\Delta\alpha)\mathbf{g} &= 0 && (4.23)\\
\nabla \cdot \mathbf{j} &= 0 && (4.24)\\
\frac{\partial \alpha}{\partial t} + \nabla \cdot \mathbf{j}_D &= 0 && (4.25)\\
\mathbf{j}_D &= \mathbf{j}_R + \alpha \mathbf{j} && (4.26)\\
\mathbf{j}_R &= \frac{2\epsilon r^2}{9\nu_C}\alpha f(\alpha)\mathbf{g} && (4.27)
\end{aligned}$$

The effective density of the mixture and the effective viscosity of the mixture are given by

$$\begin{aligned}
\rho &= \rho_C \rho(\alpha) = \rho_C(1+\Delta\alpha) && (4.28)\\
\mu &= \mu_C \mu(\alpha) = \mu_C(1-\frac{\alpha}{\alpha_M})^{-n} && (4.29)
\end{aligned}$$

Where the maximum packing constant α_M is 0.67, and the exponent $n = 2$.

Sedimentation rate is hindered when there is a cluster of particles. The function that modifies the sedimentation rate takes the form

$$f(\alpha) = (1-\alpha)^m \qquad (4.30)$$

Where the constant m is taken to be 6.

4.6 Reduction of Momentum Equations

Although the momentum equation has been simplified by assuming low Reynolds number flow, the final form Equation 4.23 is still too complicated and difficult to be

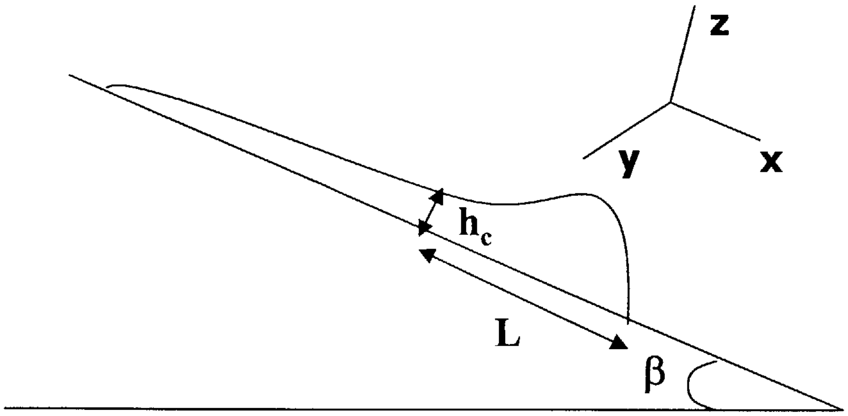

Figure 4-3: *Flow geometry and length scales*

addressed by either analytical or numerical means. There is, however, one property of all thin film flows that can be used for significant simplifications.

$$\begin{aligned}\frac{\partial j_x}{\partial x} \approx \frac{\partial j_y}{\partial y} &\approx \frac{\partial j_z}{\partial z} \\ \frac{1}{L}\frac{\partial j_y}{\partial \overline{y}} &\approx \frac{1}{h_c}\frac{\partial j_z}{\partial \overline{z}}\end{aligned} \tag{4.31}$$

where h_c and L are normal direction length scale and in-plane length scale respectively as shown in Figure 4-3. Since $h_c \ll L$, the normal component of the flux is much smaller than the in-plane ones and it can be safely neglected.

Next, the second derivative of the in-plane flux are rewritten as

$$\frac{\partial^2 j_x}{\partial x^2} \approx \frac{\partial^2 j_x}{\partial y^2} = \frac{1}{L^2}\frac{\partial^2 j_x}{\partial \overline{x}^2} \ll \frac{1}{h_c^2}\frac{\partial^2 j_x}{\partial \overline{z}^2} = \frac{\partial^2 j_x}{\partial z^2} \tag{4.32}$$

Therefore, the in-plane derivative can be ignored for both components of the in-plane flux.

To simplify the viscous stress tensor in the momentum equation, one last assumption is made: change of viscosity along the normal direction is negligible, and $\mu(\alpha) = \mu(\alpha)(x, y, t)$ only.

Applying these simplifications to the viscous stress tensor and write the momentum equation in in-plane and normal directions

$$\nabla_2 p = \mu \frac{\partial^2 \mathbf{j}_2}{\partial z^2} + \rho \mathbf{g}_2 \tag{4.33}$$

$$p_z = \rho \mathbf{g}_z \tag{4.34}$$

where $\nabla_2 = (\partial_x, \partial_y)$ and $\mathbf{j}_2 = (j_x, j_y)$. μ and ρ are effective viscosity and density of the mixture respectively as defined previously. The body forces acting on the mixture is the gravitational force in this case. If the coordinate system is setup as shown in Figure 4-1, the above equations can be rewritten as

$$\nabla_2 p = \mu \frac{\partial^2 \mathbf{j}_2}{\partial z^2} + \rho g \sin\beta \mathbf{i} \tag{4.35}$$

$$p_z = -\rho g \cos\beta \tag{4.36}$$

Equation 4.36 can be easily integrated to yield an expression for p. This expression follows from the so-called Laplace-Young boundary condition, which states that at the fluid-air interface, $z = h(x, y)$, the pressure is $p(h) = -\gamma\kappa + p_o$, where κ is the curvature of the boundary, γ is the surface tension, and p_o is the atmospheric pressure in the air phase.

$$p = -\rho g(z - h)\cos\beta - \gamma\kappa + p_o \tag{4.37}$$

Next, substitute equation 4.37 into equation 4.36 and integrate twice with respect to z. Note that $h = h(x, y), \rho = \rho(x, y)$ and define $P = \rho g h \cos\beta - \gamma\kappa$.

$$\mathbf{j}_2 = \frac{1}{\mu}\nabla_2 P \frac{z^2}{2} - \frac{g}{\mu}\cos\beta \nabla_2 \rho \frac{z^3}{6} - \frac{\rho g}{\mu}\sin\beta \frac{z^2}{2}\mathbf{i} + Az + B \tag{4.38}$$

Where A and B are integration constants.

To proceed, boundary conditions are needed. At $z = 0$, specify the no-slip condition $|\mathbf{j}_2| = 0$. At the fluid-air boundary, since the air phase is essentially inviscid compared to the fluid phase, continuous stresses requirement leads to $\partial \mathbf{j}_2/\partial z|_{z=h(x,y)} = 0$. Apply these BCs to find the constants A and B, rearrange the flux equation to yield

$$\mathbf{j}_2 = (\frac{1}{\mu}\nabla_2 P - \frac{\rho g}{\mu}\sin\beta \mathbf{i})(\frac{z^2}{2} - hz) - \frac{g}{6\mu}\cos\beta(z^3 - 3h^2 z)\nabla_2 \rho \tag{4.39}$$

From this point on, write j for $\mathbf{j}_2$ and write ∇ for ∇_2. Since it is hard to measure flux in the normal direction because the film is very thin, and we are interested in how flux varies along the plane, average flux over z-direction to remove its z-dependence. Define the average flux $\langle \mathbf{j} \rangle = \langle \mathbf{j} \rangle (x, y)$ as

$$\begin{aligned} \langle \mathbf{j} \rangle &= \frac{1}{h} \int_o^h \mathbf{j}\, dz \\ &= -\frac{h^2}{3\mu}(\nabla P - \rho g \sin \beta \mathbf{i}) + \frac{5h^3}{24\mu} g \cos \beta \nabla \rho \end{aligned} \tag{4.40}$$

4.7 Thin Film and Particle Conservation Equations

In our problems, we have 2 principal unknowns: the height of the film h and the particle volume fraction α. Other quantities such as density and viscosity are all functions of α, and their values at a point are known if α is known at that point. We have assumed that the variations in the z-direction are negligible, and the properties are taken to be uniform in the direction normal to the plane. So, $h = h(x, y, t)$ and $\alpha = \alpha(x, y, t)$ only. Since we have 2 unknowns, we will need 2 equations.

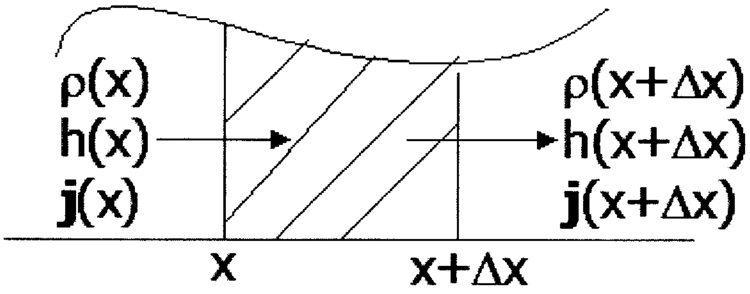

Figure 4-4: *Conservation of mass in a fixed control volume*

We have found an expression for the average flux of the flow at any point in Equation 4.40. Using this average flux, we can derive the usual thin film equation by applying the conservation of mass. We consider a fixed control volume as shown in

Figure 4-4, the mass per unit area is ρh, and the rate of change of mass per unit area is equal to the difference in the flux of mass across the surface per unit area.

$$\frac{\partial(\rho h)}{\partial t} + \nabla \cdot (\rho h \langle \mathbf{j} \rangle) = 0 \tag{4.41}$$

Substitute the average flux expression into equation 4.41

$$\frac{\partial(\rho h)}{\partial t} + \nabla \cdot \{\frac{-\rho h^3}{3\mu}(\nabla \mathbf{P} - \rho g \sin\beta \mathbf{i}) + \frac{5\rho h^4}{24\mu} g \cos\beta \nabla \rho\} = 0 \tag{4.42}$$

Recall the definition of $\mathbf{P}$ and approximate the curvature of the fluid-air interface by $\kappa \approx \nabla^2 h$ to yield

$$\frac{\partial(\rho h)}{\partial t} + \frac{1}{3}\nabla \cdot \{\underbrace{\frac{\gamma \rho h^3}{\mu}\nabla\nabla^2 h}_{\mathbf{I}} - \underbrace{\frac{\rho h^3}{\mu} g \cos\beta \nabla(\rho h)}_{\mathbf{II}} + \underbrace{\frac{5\rho h^4}{8\mu} g \cos\beta \nabla \rho}_{\mathbf{III}} + \underbrace{\frac{\rho^2 h^3}{\mu} g \sin\beta \mathbf{i}}_{\mathbf{IV}}\} = 0 \tag{4.43}$$

Equation 4.43 is the so-called thin film equation. It resembles the classical Newtonian thin film equation, except that it has extra density gradient terms due to varying density. The terms labeled are:

I: Surface tension term that is responsible for the bump in the viscous fluid case

II,III: Normal Component of Gravity terms

IV: Gravity term in the flow direction

The thin film equation describes the height evolution of the mixture flow as it moves down the inclined plane. Since the particles are present in our problem, their concentration and consequently the mixture properties change as the film evolves. We can apply the same conservation law, but this time on the number of particles in a fixed control volume.

Consider a small volume of fluid along the plane from x to $x + \Delta x$, rate of change of total number of particles in this small volume is equal to the difference between number of particles flowing in and number of particles leaving per unit time. Number of particles per unit width is αh and particle flux $\mathbf{j}_D$ can be found using equations 4.26 and 4.27.

$$\frac{\partial \alpha h}{\partial t} + \nabla \cdot [(\mathbf{j}_R + \alpha \mathbf{j})h] \tag{4.44}$$

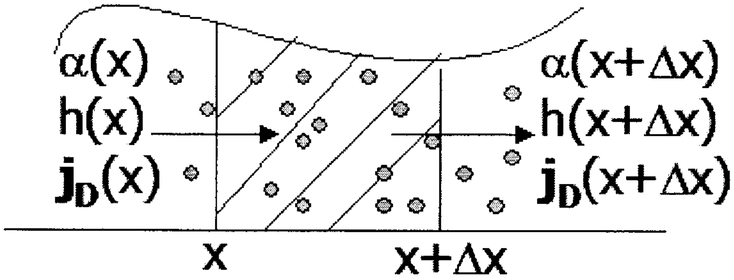

Figure 4-5: *Conservation of particles in a fixed control volume*

The relative flux $\mathbf{j}_R$ derived from modified stokes velocity really carries two orthogonal components: the component parallel to the flow that accounts for the particles being carried with the mixture down stream, and the component normal to the plane that represents the particles settling down onto the bed. There are several issues if we try to incorporate the normal component into our model. First, if particles leave the system and settle down onto the bed, it is expected that there are likely more particles near the bottom than those at the top. This will raise questions regarding our assumption that particles are essentially uniformly distributed across the thickness of the film. Secondly, if the particle concentration is higher at the bottom, then it is not accurate to calculate the normal component of the settling rate based on a depth averaged volume fraction. It is also possible that some of the particles that have settled out are brought back into the flow due to resuspension (see Section 2.4). In view of these complexities, we will leave the normal component of the relative flux out for the moment. Therefore, our current reduced model best describes the regime observed in Benjamin's experiments with high inclination angle and high volume fraction, where essentially all particles are carried downstream with the mixture.

Substituting in the average value for $\mathbf{j}$ and including only the relative flux component parallel to the plane, we arrive at the following particle equation

$$\begin{aligned}\frac{\partial(\alpha h)}{\partial t} &+ \frac{1}{3}\nabla\cdot\{\frac{\gamma\alpha h^3}{\mu}\nabla\nabla^2 h - \frac{\alpha h^3}{\mu}g\cos\beta\nabla(\rho h) + \frac{5\alpha h^4}{8\mu}g\cos\beta\nabla\rho \\ &+ \frac{\alpha\rho h^3}{\mu}g\sin\beta\mathbf{i} + \underbrace{\frac{2r^2\Delta}{3\nu_C}\alpha f(\alpha)hg\sin\beta\mathbf{i}\}}_{\mathbf{V}} = 0 \qquad (4.45)\end{aligned}$$

The term labeled **V** is the term resulting from the component of the hindered settling velocity parallel to the flow.

4.8 Nondimensionalization

The first step in solving Equation 4.43 and Equation 4.45 is to put them in nondimensional form. First, we assume that there is no variation in the y-direction, which is generally true for the flow before the onset of instability. Therefore, our space derivative only involves x-derivative. Next, we scale the fluid height, h, by the thickness far behind the front h_c. Next, we rescale the in-plane distance x by x_c and the time t by t_c through carefully balancing the terms in the equations. Balancing the capillary term (**I**) with the gravity piece (**IV**) specifies the appropriate choice for the in-plane length scale x_c. The requirement that the time derivative term on the left of Equation 4.43 is of the same order of the terms on the right-hand side of the same equation yields the time scale, t_c:

$$x_c = (\frac{a^2 h_c}{sin\beta})^{1/3} \tag{4.46}$$

$$t_c = \frac{3\mu_C}{\gamma}\frac{a^2 x_c}{{h_c}^2 sin\beta} \tag{4.47}$$

The quantity $a = \sqrt{\gamma/\rho_C g}$ is the capillary length. This is the length-scale at which the capillary effects become important relative to gravitational ones. Moreover, the velocity scale is chosen naturally as $U = x_c/t_c$ and the capillary number is defined as $Ca = \mu U/\gamma$. The quantity Ca measures the importance of the viscous force relative to those resulting from surface tension. Using this nondimensionalization, we obtain that

$$\frac{\partial(\rho(\alpha)h)}{\partial t} + \{\frac{\rho(\alpha)}{\mu(\alpha)}h^3 h_{xxx} - D(\beta)[\frac{\rho(\alpha)}{\mu(\alpha)}h^3(\rho(\alpha)h)_x - \frac{5}{8}\frac{\rho(\alpha)}{\mu(\alpha)}h^4(\rho(\alpha)_x)] + \frac{\rho(\alpha)^2}{\mu(\alpha)}h^3\}_x = 0 \tag{4.48}$$

$$\frac{\partial(\alpha h)}{\partial t} + \{\frac{\alpha}{\mu(\alpha)}h^3 h_{xxx} - D(\beta)[\frac{\alpha}{\mu(\alpha)}h^3(\rho(\alpha)h)_x - \frac{5}{8}\frac{\alpha}{\mu(\alpha)}h^4(\rho(\alpha)_x)] + \frac{\alpha\rho(\alpha)}{\mu(\alpha)}h^3 + \frac{2}{3}V_s\alpha h f(\alpha)\}_x = 0 \tag{4.49}$$

In the above, $\rho(\alpha) = 1+\Delta\alpha$ and $\mu(\alpha) = (1-\alpha/\alpha_M)^{-2}$ are as defined in Equations 4.28 and 4.29. The two dimensionless parameters $D(\beta)$, V_s are defined as

$$D(\beta) = (3Ca)^{1/3}\cot(\beta) \tag{4.50}$$

$$V_s = r^2\Delta/h_c^2 \tag{4.51}$$

r is the radius of the particles used. $D(\beta)$ measures the size of the normal component of gravity. V_s, the dimensionless settling velocity, measures the stokes velocity. The 2 equations: 4.48 and 4.49 completely describe the change of film thickness and particle concentration as the mixture flows down the inclined plane. They will be used for our numerical simulation.

4.9 Numerical Methods

In order to obtain complete solutions of the governing equations: 4.48 and 4.49, one has to resort to numerical techniques. These equations are of parabolic types; we discretize them using a finite-difference method and solve them by a fully implicit Newton scheme. We outline the discretization method and Newton solver technique in this section.

4.9.1 Space Discretization

The Equations 4.48 and 4.49 are of the form:

$$\frac{\partial(\rho h)}{\partial t} + [F(\alpha,h)]_x = 0 \tag{4.52}$$

$$\frac{\partial(\alpha h)}{\partial t} + [G(\alpha,h)]_x = 0 \tag{4.53}$$

Where $F(\alpha,h), G(\alpha,h)$ represent the terms in the space-derivative of the Equations 4.48 and 4.49 respectively. The computational domain of our problem is defined by $0 \leq x \leq L$, and discretized by the node points $x_i = i\Delta x, i = 0,\ldots,N$, where $\Delta x = L/N$. We will use Equation 4.52 to illustrate our space discretization and time discretization. $[F(\alpha,h)]_x$ is a a space derivative of $F(\alpha,h)$ at a point x_i, and we estimate the value by

$$[F(\alpha,h)]_x = \frac{[F(\alpha,h)]_{i+1/2} - [F(\alpha,h)]_{i-1/2}}{\Delta x} \tag{4.54}$$

Since we calculate and store values at discrete points x_i, to evaluate $F(\alpha,h)_{i+1/2}$, we estimate the value of a variable, for example h at $i+1/2$, by an average of the variable value at i, (h_i), and $i+1$, (h_{i+1}), and estimate the space derivative, for example h_x at $i+1/2$ by $(h_{i+1}-h_i)/\Delta x$. Here, we use the term in $F(\alpha,h)$: $(\rho(\alpha)/\mu(\alpha))h^3(\rho(\alpha)h)_x$ to illustrate the discretization method.

$$\{\frac{\rho(\alpha)}{\mu(\alpha)}h^3(\rho(\alpha)h)_x\}_{i+1/2} = \frac{(\rho(\alpha)_{i+1}+\rho(\alpha)_i)/2}{(\mu(\alpha)_{i+1}+\mu(\alpha)_i)/2}(\frac{h_{i+1}+h_i}{2})^3\frac{(\rho(\alpha)h)_{i+1}-(\rho(\alpha)h)_i}{\Delta x} \tag{4.55}$$

Using the method outlined above, we can discritize each low order terms with second-order accuracy. To complete the space discretization, we also need to find a way to discretize the 4th order surface tension term. The high order term is in $F(\alpha,h)_x$ and it takes the form $(\rho(\alpha)/\mu(\alpha))h^3h_{xxx}$. To discretize h_{xxx}, we define a new variable $f = h_{xx}$, so we have

$$\{\frac{\alpha}{\mu(\alpha)}h^3h_{xxx}\}_x = \{\frac{\alpha}{\mu(\alpha)}h^3f_x\}_x \tag{4.56}$$

$$f = h_{xx} \tag{4.57}$$

With this transformation, Equation 4.56 no longer involves high order term and it can be discretized using the method already outlined. We can discretize h_{xx} by

$$h_{xx} = \frac{h_{i+1}-2h_i+h_{i-1}}{(\Delta x)^2} \tag{4.58}$$

4.9.2 Time Discretization and Implicit Schemes

There are different schemes that can be used to solve the system of coupled ODEs. The simpler ones are explicit schemes, which use the values of h_i and α_i at time t to calculate the time derivative. This simplest possibility is the forward Euler scheme. The forward Euler scheme is easy to implement and solve since it uses known values at each time step. However, this scheme suffers from two problems. One is lacy of accuracy; it is only first order in time. This problem can be removed by using more accurate schemes, such as second-order Runge Kutta methods. A more serious issue is the fact that explicit schemes on diffusive systems may become unstable if the time step is too large. For our system, the stability requirement is that $\Delta t < C(\Delta x)^4$, where C is a constant (the fourth power is related to the fourth order term). Therefore, for small Δx, this requires rather small Δt. To circumvent this problem, we choose to use a implicit scheme.

Standard implicit schemes use the values of h_i and α_i not only at time t, but also at time $t + \Delta t$. If only values at time $t + \Delta t$ are used, the method is called fully implicit backward Euler scheme. If both values at time t and at time $t + \Delta t$ are used with equal weightage, the method is Crank-Nicholson scheme. The fully implicit backward Euler scheme is used in our numerical simulation and our system is thus formulated as

$$\frac{(\rho(\alpha)h)_i^{t+\Delta t} - (\rho(\alpha)h)_i^t}{\Delta t} + \frac{F(\alpha, h)_{i+1/2}^{t+\Delta t} - F(\alpha, h)_{i-1/2}^{t+\Delta t}}{\Delta x} = 0 \tag{4.59}$$

$$\frac{(\alpha h)_i^{t+\Delta t} - (\alpha h)_i^t}{\Delta t} + \frac{G(\alpha, h)_{i+1/2}^{t+\Delta t} - G(\alpha, h)_{i-1/2}^{t+\Delta t}}{\Delta x} = 0 \tag{4.60}$$

One commonly used approach to solving this kind of equations is Newton's method. Basically, one linearizes about a guess for the solution, and then solves the resulting "linear" system for the correction. The guess is then updated and this iterative procedure is repeated until the convergence criterion is met. In our problem, the two principal unknowns are α and h. If we denote $\bar{s}\ ^{t+\Delta t}$ as our guess solution for time $t + \Delta t$, where $\bar{s}\ ^{t+\Delta t} = (h_1, \alpha_1, \ldots, h_i, \alpha_i, \ldots, h_N, \alpha_N)\ ^{t+\Delta t}$. If the true solution is $s\ ^{t+\Delta t}$, then $s\ ^{t+\Delta t} = \bar{s}\ ^{t+\Delta t} + \Delta s$, and Δs is the correction. If we also denote the left hand side of the Equations 4.59 as H, then we have $H(s) = H(\bar{s} + \Delta s) = 0$. Linearization about the approximate solution, $\bar{s}$, yields

$$H(\bar{s} + \Delta s) = H(\bar{s}) + \frac{\partial H}{\partial s}|_{\bar{s}}\ \Delta s = 0 \tag{4.61}$$

$\partial H / \partial s$ is the Jacobian matrix, and it can be explicitly computed. At each new time step, we first guess the solution $\bar{s}\ ^{t+\Delta t}$ as $s\ ^t$. The guessed solution allows us to evaluate the Jacobian at this guess solution and calculate the correction Δs:

$$\Delta s = -\frac{\partial H}{\partial s}|_{\bar{s}}\ H(\bar{s}) \tag{4.62}$$

We use the computed correction Δs to update our guess $\bar{s}^{\,t+\Delta t}$, and this completes one Newton iteration. Next, we check whether Δs is sufficiently small (in the $|L^2|$ norm). If it is sufficiently small, the procedure to find the solution $s^{\,t+\Delta t}$ is completed and we move to the next time step. If not, the same procedure is repeated to perform more Newton iterations and update our guess after each iteration until the correction is small enough to meet the criterion.

4.9.3 Initialization and Boundary Conditions

As mentioned, all the theoretical and computational methods require to assume either a thin precursor film in front of the contact line or a no-slip boundary condition at fluid-solid interface. It has been shown that the results are rather insensitive to the choice of the model (Diez, Kondic, and Bertozzi [35]). However, the computational performance of the precursor film model was shown to be much better than that of various slip models. For this reason, we also use a precursor film of thickness b in this work.

Therefore, our model simulations are assigned an initial condition of uniform thickness and particle concentration upstream and same uniform concentration but small thickness downstream. Here, we assume that when the squeegee is applied to produce a thin precursor layer in the experiment, the precursor film retains the particle concentration. This is reasonable for our continuum model.

In the experiment, the mixture is released from a gate with a fixed opening. We assume that the mixture volume in the reservoir is very large such that the mixture flows out the gate at a constant rate throughout the experiment. Therefore at the gate, $x = 0$, we have

$$h = 1, \quad \alpha = \alpha_0$$

where α_0 is the initial concentration of the mixture. The height of the gate is taken to be 1.

To specify the boundary condition at far downstream, we note that the height of the film is the precursor thickness b. We further assume that the plate is infinitely long, so there is no particle leaving the end of the plate. This allows us to set zero flux as the boundary condition at downstream.

4.10 Normal Component of Settling Velocity

As previously discussed, it is rather difficult to model the normal component of the settling velocity in our model because we assume that there is no concentration change across the film depth. It is unlikely that the concentration is uniform if we have particles settling out from bottom of the fluid film. Nevertheless, if we retain the uniform concentration assumption, we can possibly include the normal settling effect in our model.

The settling velocity is expressed in Equation 4.27, and the gravitational acceleration $\mathbf{g}$ has two components, and we can rewrite 4.27 as

$$\mathbf{j}_R = \frac{2}{9}\frac{r_2\Delta}{\nu_C}\alpha f(\alpha)(g\sin\beta\ \mathbf{i} - g\cos\beta\ \mathbf{k}) \tag{4.63}$$

Conservation of particles in a control volume leads to

$$\frac{\partial \alpha}{\partial t} + \nabla\cdot\mathbf{j}_D = 0 \tag{4.64}$$

and particle flux $\mathbf{j}_D$ can be found by Equation 4.26. Combining these equations, we have

$$\frac{\partial \alpha}{\partial t} + \nabla\cdot(\mathbf{j}_R + \alpha\langle\mathbf{j}\rangle) = 0 \tag{4.65}$$

Next, we integrate the terms in the above equation from $z = 0$ to $z = h$, where h is the height of the free surface. This gives

$$(\int_0^h (\frac{\partial \alpha}{\partial t} + \nabla\cdot\alpha\langle\mathbf{j}\rangle)dz + \frac{2}{9}\frac{r_2\Delta}{\nu_C}\int_0^h \frac{\partial}{\partial x}(\alpha f(\alpha)g\sin\beta)dz) - \frac{2}{9}\frac{r_2\Delta}{\nu_C}\int_0^h \frac{\partial}{\partial z}(\alpha f(\alpha)g\cos\beta)dz \tag{4.66}$$

In the Equation 4.66, the terms in the parenthesis are the same terms that we already have in Equation 4.45. The first term is the average flux, and the second term is the settling velocity component parallel to the mixture flow. The last term is the added normal component of the settling velocity, and its integral can be evaluated

$$-\frac{2}{9}\frac{r^2\Delta}{\nu_C}g\cos\beta[\alpha f(\alpha)]_0^h \tag{4.67}$$

Since there are no particles flowing out from the top, a reasonable assumption is that there is no flux at the top, thus we have an expression to evaluate the normal component of the settling velocity:

$$\frac{2}{9}\frac{r^2\Delta}{\nu_C}g\cos\beta\alpha f(\alpha)|_{z=0} \tag{4.68}$$

Notice that the above expression should really be evaluated using the concentration of particles at the bottom ($z = 0$). It is likely that the concentration is higher at the bottom, but due to the limitations of our model, we assume that the concentration is constant in the normal direction of the film.

If we add this new term, the revised equation of the particle evolution becomes

$$\begin{aligned}\frac{\partial(\alpha h)}{\partial t} + \frac{1}{3}\nabla\cdot \quad \{ \quad & \frac{\gamma\alpha h^3}{\mu}\nabla\nabla^2 h - \frac{\alpha h^3}{\mu}g\cos\beta\nabla(\rho h) + \frac{5\alpha h^4}{8\mu}g\cos\beta\nabla\rho + \frac{\alpha\rho h^3}{\mu}g\sin\beta\mathbf{i} \\ & + \frac{2r^2\Delta}{3\nu_C}\alpha f(\alpha)hg\sin\beta\mathbf{i} \ \} + \frac{2}{9}\frac{r_2\Delta}{\nu_C}g\cos\beta\alpha f(\alpha) = 0 \end{aligned} \tag{4.69}$$

We can non-dimensionalize Equation 4.69, and after some simplifications, the final form of the dimensionless particle-evolution equation is

$$\begin{aligned}\frac{\partial(\alpha h)}{\partial t} + \quad \{ \quad & \frac{\alpha}{\mu(\alpha)}h^3 h_{xxx} - D(\beta)[\frac{\alpha}{\mu(\alpha)}h^3(\rho(\alpha)h)_x - \frac{5}{8}\frac{\alpha}{\mu(\alpha)}h^4(\rho(\alpha)_x)] + \frac{\alpha\rho(\alpha)}{\mu(\alpha)}h^3 \\ + \quad & \frac{2}{3}V_s\alpha h f(\alpha) \ \}_x + \frac{2}{3}V_S D(\beta)\frac{x_c^2}{h_c^2}\alpha f(\alpha) = 0 \end{aligned} \tag{4.70}$$

Chapter 5

Results and Discussions

In this chapter, we present the results obtained from numerical simulations based on the model and the full system of equations presented in the previous chapter. We also compare our numerical results with those obtained from experiments. We aim to highlight the agreements and discrepancies between the two through qualitative comparisons.

5.1 Physical and Dimensionless Parameters

The set of values of physical quantities used in the numerical simulations are based on the actual values Benjamin Dupuy used in his experiments. This provides an easy means to compare our simulation results to those obtained from the experiments. We pick silicon oil as our continuous phase, and its surface tension, viscosity and density are assumed to be $\gamma = 21.3 \times 10^{-3}\ kg/s^2$, $\mu_C = 1\ Pa \cdot s$ and $\rho_C = 980\ kg/m^3$ respectively. In the experiments, the particle radius, r, varies from 250 μm to 425 μm. We take the average, and assume that all particles have the same radius, which is taken to be $r = 330\ \mu m$. The particles also have density $\rho_D = 2600\ kg/m^3$. Finally, to scale the thickness of the film, we need to specify the film thickness far behind the front, h_c. The gate opening of the experimental apparatus is normally kept at 1 mm, therefore, we choose $h_c = 10^{-3}\ m$.

The two most important parameters in our problem are the inclination slope β and the initial concentration of the particles in the mixture α. The bulk of our simulations are made with initial particle concentrations in the range of $\alpha = 15\% \sim 45\%$. The inclination angles chosen include $30^o, 42^o, 60^o, 90^o$, where 90^o corresponds to a vertical slope.

The simulations are run with dimensionless quantities. Once the physical quantities and parameter values are set, we are able to calculate the dimensionless parameters using the equations presented in Section 4.8. In particular, we can calculate the values of x_c and t_c from Equations 4.46, 4.47. It is interesting to note that these quantities do not depend on α. Since we expect the particle concentration to play a significant role in the mixture flow, and the non-dimensionalization process does not result in concentration dependent scalings, we expect to see distinct flow behaviors in our simulation results between flows of different initial concentrations. On the other hand, x_c and t_c vary with β. $x_c \sim (\sin\beta)^{-1/3}$, so x_c decreases when β increases. $t_c \sim (\sin\beta)^{-4/3}$, so t_c decreases at a faster rate than x_c when β increases. As a result, the velocity scale $x_c/t_c \sim \sin\beta$. This is consistent with our intuition: the flow is faster when the inclination from the horizontal increases. Because of the scaling, the dimensionless plots correspond to the flow profiles in the dimensional units scaled by x_c/t_c. Table 5.1 lists the values of dimensionless quantities x_c, t_c at different inclination angles.

Angle(degree)	**$x_c(10^{-3}m)$**	**$t_c(sec)$**	**$x_c/t_c(10^{-3}m/sec)$**
30	1.643	1.026	1.601
42	1.491	0.696	2.142
60	1.368	0.493	2.772
90	1.304	0.407	3.201

Table 5.1: *Non-dimensionalization parameters vs. angle of inclination*

The other dimensionless parameters, such as V_s and D_β can also be easily calculated from the expressions derived in the previous chapter. Since D_β measures the relative importance of the normal component of gravity, it vanishes when the flow is

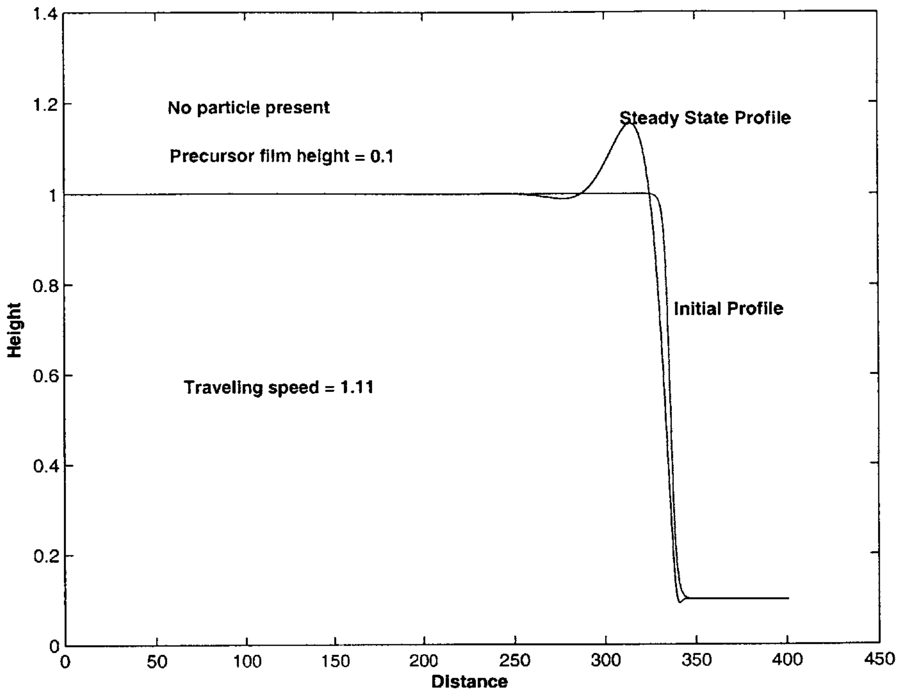

Figure 5-1: *Height Profile for viscous fluid with no particles ($\alpha = 0$), inclination angle $\beta = 42^o, D(\beta) = 0.75$, and precursor film thickness $h_+ = 0.1$ in a moving frame traveling at dimensionless speed* 1.11.

vertical with $\beta = 90^o$.

5.2 Particle Free Viscous Fluid

Since we use a continuum approach in our model, we can study the test case of flow without particles by simply setting the concentration $\alpha = 0$. This corresponds to the thin film flow of a viscous fluid under gravity on an incline plane, and such flow has been extensively studied. Figure 5-1 is a plot of the flow profile when pure silicon oil flows down a plane at 42^o to the horizontal. A precursor film height of 0.1 is used.

With an initial flat profile, the flow quickly develops a bump at the front of the flow, which is approximately 1.2 times the height upstream. Figure 5-1 is set in a moving frame traveling at a dimensionless speed of 1.11. Given the precursor

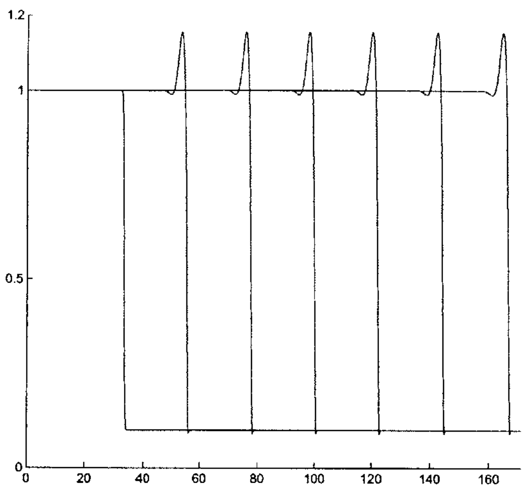

Figure 5-2: *Height Profile for viscous fluid with no particles* ($\alpha = 0$), $\beta = 42^o, D(\beta) = 0.75$ *and precursor film thickness* $h_+ = 0.1$ *in a fix frame. The profiles are plotted at intervals of* $\Delta t = 10$

film height h_+ and the height upstream h_-, the wave traveling speed is precisely determined by $v = h_-^2 + h_- h_+ + h_+^2$ (Refer to Bertozzi and Brenner, Equation 1.8). This speed is verified from the simulation plots, where snapshots of profiles at time intervals in the moving frame, traveling at speed v, overlap. Since there is no more change in the flow profile, the flow has reached its steady state, and it travels at a fixed wave speed. The same flow profile in a fix frame is shown in Figure 5-2. The fluid profiles are plotted at intervals of $\Delta t = 10$.

The simulation results obtained from zero particle concentration agree with the results obtained previously for a viscous fluid. A bump is formed at the contact line which has been proved to be responsible for the instability.

5.3 Effect of Inclination Angle and Particle Concentration on the Flow Profile

Numerous simulations have been performed with varying inclination angles and varying initial particle concentrations. In each case, we plot the height profile and concentration profile at selected time points as the mixture flows down the inclined plane. It requires considerable effort to derive the wave speed at which the mixture is flowing down, as it involves applying the system of conservation laws on our two-equation system. We will discuss this in greater detail in the next chapter. Therefore, profiles are all shown in a fixed frame in this chapter. Profiles at initial concentrations of 15%, 30% and 45%, and inclination angles of 30^o, 42^o, 60^o and 90^o are selected for comparisons.

Figure 5-3 shows the height profiles at intervals of $\Delta t = 40$ in successive times. The horizontal axis of each plot is the dimensionless distance, and the vertical axis is the dimensionless height. All of these plots are simulated with a precursor film height of 0.1. For comparison purposes, all plots have a distance range of $0 - 250$ on the x-axis and a height range of $0 - 2$ on the y-axis. The first profile on the left most of each plot corresponds to the initial height profile, and they are set the same for each case. The total simulated time for all plots are $t = 280$ in dimensionless time.

It is easy to see that the flow profiles at different initial concentrations differ significantly. For flows with same inclination angle, mixtures with higher concentration flow slower than those with lower concentration. A mixture with high particle concentration behaves more like a solid with high viscosity and density in our continuum model. In fact, the viscosity tends to infinity as the concentration approaches the maximum packing number, and the mixture becomes increasingly more resistant to flow. Another interesting feature is that the peak height of the profiles at the same dimensionless time for different initial concentrations show that the bump is taller when the concentration is higher. This seems to suggest that the particle concentration plays an important role in forming the bump: more particles result in higher bumps at the contact line. The profiles with 15% particle concentration reveal that after the flow has developed for some time, the height profile shows an intermediate flat plateau behind the peak of the bump. The plateau gradually grow in width as time progresses. On top of the plateau, we observe the usual bump that resembles the bump in the pure viscous fluid case. The bump in the viscous fluid case is caused by the surface tension as discussed in chapter 1. These observations lead us to postulate that the lower plateau is caused by the presence of particles and the upper small bump is caused by the surface tension. Once again, it is impossible to check the validity of this postualte from just the plots alone. We will discuss this point again when we analyze our system of equations in the next chapter. The plots at 30% initial concentration begin to show the plateau structure too, although it starts to develop at a later time and at a higher height. We do not observe the plateau structure in the case of 45% concentration, at least up to the simulation time of $t = 280$. Moreover, unlike the pure viscous fluid case, the flow profiles are still evolving, and we have not observed a steady state profile. In the case of 15% and 30% concentrations, the peak height of the bump has reached a steady value, yet the plateau is growing in width. In the case of 45% concentrations, the height of the bump is still growing.

If we look down the column and compare the flow profiles with same initial concentration but different inclination angles, we see that the bulk structure is similar for each plot. In the dimensionless frame, a mixture with a fixed initial concentration flows down at the same dimensionless speed on inclined planes of different angles. This does not contradict our intuition that flow is faster at steeper slopes, since the dimensional speed is obtained by multiplying the dimensionless speed with the velocity scale x_c/t_c, which increases with increasing angle. The plots also show that flows of same initial concentration have a plateau developing at the same height and growing at the same rate. We do observe slight differences in the upper bump areas for flows at different angles. This upper bump appears to be taller for higher angles. On the other hand, this upper bump seems to be the same for flows of different initial concentrations but same slope angle, reinforcing our believe that this upper bump is formed by surface tension rather than the particles. The inclination angle β affects the terms with $D(\beta)$ coefficient in our system of equations. $D(\beta) = 0$ when $\beta = 90^o$, and it increases to $D(\beta) > 1$ at $\beta = 30^o$. Even though there is a significant change in the magnitude of the terms with $D(\beta)$ coefficient from $\beta = 90^o$ to $\beta = 30^o$, the dimensionless bulk flow speeds and flow profiles are almost identical, indicating that these terms are relatively unimportant to the overall transport of the mixture.

The height profiles provide us with many interesting and important observations that lead us to several questions. First, we want to know whether there exists a steady state for flows with particles present. Second, mixtures of the same initial concentration seems to flow at the same dimensionless speed, but we have yet to find what determines this speed. Third, we need to find out how much of the bump results from particle effects and how much of it is caused by the surface tension effect. Lastly, we want to know what determines the intermediate height that gives the plateau, and whether such an intermediate height also exists in flows of high initial concentrations.

Figure 5-4 shows the evolution of flow concentrations as the mixture moves down the plane. The x-axis is the dimensionless distance, which has a range of $0 - 250$ for all plots. The y-axis is the concentration. Although plots of different initial concentrations have different y-axis ranges, the y-axis for all cases is set to have a span of 20%. The concentration profiles are plotted at intervals corresponding to the height profiles intervals. The concentration plots show that a constant concentration profile changes as the profile evolves, and the region where we see a bump in the height profile has higher concentration. So, as the mixture flows down, the heavier particles flow down faster and they accumulate at the flow front, causing the concentration and the resulting height at the contact line to be higher. Previously in the height profile plots, we observed a plateau structure for initial concentrations of 15% and 30%. In the concentration plots, we observe that the plateau region has a constant concentration larger than the initial concentration. On top of this flat concentration, a slightly higher concentration bump is observed, which corresponds to the upper bump in the height profile. Comparing concentration plots of different initial concentrations, we notice that the increase in concentration from the initial level to the maximum value at the bump is greater for lower initial concentration. This is probably due to the fact that the maximum concentration that can be reached is the maximum packing fraction, and the concentration becomes progressively harder to increase as it approaches this limit. Another interesting feature of the plot is the presence of a small dip in concentration on the immediate left of the major bump. This feature is more pronounced in the early stages of the flow, and in the flow with higher initial concentration. The origin of this feature is not known.

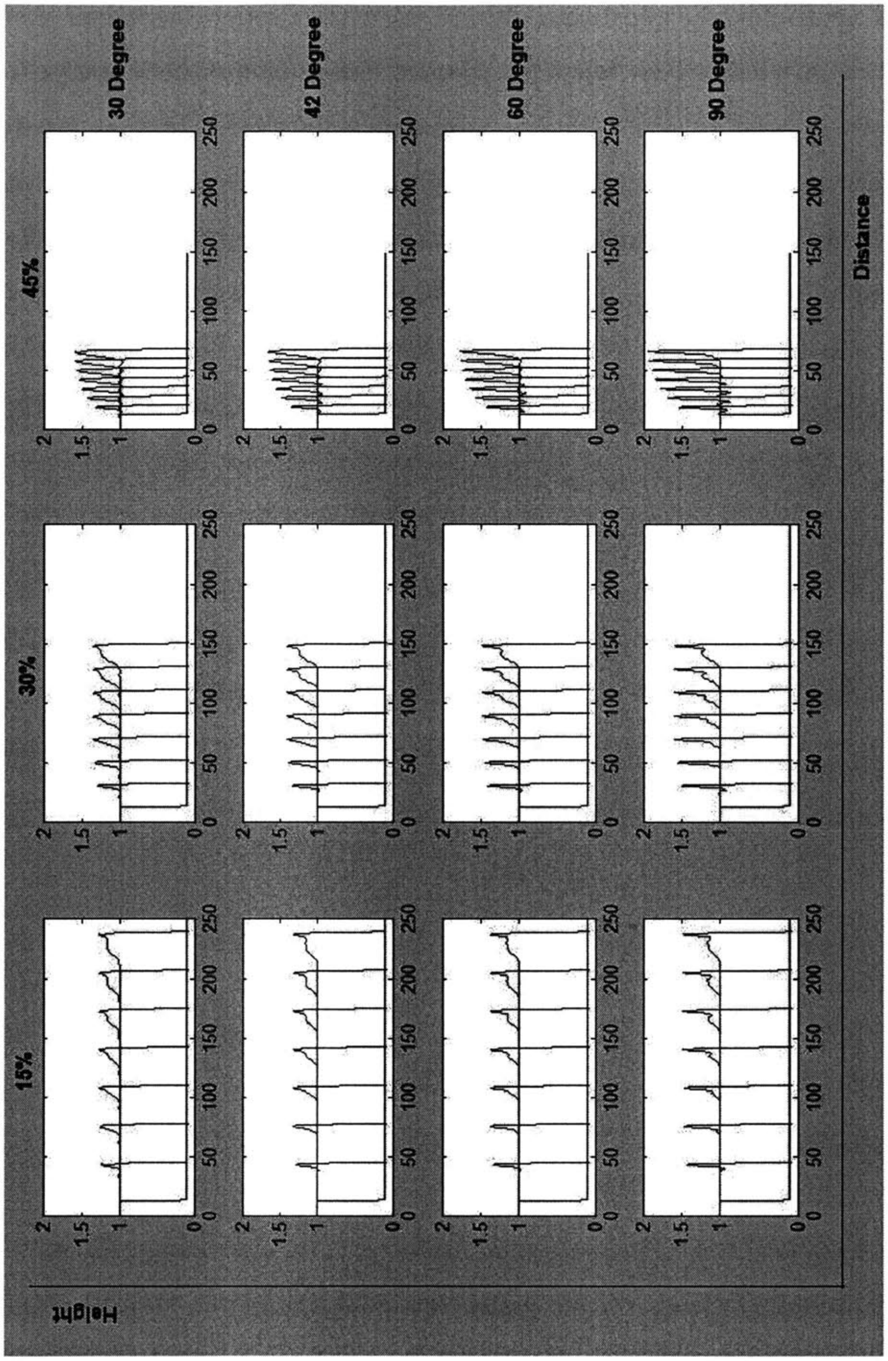

Figure 5-3: *Height profiles simulated on mixture flows with initial particle concentrations of* 15%, 30% *and* 45% *and inclination angles of* 30^o, 42^o, 60^o *and* 90^o. *For each plot, the profiles are plotted at intervals of* $\Delta t = 40$. *Precursor film thickness of* 0.1 *is used in all simulations.*

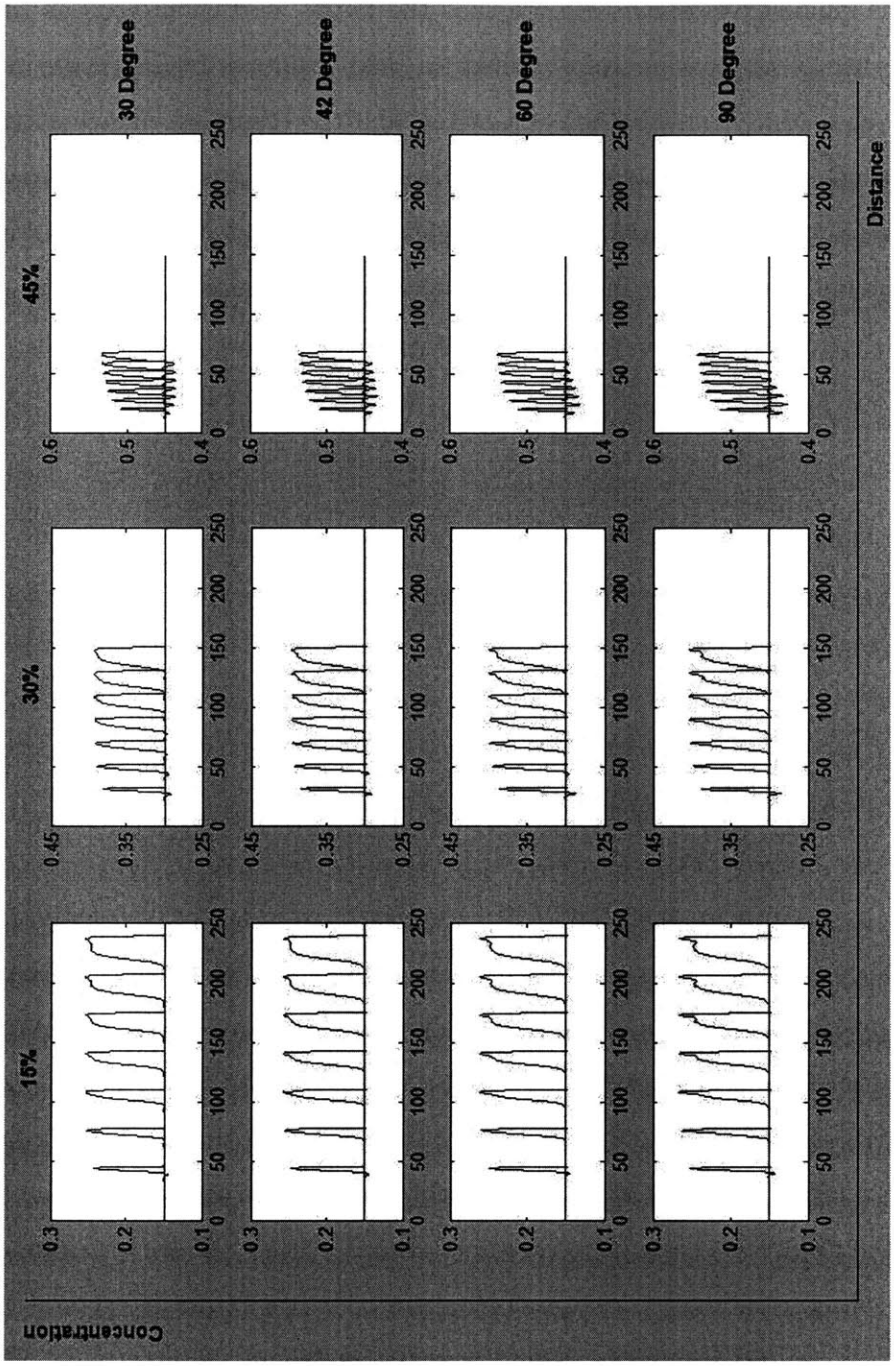

Figure 5-4: *Concentration profiles simulated on mixture flows with initial particle concentrations of* 15%, 30% *and* 45% *and inclination angles of* 30^o, 42^o, 60^o *and* 90^o. *For each plot, the profiles are plotted at intervals of* $\Delta t = 40$. *Precursor film thickness is* 0.1 *in all simulations.*

In the simulations above, we see that the bump width increases as the mixture flows down the plane. Therefore, there are two fronts traveling down at different speeds: the leading front at the contact line and the trailing front which travels at a slower speed. Table 5.2 lists the measured speeds at the two fronts for flows of 15%, 30% or 45% initial concentrations. Note that the speeds for flows of the same initial concentration but different inclination angles have the same dimensionless speeds.

	15%	**30%**	**45%**
Leading Front	0.811	0.488	0.196
Trailing Front	0.744	0.440	0.179

Table 5.2: *Frontal speeds for flows with initial concentrations of* 15%, 30% *and* 45% *measured from simulations.*

5.4 Effect of Precursor Film Thickness

We have used a precursor film of 0.1 in the results presented in the previous section. In the case of pure viscous fluid, it has been found that the choice of the precursor film has a substantial influence on the height of the bump developed. We therefore run a series of simulations with different precursor film thicknesses, while keeping all other parameters the same. In a typical experiment, the height of the film upstream near the gate is approximately 1 mm, and the thin layer of fluid mixture left on the plate after applying the squeegee is approximately $10 - 20$ μm. Therefore, based on our scaling, a dimensionless precursor film of $0.01 - 0.02$ corresponds to the real experimental values. Figure 5-5 shows a snapshot of the height profiles of a mixture with 30% initial concentration flowing down a 42^o incline plane. Precursor heights of 0.01, 0.02, 0.05 and 0.1 are used in the simulations. All profiles are taken at the same instant after the mixture has flowed and evolved for some time. Figure 5-6 shows the corresponding concentration profiles for the same set of simulations.

The plots show clearly that the precursor thickness has a significant influence

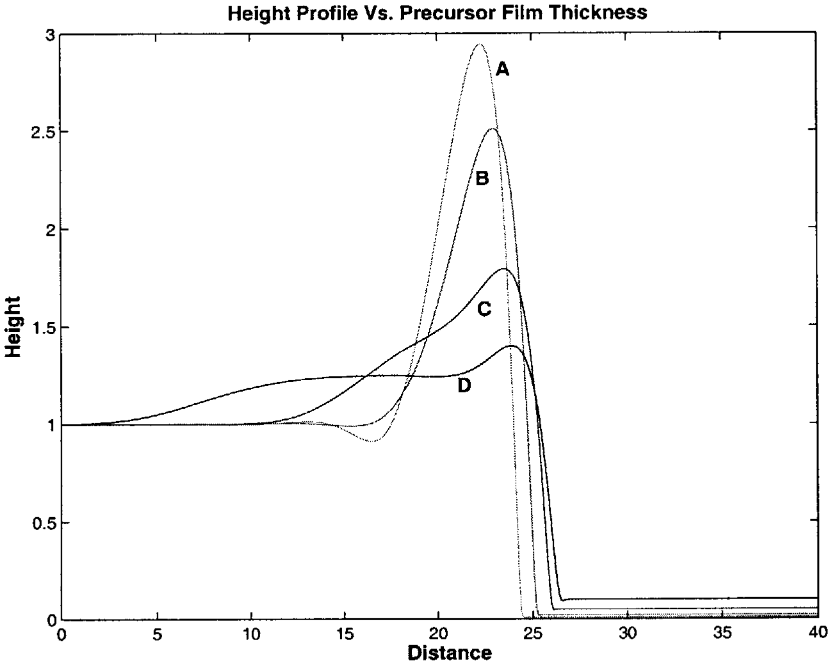

Figure 5-5: *Height profiles at* $t = 280$ *with different precursor film thickness: (A) 0.01 (B) 0.02 (C) 0.05 (D) 0.1*

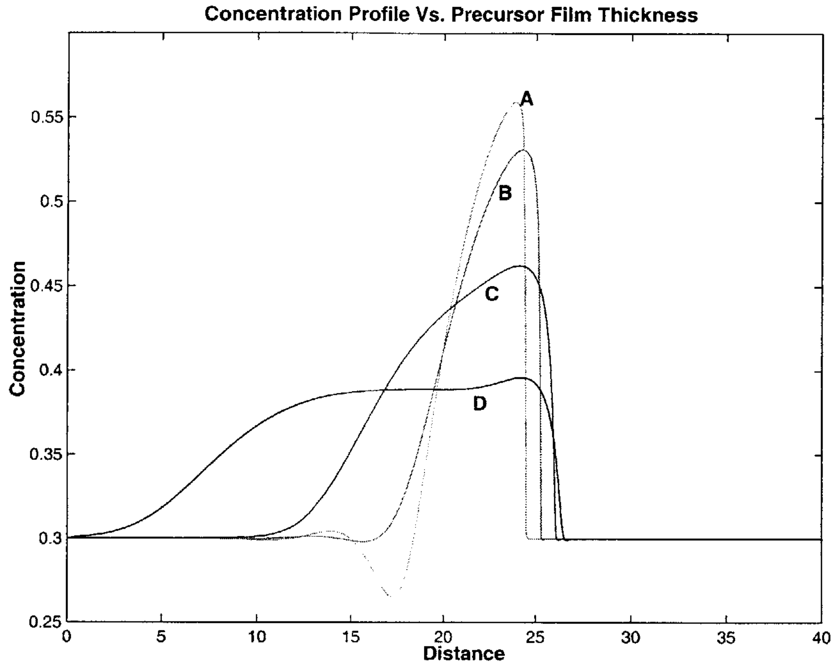

Figure 5-6: *Concentration profiles at* $t = 280$ *with different precursor film thickness: (A) 0.01 (B) 0.02 (C) 0.05 (D) 0.1*

on the maximum height and concentration, as well as the bulk structure of the flow. Similar to the pure viscous fluid case, the height profiles show that a smaller precursor film leads to a higher bump. The peak height of the bump with a precursor film thickness of 0.1 is approximately 1.4. On the other hand, the peak height of the bump at the same instant with a precursor of 0.01 reaches 2.9. The height profile with a precursor film thickness of 0.1 has develped a plateau approximately at height 1.25. The profile with 0.02 precursor thickness has not yet developed a plateau, but we can clearly see a kink in the trailing edge at around 1.5. If we let the simulation run longer, a plateau starts to form at this height. In the case of even thinner precursor films, the bulk structure resembles those observed in the simulations of higher initial concentrations previously presented, with no plateau and secondary bump visible. Therefore, the choice of precursor film affects both the peak height of the bump as well as the height at which the plateau forms if one exists.

The precursor film thickness can also affect the mixture traveling speed. The profiles shown are taken at the same instant and all have been shifted by the same amount to the left. If we compare the leading edge on the right of each profile, we see that the leading front of the profiles with thicker precursor film are to the right of those with thinner precursor film, indicating that the leading front speed increases with precursor film thickness. On the other hand, the trailing front of the profiles with thicker precursor film are behind those with thinner precursor film, suggesting that the trailing front speed decreases when precursor film thickness increases. The fact that the bump width grows faster when thicker precursor film is used is a combination of the above two effects.

The corresponding concentration profiles show similar structures. Thicker precursor film gives rise to a more rounded and wider bump, whereas thinner precursor film gives rise to a sharper and narrower bump.

5.5 Dimensional Plots

In this section, we will show a couple of plots in dimensional units and compare them to the real flow from experiments. As we have pointed out, our current model best describes flow regimes where a ridge is formed at the contact line. In such regimes, the slope is steep and the particle concentration is high. Nearly all particles travel down with the mixture and accumulate at the front. As time progresses, more and more particles accumulate to create a very pronounced bump that Benjamin Dupuy described as a "ridge" in his experiments. Benjamin showed the height of the bump can grow by as much as a factor of three compared to the bump $0.1m$ upstream.

Mixtures of 45% initial concentration flowing down a 42^o slope falls into the "ridge formation" regime based on Benjamin's phase diagram. We run simulations on this set of parameters and plot the resulting height and concentration profiles. The plots are shown in Figure 5-7. The height profiles from numerical simulations behave very much like what Benjamin observed in his experiment. At the end of simulation at dimensional time $t = 280s$, the tip of the bump is 5 times as tall as the film thickness far upstream. Compared to the peak height of 1.2 in the pure viscous case, this growth of bump height is astonishing, and must be attributed to the particles. Comparing the peak height at $t = 280s$ to that at $0.1m$ upstream ($t = 70s$), the height has more than doubled. So, our numerical results are in line with experimental results. The concentration plot shows that the maximum concentration at the bump increases to more than 60%. This concentration is very close to the maximum packing fraction. This explains the observation in Benjamin's experiments that when a ridge is formed, the particle concentration at the contact line is so high that the mixture behaves almost like a solid. In the concentration plot, we observe a dip in concentration just before the bump. It is very difficult to measure particle concentration during the experiment, and currently we do not have experimental data to verify this interesting feature revealed by the simulation.

Figure 5-8 shows the same height profile, but with an aspect ratio of 1 to 1. The height profiles shown in this aspect ratio has the same scale as the actual experimental profiles.

5.6 Preliminary Results on Model with Normal Gravity Component

In Chapter 4, we briefly discussed an approach for including the normal component of gravity into our system of equations. The normal component of gravity takes into account motion of the particles in the direction normal to the mixture flow direction. Therefore, the inclusion of this term will result in loss of particles during the flow down the inclined plane as some of the particles leave the mixture and settle down onto the bed. We also mention the limitations of our model as well as the difficulties in estimating this normal flux. We present some results obtained by simulating the system of Equations 4.48, 4.70. These results are only preliminary, and they only serve to provide us some insights into this aspect of the problem.

Figure 5-9 shows the simulation results on a flow with 30% initial concentration

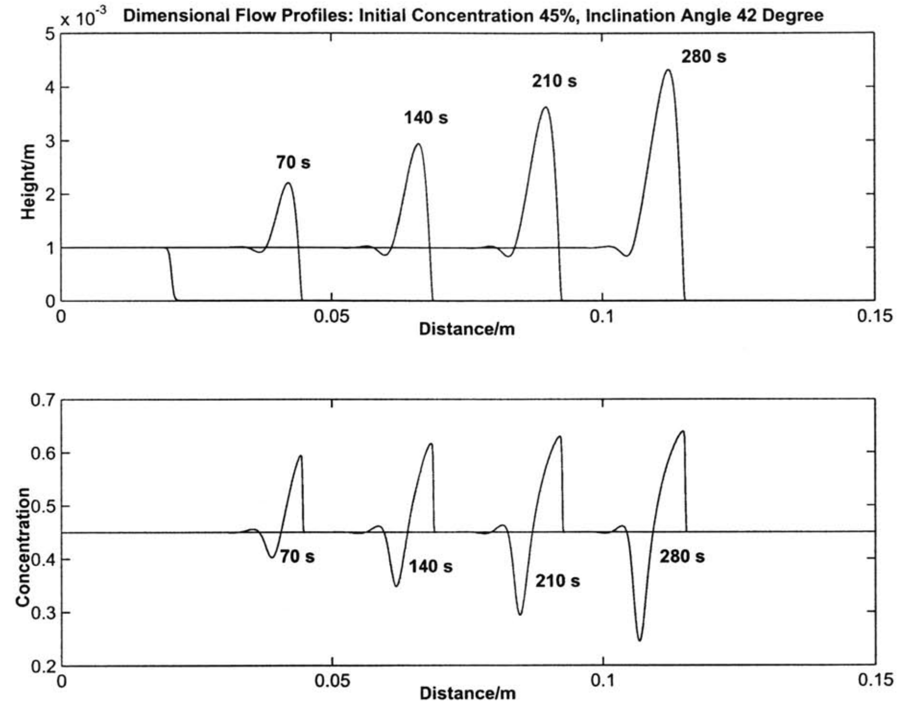

Figure 5-7: *Dimensional plots from simulations on flow of* 45% *initial concentration and* 42° *slope. Top: height profiles; Bottom: corresponding concentration profiles. All quantities shown are dimensional.*

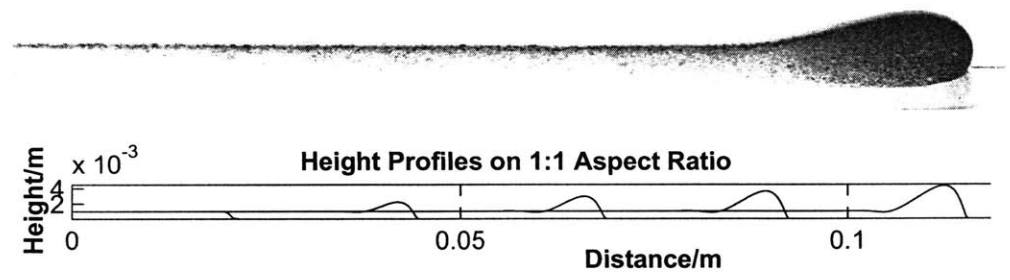

Figure 5-8: ***Top:*** *Picture of a ridge with* 250 ~ 425μm *beads illuminated by a laser and taken by a digital camera during an experiment conducted by Benjamin.* ***Bottom:*** *Simulated Height profile on a* 45% *particle concentration flow down a* 42° *slope with 1 to 1 aspect ratio.*

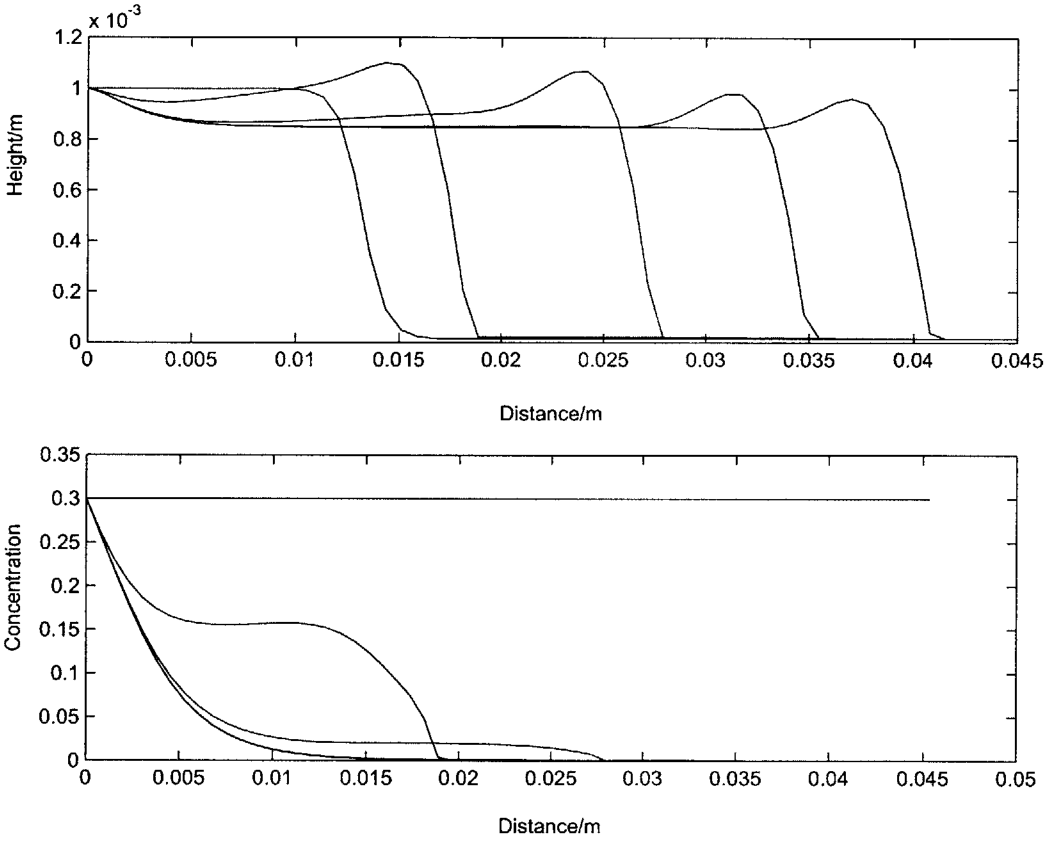

Figure 5-9: *Simulated plots with normal flux term included. The mixture's initial concentration is* 30%, *and the inclination angle is* 45^o. *Top: Height profiles at intervals of 10s. Bottom: Concentration profiles at same time.*

and inclination angle of 45^o. The upper plot shows the height profiles at intervals of 10 seconds. The lower plot is the corresponding concentration plot. The graphs are shown in dimensional units.

We observe from the concentration plot that the concentration of the particles in the mixture drops down to zero within a short period of time. This means the particles in the mixture quickly settle out, leaving behind a clear viscous fluid. We still observe a bump in the height plot, caused by surface tension alone, as the size of the bump is much smaller in this case and there are no particles left in the flow. In Section 3.2, we have discussed the phase diagram (See Figure 3-3) that Benjamin Dupuy ([16]) mapped out according to his experimental data and observations. Base on the phase diagram, the flow of a mixture with 30% initial concentration on a 45 degree slope falls into the suspension regime. In this regime, we expect to see part of the particles present settling out, and the remaining particles traveling downstream with the mixture. The magnitude of the normal flux in our system of equations is so large that it pulls out all particles. We have previously mensioned that our approach of using the average concentration instead of the concentration at the base will tend to result in a larger normal flux. Another subtle effect that we have ignored is the slowing down of settling velocity near the base due to wall effect. Our simulation demonstrates that the current normal flux term is indeed too large.

In order to have a better estimate, we have to modify the normal flux expression by adding more terms to account for the effects near the wall. Unfortunately, the problem is rather complex. Due to time constraints, we have not pursued further investigations into this particular problem. Figure 5-10 shows simulation plots on the same flow problem, but with 1/10 of the original flux term. There is no particular reason for picking the factor 1/10, but the plots do show us changes in the flow behaviors when we have a smaller normal settling component.

With a reduced normal settling velocity, we see that the concentration still decreases as particles settle out, but the rate at which the concentration decreases is much smaller. In fact, there are still particles present in the mixture at the end of the simulation time. This resembles the suspension regime. This simple and crude

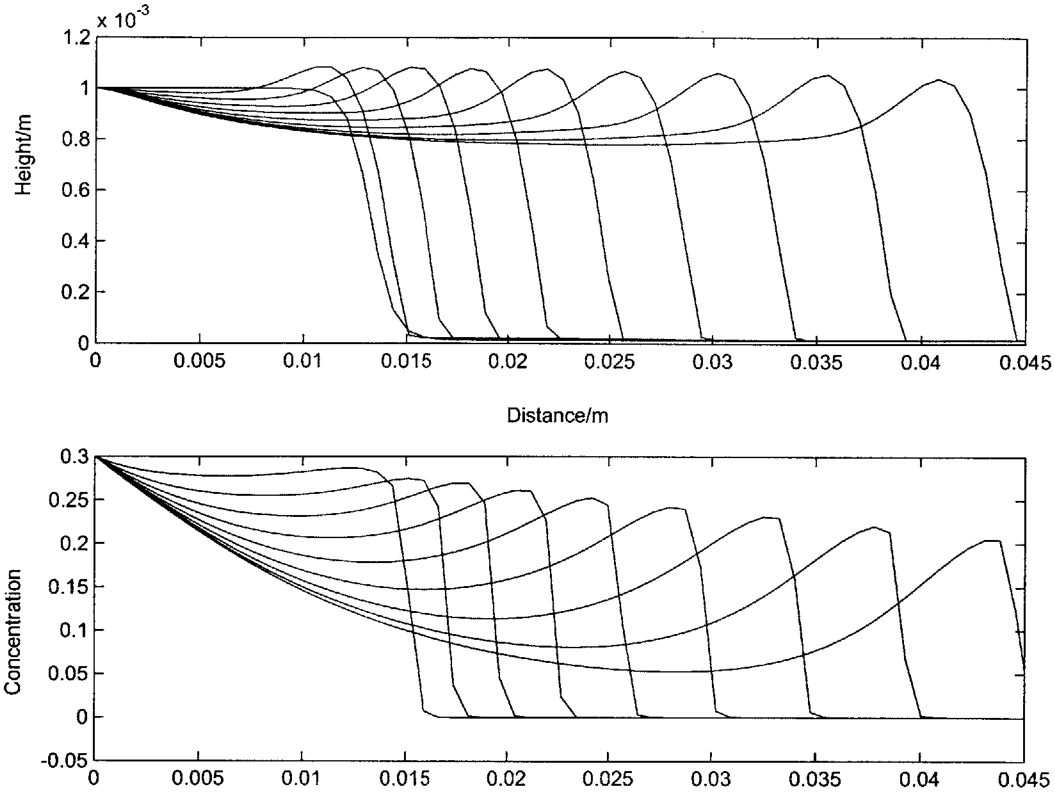

Figure 5-10: *Simulation on the same problem with* $1/10$ *of the normal flux. The mixture's initial concentration is* 30%, *and the inclination angle is* 45^o. *Top: Height profiles at intervals of 10s. Bottom: Concentration profiles at same time.*

modification tells us that by accurately balancing the relative magnitude of the two competing events: transportation of particles downstream and settlement of particles onto the flow bed, it is possible to mimic behaviors observed in the real flow.

Chapter 6

Reduced System

In previous chapters, we presented a model for particle laden flow down an inclined plane. We also presented and discussed observations and interesting features from the simulation results. We raised several key questions regarding system behaviors, and we hope to answer these questions by analyzing our system of equations in this chapter.

6.1 Equations and Comparison

In fluid experiments involving flow down an inclined plane, the large scale dynamics is often described by shock theory in which only the lowest order terms (the convective terms) in the equation yield information about the front speed, shape of the fluid etc. One classical example is the work by Huppert [33], in which he drops the higher order terms and shows that fluid flow on an incline is well described by a rarefaction wave solution of a scalar conservation law.

More recently, temperature gradient driven flow balanced by gravity has been shown to be described by a scalar conservation law with a nonconvex flux [2]. In that problem, the non-convexity of the flux opens up the possibility of undercompressive shocks. The transition from compressive to undercompressive waves has been documented in recent experiments and explains a variety of phenomena seen in experiments [2, 36]. In these experiments, the effect of surface tension in the shock layer is responsible for the emergence of these 'non-classical' shock patterns.

For our particle laden flow problem, we discover that the underlying convective dynamics is described by a system of two conservation laws:

$$\begin{aligned} \frac{\partial(\rho(\alpha)h)}{\partial t} + \{\frac{\rho(\alpha)^2}{\mu(\alpha)}h^3\}_x &= 0 \qquad (6.1) \\ \frac{\partial(\alpha h)}{\partial t} + \{\frac{\alpha\rho(\alpha)}{\mu(\alpha)}h^3 + \frac{2}{3}V_s\alpha h f(\alpha)\}_x &= 0 \qquad (6.2) \end{aligned}$$

We will, hereafter, call the above system of equations the reduced system. The reduced system retains the low order transport terms in the full system of equations, and drops rest of the higher order terms. We notice that the $D(\beta)$ terms are no longer in the reduced system, and therefore flows with same initial particle concentration will yield the same profiles in dimensionless units regardless of the inclination angle. Figure 6-1 shows the height profiles and concentration profiles of flows with initial concentration of 15%, 30% or 45%.

The plots from the reduced system exhibit similar behaviors compared to those obtained from the full system. Flows with lower initial concentration travel faster than those with higher concentration. In the case of 15% and 30% initial concentrations, the profiles have developed into a flat top structure, whereas the 45% initial concentration flow has not. Similar to the full system, the concentration plots from the reduced system show that there are more particles in the bump.

In the case of a viscous fluid, previous studies have shown that the bump is caused by the presence of the surface tension terms. Without the surface tension term, simulations result in a classical shock wave structure with no bump at all. Our reduced system does not have surface tension in it, yet we still observe a bump forming at the front. Therefore, the presence of particles are definitely responsible for the formation of the bump.

We would like to determine whether the large scale quantities of interest, such as front speed and bump height, are well described by the reduced set of equations. To do so, we plot the height and concentration profiles from both the reduced and the full systems on top of each other. Figure 6-2 shows the comparison of numerical simulation results of the full system with the reduced system on a flow with initial concentration

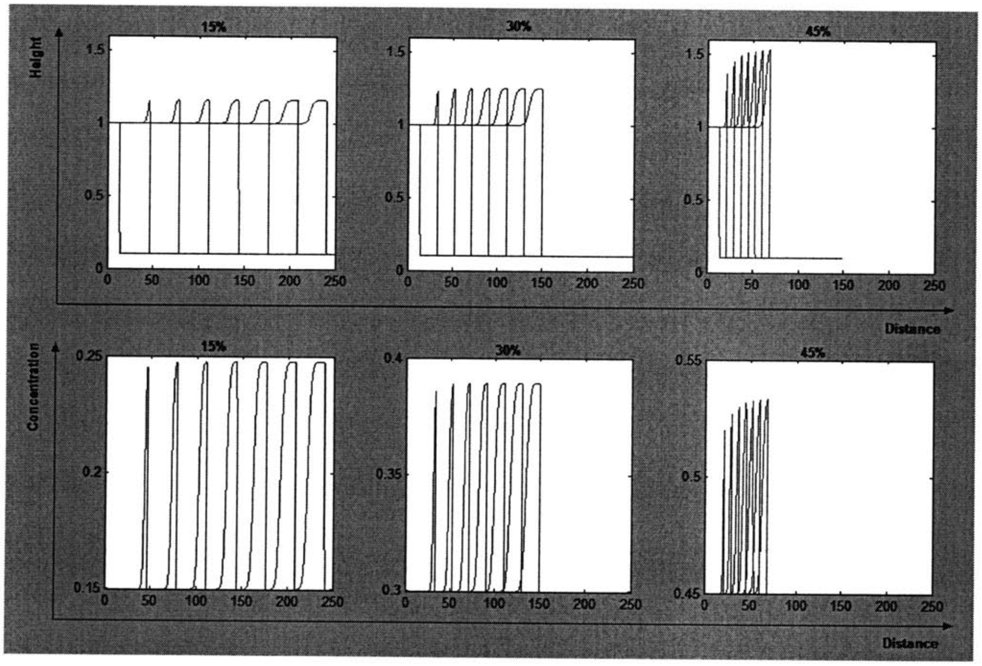

Figure 6-1: *Flow profiles from simulations on the reduced system. Initial concentrations are* 15%, 30% *or* 45%. *Profiles are plotted at dimensionless time* $\Delta t = 40$. *Top row: height against distance. Bottom row: concentration against distance.*

of 30% and inclination angle of 42^o. These plots clearly show that the front speed of the full system agrees very well with the front speed of the reduced system. Moreover, the bulk structure of the two systems are also very close. Previously, we noted that the height profiles of the full system for this mixture flow has an upper minor bump on top of an intermediate plateau. The comparison plots indicate that the plateau from the full system coincides with the flat top from the reduced system. Therefore, the formation of this plateau must be attributed to the low order transport terms. On the other hand, the reduced system does not have the small hump on top of the plateau, suggesting that this hump is resulted from the presence of surface tension as in the case of viscous fluid.

Figure 6-3 gives another set of comparison plots on a mixture flow with 45% initial concentration. Even though the flow behavior in this plot is quite different from the 30% concentration case, we still observe close agreement between the reduced system and the full system.

6.2 System of Conservation Laws

We note that the reduced system has the form

$$\frac{\partial u}{\partial t} + [F(u,v)]_x = 0 \tag{6.3}$$

$$\frac{\partial v}{\partial t} + [G(u,v)]_x = 0 \tag{6.4}$$

where $u = \rho(\alpha)h$ and $v = \alpha h$.

We are interested in the solution of the above system with an initial condition of uniform thickness and particle concentration upstream, and the same uniform concentration but small thickness downstream in the precursor layer. Therefore, at time zero, we have

$$h = 1, \quad x < 0, \quad h = b, \quad x > 0$$

$$\alpha = \alpha_0$$

where b is the precursor thickness and α_0 is the initially uniform particle concentration. Here, we set $x = 0$ as the position of the gate.

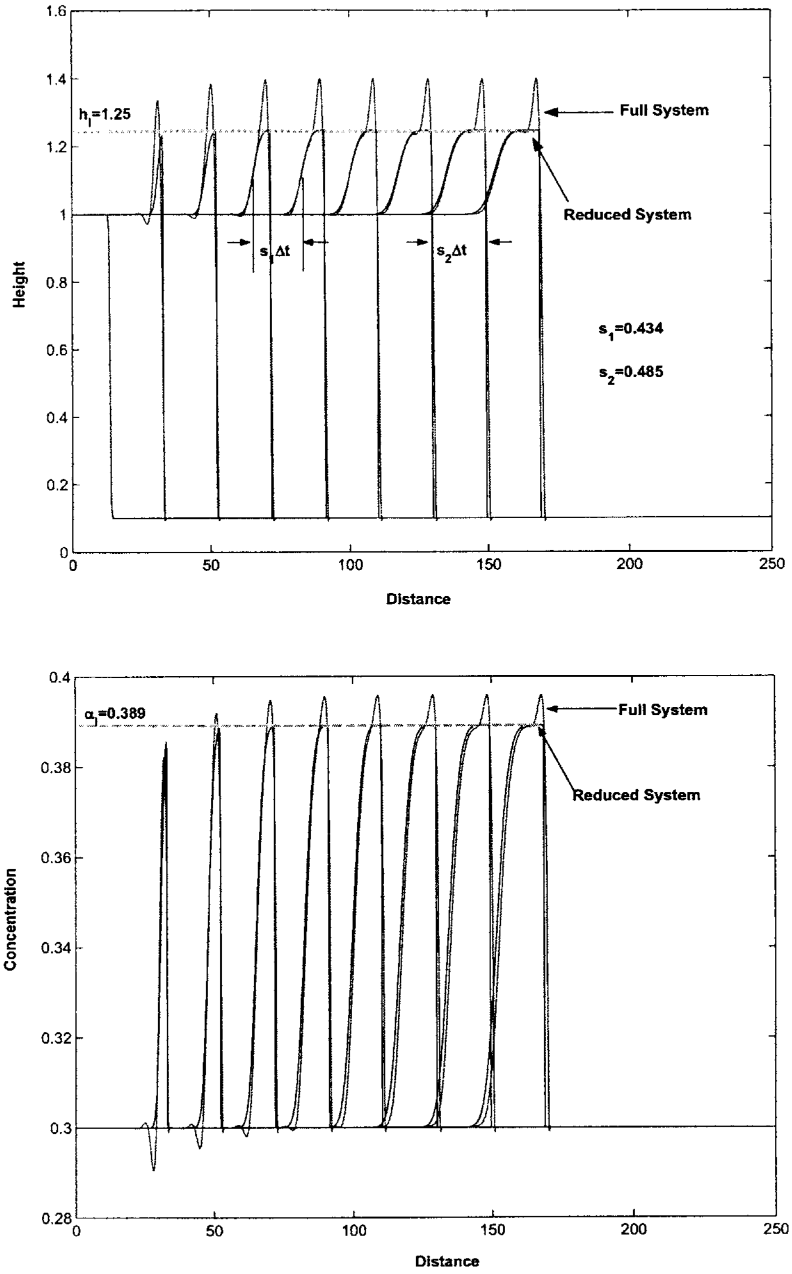

Figure 6-2: *Comparison of the reduced system and the full system for flow with initial concentration* 30% *down a* 42° *slope. Top: height profiles; Bottom: concentration profiles. Profiles are shown at intervals of* $\Delta t = 40$.

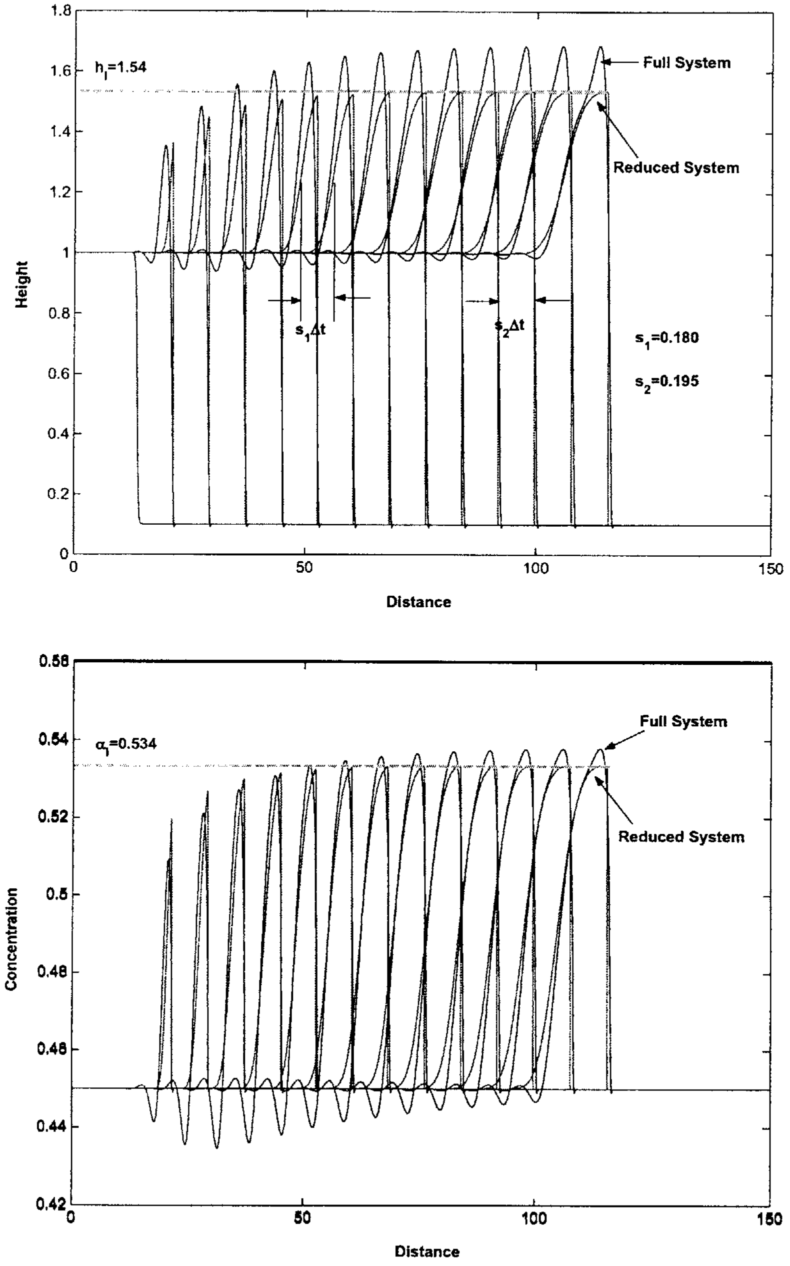

Figure 6-3: *Comparison of the reduced system and the full system for flow with initial concentration* 45% *down a* 42^o *slope. Top: height profiles; Bottom: concentration profiles. Profiles are shown at intervals of* $\Delta t = 40$.

The above initial concentration gives us a Riemann problem. That is, both of the system variables u and v have a jump at the origin at time zero. The variable u jumps from

$$\rho(\alpha_0) \equiv u_l \text{ to } \rho(\alpha_0)b \equiv u_r$$

while the variable v jumps from

$$\alpha_0 \equiv v_l \text{ to } \alpha_0 b \equiv v_r$$

The solution of this problem is in the theory of shock-waves. We expect to see shock-shock pair with an intermediate state u_i, v_i separating the two. The values of u_i and v_i in the intermediate state describe the density of particles and the fluid thickness in the bump region of the flow. We can derive an implicit formula for the intermediate values u_i and v_i by solving a couple eigenvalue and ODE problem. These values will only depend on the left and right states (u_l, v_l), (u_r, v_r), and the particular functional form of F and G. Thus, we will be able to obtain a prediction for the bump height and front speed depending only on the initial particle concentration and initial thickness of the film. In the next 2 sections, we will first outline the general approach in solving these type of problems, and then apply it to solve for our particular system of conservation laws.

6.3 Theory of Shock Waves for 2-Systems

We consider the 2X2 system of conservation laws: 6.3 and 6.4. Let us assume that the system is hyperbolic, that is the Jacobian matrix

$$J(u,v) = \begin{pmatrix} F_u & F_v \\ G_u & G_v \end{pmatrix}$$

has two real distinct eigenvalues $\lambda_1(u,v)$ and $\lambda_2(u,v)$ labeled in increasing order. Since J depends on (u,v), so do the eigenvalues and eigenvectors r_1 and r_2. We require that the eigenvalue problem is genuinely nonlinear which means that

$$r_i \cdot \nabla \lambda_i \neq 0 \tag{6.5}$$

where the gradient is with respect to the variables u and v. This condition generalizes the classical scalar law condition that the shock speed depends non-linearly on the solution u, that is $ds/du \neq 0$. The classical shock theory says that if the states (u_l, v_l) and (u_r, v_r) are sufficiently close, then the Riemann problem has a solution. The solution consists of 3 constant states (u_l, v_l), (u_i, v_i), and (u_r, v_r) each separated by either a centered rarefaction wave or a shock wave.

We now need to compute the shock connection problem. The rarefaction wave and the shock wave behave differently, and mathematically the methodology for solving the two are quite different. It would save a great deal of work in terms of computation if we could determine the type of the wave occurring in our system. Plots from the simulation show that the leading front wave which connects the intermediate state (u_i, v_i) and the right state (u_r, v_r) resembles a typical shock wave with sharp edge and a clear jump between states. On the other hand, the trailing wave which connects the left state (u_l, v_l) and the intermediate state (u_i, v_i) is rather ambiguous. It looks too smooth to be a shock wave, but it also does not open up like a typical rarefaction wave. When we numerically solve the problem, we inevitably introduce diffusion into the problem. To check the effect of added diffusion on the results, we can reduce the grid size while keeping the CFL condition satisfied. Figure 6-4 is a height profile plot of a mixture flow with 30% initial concentration down an incline of 42^o to the horizontal. This plot is obtained from simulation with a grid size of 0.025, which is 4 times smaller than the simulation results previously shown in Figure 6-1. Reducing the grid size reduces the amount of added diffusion in the numerics. Although the trailing edge in Figure 6-4 is still rather smooth, it is considerably sharper than the simulation on the same flow with coarser grid points. This fact suggests that the smoothness of the trailing front is likely induced by the numerics, and we would see a sharp shock wave at the trailing edge as well if we make the grid size small enough.

6.3.1 Shocks at Both Fronts

If we assume that we have shock waves at both fronts, our task is to find for what values we will have a 1-shock that connects to u_l, v_l and a 2-shock that connects to

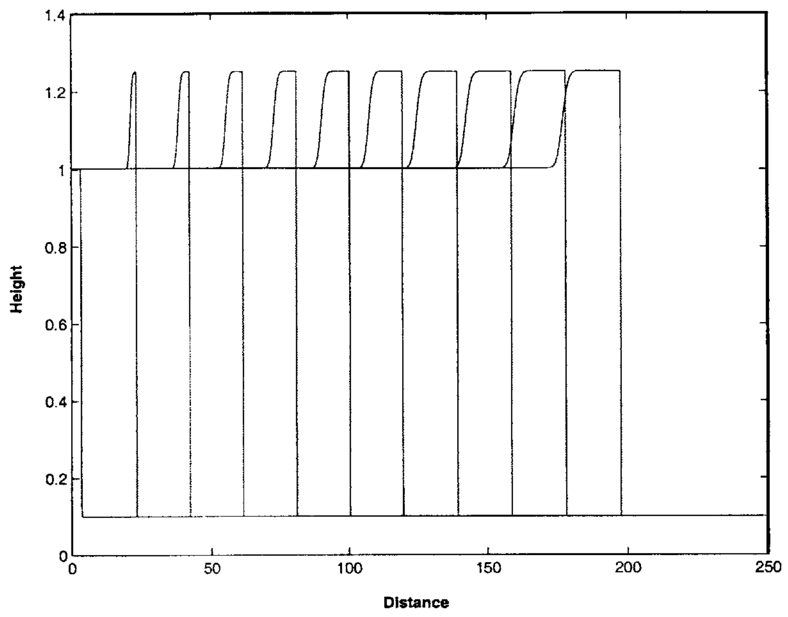

Figure 6-4: *Height profiles from simulation with more refined grid points:* $dx = 0.025$. *The mixture has* 30% *initial concentration and the inclination angle is* 42^o.

u_r, v_r. Since we have two variables u, v, generically there is a one parameter family in each case. Shocks are jump discontinuities and when the equation representing a shock is integrated against a test function, the weak form of the equation yields two Rankine-Hugoniot conditions for the shock speed both of which have to be satisfied.

For the 1-shock, they are

$$s_1 = \frac{F(u_i, v_i) - F(u_l, v_l)}{u_i - u_l} \tag{6.6}$$

$$s_1 = \frac{G(u_i, v_i) - G(u_l, v_l)}{v_i - v_l} \tag{6.7}$$

and for the 2-shock they are

$$s_2 = \frac{F(u_i, v_i) - F(u_r, v_r)}{u_i - u_r} \tag{6.8}$$

$$s_2 = \frac{G(u_i, v_i) - G(u_r, v_r)}{v_i - v_r} \tag{6.9}$$

In the case where the state (u_i, v_i) connects to the left and right states by shocks on either side, then the equations 6.6-6.7 and 6.8- 6.9 provide four equations in four unknowns (u_i, v_i, s_1, s_2). Generically, there will be a locally unique solution.

However, these equations are also accompanied by entropy conditions which restrict whether a 1-shock or 2-shock is an admissible connection. For the 1-shock connecting (u_l, v_l) to (u_i, v_i), we must have $\lambda_1(u_l, v_l) > s_1 > \lambda_1(u_i, v_i)$ and $\lambda_2(u_l, v_l) > s_1$ and $\lambda_2(u_i, v_i) > s_1$. That is the characteristics associated with λ_1 impinge on the shock and the characteristics associated with λ_2 pass through the shock from the left. For the 2-shock connecting (u_i, v_i) to (u_r, v_r), we must have $\lambda_2(u_i, v_i) > s_2 > \lambda_2(u_r, v_r)$ and $\lambda_1(u_i, v_i) < s_2$, $\lambda_1(u_r, v_r) < s_2$. That is the characteristics associated with λ_2 impinge on the shock and the characteristics associated with λ_1 pass through the shock from the right. In the event that the four equations have a solution, but do not satisfy the entropy condition, then the correct solution will involve a rarefaction fan. See appendix for rarefaction wave solution.

6.4 Reduced Particle Model as a 2X2 System

We now return to our reduced particle model:

$$\begin{aligned} \frac{\partial(\rho(\alpha)h)}{\partial t} + \{\frac{\rho(\alpha)^2}{\mu(\alpha)}h^3\}_x &= 0 \qquad (6.10) \\ \frac{\partial(\alpha h)}{\partial t} + \{\frac{\alpha\rho(\alpha)}{\mu(\alpha)}h^3 + \frac{2}{3}V_s \alpha h f(\alpha)\}_x &= 0 \qquad (6.11) \end{aligned}$$

Denoting $u = \rho(\alpha)h$ and $v = \alpha h$, we can rewrite the above as

$$\begin{aligned} u_t + (V_1 u)_x &= 0 \qquad (6.12) \\ v_t + (v(V_1 + V_2))_x &= 0 \qquad (6.13) \\ V_1 &= \frac{\rho(\alpha)h^2}{\mu(\alpha)} \qquad (6.14) \\ V_2 &= \frac{2}{3}V_s f(\alpha) \qquad (6.15) \end{aligned}$$

So it remains to write V_1 and V_2 in terms of the system variables u and v. Substituting in the definition for $\rho(\alpha)$ and $\mu(\alpha)$, after some algebra, we have the following relations

$$\begin{aligned} \alpha &= \frac{v}{u - \Delta v} \qquad (6.16) \\ h &= u - \Delta v \qquad (6.17) \\ \rho(\alpha) &= \frac{u}{u - \Delta v} \qquad (6.18) \end{aligned}$$

These give

$$V_1 = u(u-\Delta v)(1-\frac{v}{(u-\Delta v)\alpha_M})^2 \tag{6.19}$$

$$V_2 = \frac{2}{3}V_s(1-\frac{v}{u-\Delta v})^6 \tag{6.20}$$

The next step is to compute the Jacobian matrix, which we can write in terms of V_1 and V_2:

$$J = \begin{pmatrix} V_1 + u\partial_u V_1 & u\partial_v V_1 \\ v(\partial_u V_1 + \partial_v V_2 & V_1 + V_2 + v(\partial_v(V_1+V_2)) \end{pmatrix} \tag{6.21}$$

We then have to compute the eigenvalues and eigenvectors and solve the connection problem. We assume that we have both a 1-shock and a 2-shock, and we can validate this assumption later from the results. We will illustrate the computation process by solving 2 typical cases: flows with 30% and 45% initial concentrations. We will be able to obtain the speed at which the 2 fronts are traveling as well as the height and concentration of the intermediate states. These results can then be compared to the simulation plots previously shown: Figure 6-2 and Figure 6-3.

6.4.1 Mixture of 30% Initial Concentration

In this case, we have a mixture with uniform initial concentration of 30% flowing down the inclined plane. The flow has a dimensionless height of 1.0 at the gate (left state). To be consistent with the simulation, the precursor film thickness is assumed to be 0.1 (right state). The left and right state (u_l, v_l), (u_r, v_r) can then be determined.

The next step is to plot in the $u-v$ plane all the values of u_i and v_i which form allowable connections. Equations 6.6-6.7 provides us with a family of allowable u_i, v_i that forms allowable connections to the left state u_l, v_l. Similarly, we obtain another family of allowable u_i, v_i that forms allowable connections to the right state u_r, v_r by solving Equations 6.8-6.9. The point where these 2 curves intersect is the intermediate state that connects to both the left and right states. If these 2 curves do not intersect, then we may have 1-rarefaction instead of 1-shock and our assumption is incorrect. Figure 6-5 shows the 2 lines traced from left state and right state respectively. The two lines clearly intersect each other at $(u_i, v_i) = (2.070, 0.492)$. Indeed, we have both

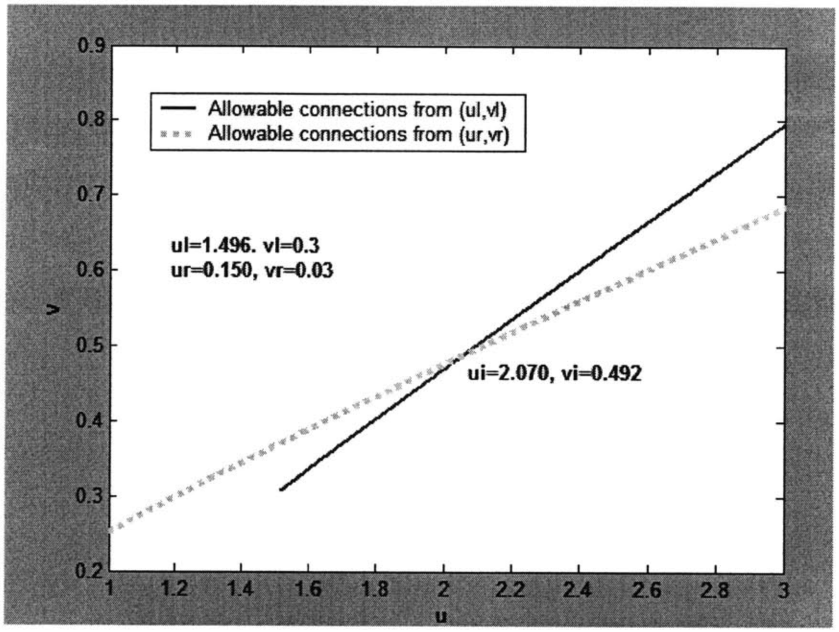

Figure 6-5: *Allowable connections to the left state and the right state respectively for a 30% initial concentration mixture flow. The two lines traced from the left and the right states intersect to give the intermediate state* u_i, v_i.

1-shock and 2-shock for this particular flow. Based on the intermediate state in $u-v$, we can solve for the intermediate height h_i and intermediate concentration α_i. It is found that $h_i = 1.26$ and $\alpha_i = 0.39$. In Figure 6-2, the intermediate state at where the plateau forms, has height and concentration exactly the same value as predicted from the shock theory analysis.

We can easily obtain the 1-shock speed and 2-shock speed by substituting the calculated u_i, v_i into Equations 6.6-6.9. 1-shock speed s_1 and 2-shock speed s_2 are $s_1 = 0.434$, $s_2 = 0.485$ respectively. The 2 speeds calculated also agree very well with the corresponding speed measured from the simulation plots. So, we have a mechanism to accurately predict the speed at which the fronts travel. The difference between these two gives us the rate at which the width of the bump increases. To complete the analysis, we need to check the eigenvalues for the left, right and intermediate states, and validate that the entropy conditions are met. The results are summarized in Table 6.1.

Left State	Right State	Intermediate State
$(h_l, \alpha_l) = (1.0, 0.30)$	$(h_r, \alpha_r) = (0.1, 0.30)$	$(h_i, \alpha_i) = (1.26, 0.39)$
$(u_l, v_l) = (1.496, 0.300)$	$(u_r, v_r) = (0.150, 0.030)$	$(u_i, v_i) = (2.070, 0.492)$
$\lambda_1(u_l, v_l) = 0.4362$	$\lambda_1(u_r, v_r) = -0.0315$	$\lambda_1(u_i, v_i) = 0.4326$
$\lambda_2(u_l, v_l) = 1.3484$	$\lambda_2(u_r, v_r) = 0.0095$	$\lambda_2(u_i, v_i) = 1.3326$
$s_1 = 0.4339$: $\lambda_1(u_l, v_l) > s_1 > \lambda_1(u_i, v_i)$, $\lambda_2(u_l, v_l) > s_1$, $\lambda_2(u_i, v_i) > s_1$		
$s_2 = 0.4848$: $\lambda_2(u_i, v_i) > s_2 > \lambda_2(u_r, v_r)$, $\lambda_1(u_i, v_i) < s_2$, $\lambda_1(u_r, v_r) < s_2$		

Table 6.1: *Summary of shock theory analysis on a mixture flow of initial concentration* 30%

6.4.2 Mixture of 45% Initial Concentration

In this section, we present the results from the same type of shock analysis, but on a mixture with high concentration: 45% initial concentration. Once again, we plot the

	Full Model	Reduced Model	Shock Theory
h_i	1.25	1.25	1.257
α_i	0.389	0.389	0.3915
s_1	0.448	0.434	0.4339
s_2	0.488	0.485	0.4848

Table 6.2: *Summary of intermediate states and wave traveling speeds of* 30% *initial concentration mixtures obtained by full model simulation, reduced model simulation and shock theory analysis.*

possible intermediate states u_i, v_i in the $u - v$ plane. As shown in Figure 6-6, the 2 lines intersect at $(u_i, v_i) = (2.892, 0.820)$.

Similar to the lower concentration case, we have both 1-shock and 2-shock for flows with 45% initial concentration. The intermediate state which connects to both the 1-shock and the 2-shock is at $h_i = 1.54$ and $\alpha_i = 0.53$. We see that in the case of higher initial concentration, the intermediate state occurs at larger thickness and higher concentration. This is the main reason that the plot from the simulation (Figure 6-3) has just started developing an intermediate plateau structure almost at the end of our simulation time. The intermediate state enables us to compute the 1-shock and 2-shock speeds: $s_1 = 0.1777$, $s_2 = 0.1956$. Comparing to the speeds obtained for flows with 30% initial concentration, mixture of higher concentration indeed flows slower. The eigenvalues are calculated and it is verified that all entropy conditions are met.

Figure 6-7 plots the height of the intermediate state against the precursor film thickness for mixtures of different initial concentrations. Intermediate states are affected by both the initial concentration and the precursor film thickness. The height of the intermediate state increases with the initial concentration and thinner precursor film results in greater intermediate state height. No intermediate state is observed for mixtures of high concentration and small precur film. In these cases, the concentration at the bump reaches the maximum packing number. Figure 6-8 shows the

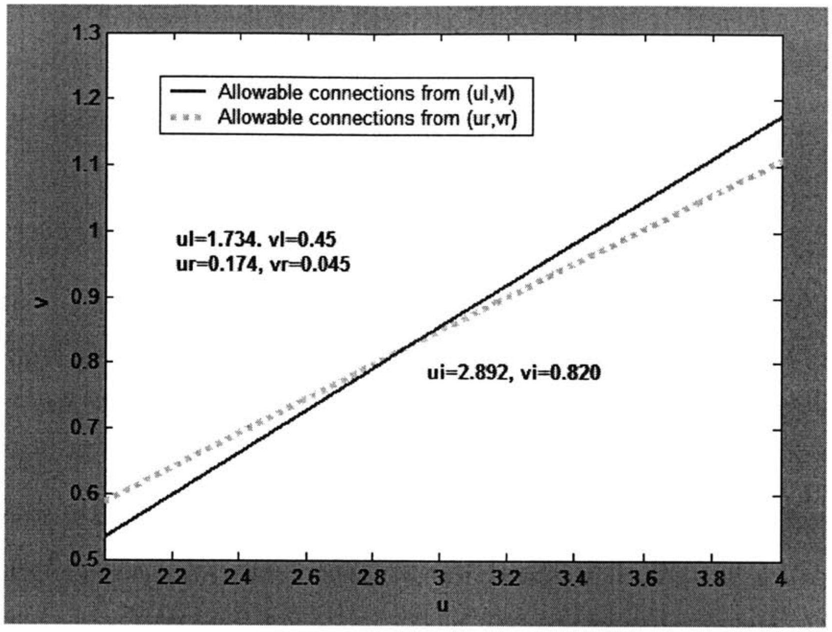

Figure 6-6: *Allowable connections to the left state and the right state respectively for a* 45% *initial concentration mixture flow.*

Left State	Right State	Intermediate State
$(h_l, \alpha_l) = (1.0, 0.45)$	$(h_r, \alpha_r) = (0.1, 0.45)$	$(h_i, \alpha_i) = (1.54, 0.53)$
$(u_l, v_l) = (1.744, 0.450)$	$(u_r, v_r) = (0.174, 0.045)$	$(u_i, v_i) = (2.892, 0.820)$
$\lambda_1(u_l, v_l) = 0.1756$	$\lambda_1(u_r, v_r) = -0.0214$	$\lambda_1(u_i, v_i) = 0.1787$
$\lambda_2(u_l, v_l) = 0.5514$	$\lambda_2(u_r, v_r) = 0.0038$	$\lambda_2(u_i, v_i) = 0.5423$
$s_1 = 0.1777$: $\lambda_1(u_l, v_l) > s_1 > \lambda_1(u_i, v_i)$, $\lambda_2(u_l, v_l) > s_1$, $\lambda_2(u_i, v_i) > s_1$		
$s_2 = 0.1956$: $\lambda_2(u_i, v_i) > s_2 > \lambda_2(u_r, v_r)$, $\lambda_1(u_i, v_i) < s_2$, $\lambda_1(u_r, v_r) < s_2$		

Table 6.3: *Summary of shock theory analysis on a mixture flow of initial concentration* 45%

	Full Model	Reduced Model	Shock Theory
h_i	1.54	1.54	1.537
α_i	0.534	0.534	0.5337
s_1	0.184	0.180	0.1777
s_2	0.198	0.195	0.1956

Table 6.4: *Summary of intermediate states and wave traveling speeds of* 45% *initial concentration mixtures obtained by full model simulation, reduced model simulation and shock theory analysis.*

concentration of the intermediate state. We also observe that the concentration of the intermediate state increases with initial concentration and with thinner precursor film.

6.5 Complex Eigenvalues at Precursor Film

We have demonstrated in the previous section that we can obtain the wave speed and the bulk flow characteristics by applying the classical shock theory on a 2X2 system of conservation laws. Moreover, we have shown that the reduced system captures the main features of the full system, and solving the reduced system provides an alternative and easier means to solve the full system. For the 30% and 45% initial concentration cases we presented, with a precursor film thickness of 0.1, both systems result in 1-shock and 2-shock connected through an intermediate state. For these 2 cases, the shock theory accurately solves the shock speed and predicts the intermediate state.

Unfortunately, the shock theory breaks down at flow regimes with certain combinations of precursor film thickness and initial concentration. Recall that in order to ensure that the theory works, we must have 2 real and distinct eigenvalues. The eigenvalues are real if the discriminant of the J-matrix is positive. The J-matrix is

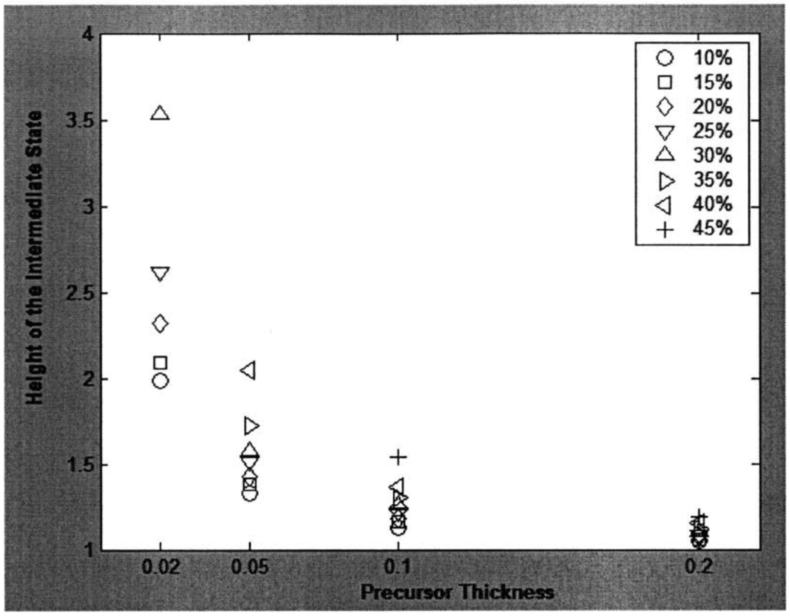

Figure 6-7: *Height of the intermediate state against precursor thickness for mixtures of different initial concentrations.*

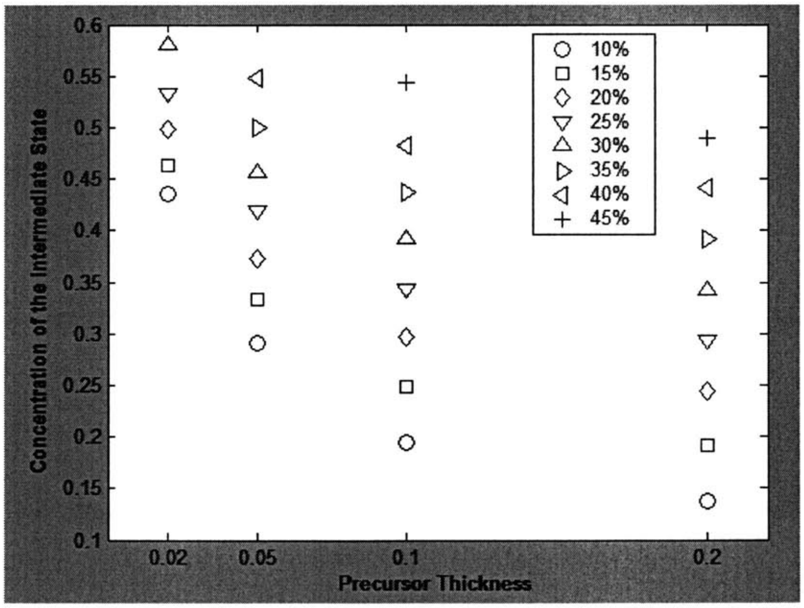

Figure 6-8: *Concentration of the intermediate state against precursor thickness for mixtures of different initial concentrations.*

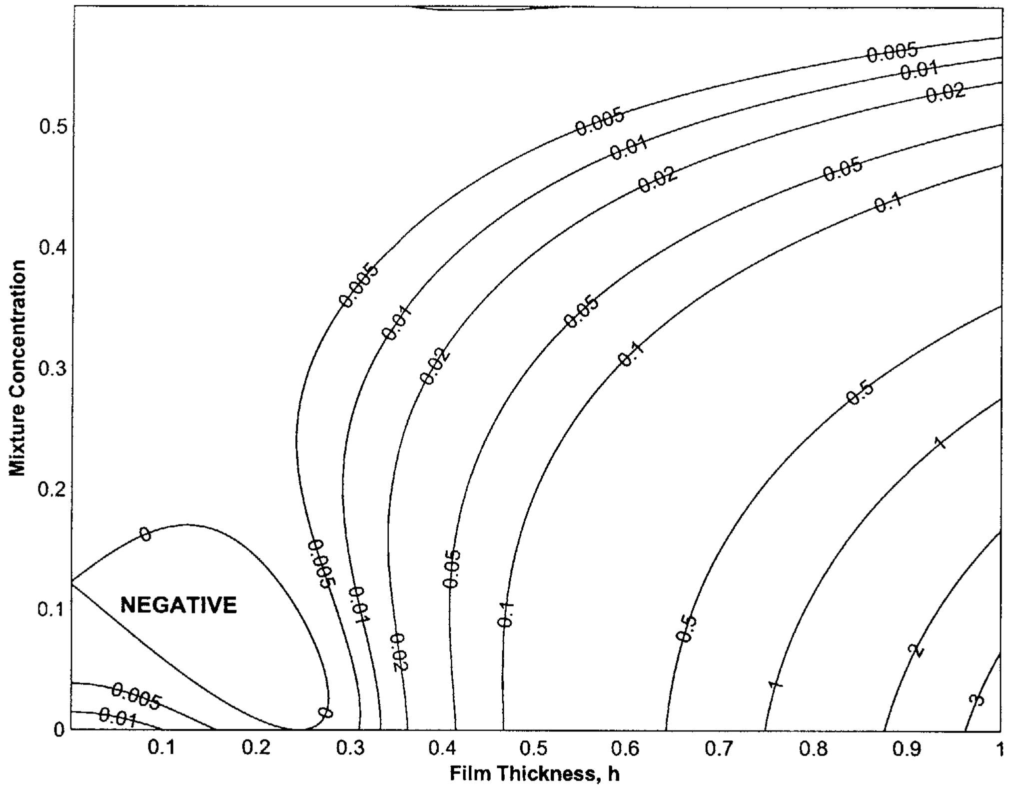

Figure 6-9: *Contour plot of the J-matrix discriminant. The horizontal axis is the height of the film and the vertical axis is the concentration. Discriminant is negative at small film thickness and low concentration.*

given by 6.21, and the discriminant for the matrix is:

$$Discriminant = (J(1,1)+J(2,2))^2 - 4\times(J(1,1)\times J(2,2) - J(2,1)\times J(1,2)) \quad (6.22)$$

Figure 6-9 is a plot of the resulting discriminant when we vary the film thickness and particle concentration. It is clear from the contour plot that the discriminant is positive for most flow regimes except at low concentration and small film thickness. The contour plot reveals that the shock theory breaks down at the precursor film for our current model.

Compared to the pure viscous fluid case, our reduced model has an extra settling velocity piece. To explain the negative discriminant for some values of the precursor film, we note that the settling velocity in our current model only depends on particle concentration, but does not depend on the thickness of the film. It has long been known that the settling of particles slows down when the particles are very close to the wall. Happel and Brenner [29] worked out an expression for the velocity change when a spherical particle very close to a vertical wall drops down. The settling velocity is modified by a factor $s(z)$, which depends on the distance from center of the spherical particle to the wall.

$$s(z) = 1 - \frac{9}{16}\frac{a}{z} + \frac{1}{8}(\frac{a}{z})^3 - \frac{45}{256}(\frac{a}{z})^4 - \frac{1}{16}(\frac{a}{z})^5 \tag{6.23}$$

Where a is the particle radius. As before, we need to integrate this expression. The limits of integration are from the particle radius a to the free surface height h. The integration yields

$$\int_a^h s(z) = h[1 - \frac{259}{256}\frac{a}{h} + \frac{9}{16}\frac{a}{h}ln\frac{r}{h} - \frac{1}{16}(\frac{a}{h})^3 + \frac{15}{256}(\frac{a}{h})^4 + \frac{1}{64}(\frac{a}{h})^5] \tag{6.24}$$

If we denote the terms in the square bracket as $w(h)$, then the modified settling velocity term becomes

$$\frac{2}{3}V_s\alpha hf(\alpha)w(h) \tag{6.25}$$

The added function $w(h)$ involves the ratio a/h in each of its terms. Since the distance of the particle from the wall is measured from the wall to its center, the expression is only defined for $a > h$. The particles used in the experiments have an average radius of approximately $330\mu m$. This translates to $a = 0.33$ in dimensionless length scale.

The expression we have derived based on Happel and Brenner's findings points out that the settling velocity decreases as the particles move very close to a wall and the effect diminishes when the particles are further away. For the film thickness we are dealing with in our flow, especially the precursor film, this wall effect on the particle settling velocity is definitely important. Therefore, our current approach of taking the settling velocity independent of thickness of the film is questionable. It is likely that the settling velocity at the precursor film is so much larger than the realistic values that it drives the discriminant negative.

We can modify our current model by including the function $w(h)$ to account for the wall effect. However, $w(h)$ derived above is only valid for $h > a$. Since our model

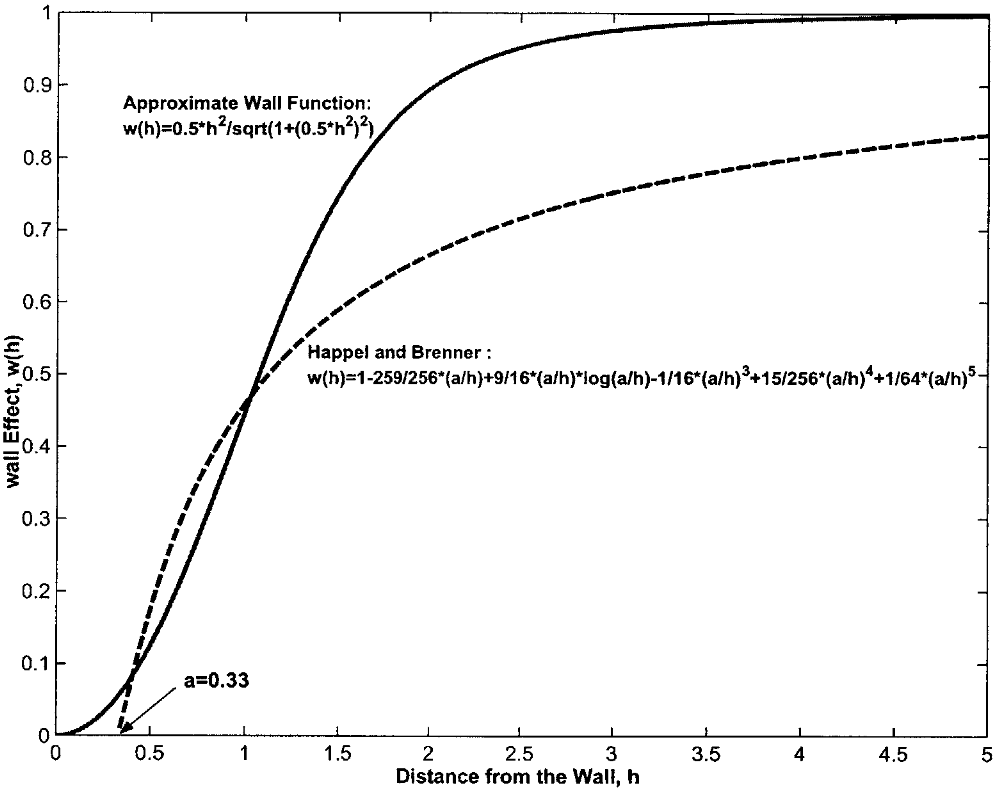

Figure 6-10: *Function value* $w(h)$ *against the film thickness* h. ***Dashed line:*** $w(h)$ *is derived from Happel and Brenner's study on settling velocity near a wall.* $w(h)$ *is* 0 *at particle radius* a, *and it approaches* 1 *when height increases.* ***Solid line:*** *A much simpler approximation that starts at zero film thickness.*

follows a continuum approach, we would like an expression of $w(h)$ that is defined at distance less than the apparent particle radius. In fact, our precursor film is less than 0.1, which is smaller than the particle radius. So, if we were to use this expression, we need to find an approximation to the original $w(h)$ that also passes through the origin. Alternatively, since we do not necessarily need an expression that involves 4th or 5th power, we can look for a simpler expression that takes similar values. By trial and error, we find that $w(h) \sim h^2$ can successfully resolve the negative discriminant issue. If we normalize the wall function such that the function takes value of 0 when $h = 0$, and it approaches 1 when $h \longrightarrow \infty$, we find one possbility:

$$w(h) = \frac{0.5h^2}{\sqrt{1 + (0.5h^2)^2}} \tag{6.26}$$

Figure 6-10 shows the function value $w(h)$ with respect to h for both the original Happel and Brenner function and our approximate function. The approximate function allows us to calculate the wall effect on settling velocity for any film thicknesses. When the approximate wall function is included in the settling velocity, the resulting discriminant is shown in the contour plot: Figure 6-11. Note that unlike Figure 6-9 the discriminant is always possitive within the range considered in this plot.

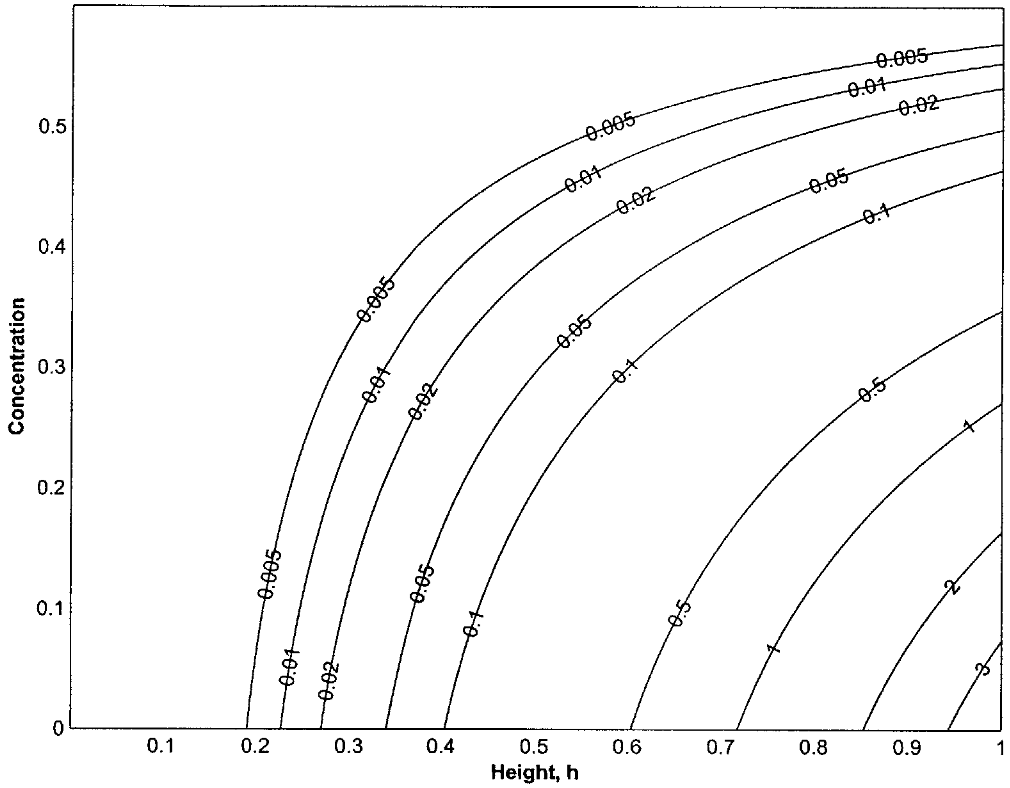

Figure 6-11: *Contour plot of the J-matrix discriminant that includes the function $w(h)$ in the settling velocity term.*

Chapter 7

Summary and Future Directions

In this thesis, we have derived a mathematical model for simulating and predicting the flow behaviors of thin film particle laden flow down an inclined plane under gravity.

7.1 Summary

The study of thin film flow under the influence of gravity has numerous applications both in industrial processes and in the geophysical world. In Chapter 1, we presented the results from past research on viscous fluid flow down an inclined plane. When a viscous thin film flows down an inclined plane, an initially uniform straight front becomes unstable, and saw-tooth or fingers of rivulet shapes form at the leading edge of the flow. Theoretical and numerical studies indicate that the presence of the bump at the front due to surface tension is the key factor that drives the instability. In the absence of surface tension, no bump is formed and the flow is stable. We introduced the notion of adding an extremely thin precursor film at the contact line that helps to remove the singularity. In Chapter 1, we also discussed the past studies made on suspension flows and granular flows. Surprisingly, studies have revealed that suspension flows and granular flows, too, exhibit contact line instabilities although the mechanism that induces the instability is different. In such cases, the driving force for the instability is known as Rayleigh-Taylor instability where adverse density stratification resulting from rapid shearing motion in heavy particle flow causes the flow to be unstable to spanwise disturbances. These past results have shown that contact line instability is a common feature to thin film flows, whether in the case of pure viscous fluid or in the case of granular flow. However, very few studies have made on flows where both particles and viscous fluid are present in the form of a well-mixed mixture. This motivates the current study - a particle laden flow down an inclined plane under gravity.

In Chapter 2, we looked into the effect of particles on mixture properties. Generally, the presence of particles increases viscosity which blows up when the particle concentration reaches the maximum packing number. Besides viscosity, mixture concentration also has an effect on settling velocity. In clear fluid, a single particle settles at Stokes velocity. However, in the presence of neighboring particles, the settling velocity decreases because of increased hindrance. This phenomenon is known as hindered settling velocity. The most widely used hindered settling velocity function is the one proposed by Zaki (2.11). We also discussed more complicated issues involving particles such as particle velocity fluctuations and viscous resuspensions. These clearly suggest that the study on particle laden flow is a very complicated problem if we were to consider all of these issues. Therefore, in our current study, we aim to propose a much simplified model which omits some of the more complicated issues and at the same time is able to capture the bulk flow characteristics.

Benjamin Dupuy performed experiments using silicon oil or glycerin and particles of various sizes. He observed that particle size can greatly influence the settling rate and thus the resulting flow behavior. If the particles are too big, the settling velocity is so fast that the particles quickly drop out from the mixture and the mixture essentially becomes pure viscous fluid in a short period of time after being released. On the other hand, if the particles are so small such that the settling of particles are almost negligible, the mixture behaves as if it is a pure viscous fluid but with modified properties. The flow is most interesting when the particles are of intermediate size and the settling velocity is of the same order as the bulk flow velocity of the mixture. Benjamin Dupuy conducted a series of experiments with particles of this intermediate size, and he was able to map out a phase diagram that describes the flow regime observed under different initial particle concentration and the slope inclination angle. He categorized the flows into 3 different regimes: clear fluid fingers that occur at low concentration and low inclination angle; fingers of suspension that occur at intermediate concentration and inclination angle; and ridge formation that occurs at high concentration and high inclination angle. The experimental results obtained by Benjamin Dupuy clearly demonstrated that our study on particle laden flow down an inclined plane involve two time scales: the rate at which the mixture and the particles are transported downslope, and the rate at which the particles settle out. Depending on the relative rate of these two, we observe different flow behaviors.

With this background research and experimental exploration, we derive a mathematical model in Chapter 4. We use a mixture model which has uniform fluid properties depending on the local particle concentration in the fluid. The equations are formulated in terms of volume averaged velocities because this is expected to facilitate the numerical treatment of the incompressibility condition. Our problem consists of two unknowns: the film thickness and the particle concentration. The flow is completely described if these two quantities are known. The first equation that describes the height evolution of thin film flow can be obtained by applying conservation of momentum to the flow, and then simplifying it through low Reynolds number flow assumption and lubrication assumption. Due to the presence of particles, we need a second equation to account for the change in particle concentration in the mixture. This particle evolution equation is obtained by applying conservation of particles to a control volume. To simplify the analysis, we further assume that there is no variation in the spanwise direction, and change across the film thickness is very small. So, we depth-average the fluid properties and assume the properties are everywhere the same across the film thickness at a particular distance down the slope. To finish the derivation, the equations are non-dimensionalized to yield the system of dimensionless equations: 4.48-4.49. Comparing to the thin film equation for the pure viscous fluid, our system of equations depends on density and viscosity of the mixture because these quantities are functions of particle concentration and therefore vary as the mixture travels downslope. The extra particle equation has a settling velocity term that takes into account that particles are settling due to gravitational force. Because of the difficulties involving modeling the normal component of the settling velocity, only the settling velocity component that is parallel to the mixture flow is included in the current study. Therefore, the results obtained in this thesis best describes the ridge formation regime in which essentially all particles are transported downstream.

In Chapter 5, we present results obtained from numerical simulations on the system of equations derived in Chapter 4. As expected, the resulting flow profiles depend on inclination angle and initial concentration. Mixtures with higher initial concentration flow slower than those with lower initial concentration. All of these flows form a bump at the leading edge, and the bump formed is significantly larger than that formed by surface tension alone in pure viscous fluid. The bump height increases as the initial particle concentration increases. Within the simulation time, flow profiles from lower concentration mixtures also develop an interesting intermediate plateau structure, on which a secondary smaller bump is formed. As the mixture flows downstream, the bump thickness grows because the leading edge and the trailing edge travel at different speeds. Unlike pure viscous fluid, our particle laden flows do not seem to reach steady state, at least not within our reasonably long period of simulation time. We also studied the effect of precursor film thickness on the resulting profiles. We found that choice of precursor film has a profound influence on the final flow profile. Thinner precursor film results in a much bigger bump. On the other hand, plateau structure is formed when thicker precursor film is used. Many interesting flow features were introduced in this chapter. These flow features led us to ask questions such as the intermediate state that characterizes the plateau structure and the wave speeds at which the leading edge and the trailing edge travel.

The full system of equations are too complicated to analyze, especially with the high order terms. In Chapter 6, we present simulation results obtained from the reduced system, that includes only the low order transport and settling velocity terms. Simulation on the reduced system shows that the reduced system is able to capture the bulk flow characteristics of the full system, such as the front traveling speed and the bump height. We further introduced classical shock theory to solve our 2X2 system of conservation laws. Based on the shock theory, we found that systems in which we observe an intermediate plateau structure, actually consist of a 1-shock at the leading front and a 2-shock at the trailing front. The two shock waves are connected by an intermediate state which is manifested in the form of a plateau structure. The two fronts separate from each other because the leading front travels faster. This explains the growth of bump width as the mixture flows down. Basically, the full system can be understood by solving the much simpler reduced system. When the reduced system has two real and distinct eigenvalues at the left state (far upstream), the intermediate state and the right state (far downstream), shock theory successfully solves the reduce system and predicts the wave speeds as well as the intermediate state.

7.2 Future Direction

Many of the problems presented here were only briefly studied and thus are in need of further analysis, moreover, our model is very simplified and therefore it is only good for a limited range of flow regimes. Below are the few areas that need to be further studied to improve our current model.

First of all, our current model only includes the parallel component of the settling velocity. In reality, particles settle out from the mixture and the concentration of particles decreases in flows with smaller particle concentration and inclination angle. The main difficulty of modeling the normal component in our current model is our assumption of uniform property across the depth of the film. If we were to use the depth averaged concentration to calculate the normal component, it is likely to be inaccurate. Therefore, to include the normal component in the future, a more complicated 2-D model that involves both x-direction (along the slope) and z-direction (across the film thickness normal to the slope) variations need to be used. Alternatively, an easier approach would be to insert a function that accounts for the effect of wall and accumulation of particles near the bottom on the settling velocity. The ultimate goal is to give the right magnitude to the normal component of the settling velocity such that similar to the phase diagram of Benjamin Dupuy's experimental results, our model simulations also produce 3 flow regimes depending on inclination angle and initial particle concentration.

This thesis has been focusing on coming up with a good model to accurately predict the base state of the particle laden flow. Due to time constraint, no linear stability analysis were performed. In the future when base state can be accurately predicted, linear stability analysis should be performed to calculate the most unstable wave length as well as fingering shapes. Benjamin Dupuy observed in his experiment that the front becomes stable when a ridge structure forms under high slope angle and high concentration. Linear stability analysis would be helpful to test whether contact lines of certain flow regimes are indeed linearly stable. Our preliminary study on the base state seems to suggest that the flow profile does not reach a steady state. If this is indeed the case, then a more complicated time dependent linear stability analysis has to be used.

In Chapter 6, we discussed the complex eigenvalue issue with our current model. We suggested including a wall function into the settling velocity. We have to perform simulations to check the effect of this wall function on the resulting flow profiles. As for the shock theory analysis on the reduced system, we have yet to determine whether an intermediate state exists for all flow regimes and whether we always have 1-shock and 2-shock at both fronts. If an intermediate state does not exist for some flows, we may have 1-rarefaction instead of 1-shock. So, more studies need to be made to further categorize all possible flow regimes.

We presented in Chapter 5 that choice of precursor film thickness has a great influence both on the resulting bump height and the resulting bulk flow structure. We need to determine whether we would observe the same kind of change on flow profiles when the slope is pre-wetted by a layer of mixture. If this dependence of flow profile on precursor film thickness is purely an artifact created by our particular model, then we may need to refine our model to reduce the influence of precursor film. After all, precursor film is an artificial layer that we introduce at the contact line to circumvent the singularity problem.

Appendix A

1-Rarefaction Wave at the Trailing Edge

In the case that we have 1-rarefaction wave at the trailing front, we can still solve the connection problem. Rarefaction waves are similarity solutions centered at the origin. They have the simple scaling structure $(u, v) = (U(x/t), V(x/t))$. Plugging this into Equations 6.3 - 6.4, and separating variables gives the vector equation

$$[J(u,v) - \xi I] \begin{pmatrix} U'(\xi) \\ V'(\xi) \end{pmatrix} = 0 \tag{A.1}$$

where $\xi = x/t$ is the similarity variable. The nontrivial solution of the matrix equation gives us the shape of the rarefaction wave. The solution satisfies the ODE-eigenvalue problem

$$\xi = \lambda(U, V) \tag{A.2}$$

$$\begin{pmatrix} U'(\xi) \\ V'(\xi) \end{pmatrix} = \alpha r(U, V) \tag{A.3}$$

Since we are considering the 1-wave, we take $\lambda = \lambda_1$. Note that we can simplify this to a coupled ODE alone by first differentiating A.2 with respect to ξ to obtain

$$1 = \lambda(U,V)' = U'\lambda_u + V'\lambda_v = \begin{pmatrix} U'(\xi) \\ V'(\xi) \end{pmatrix} \cdot \nabla\lambda = \alpha r \cdot \nabla\lambda$$

We assume the genuinely nonlinear condition, which means we can normalize the eigenvector so that

$$r \cdot \nabla\lambda = 1 \tag{A.4}$$

Using this convention, we have a simple shooting problem to solve for the shape of the rarefaction wave. We compute below the 1-wave solution.

Given a left state (u_l, v_l), there exists a one parameter family of states (u_i, v_i) which connect through a centered rarefaction wave. The shape of the wave (U, V) described above, is determined by solving the initial value ODE problem

$$U' = R_1(U, V), \quad V' = R_2(U, V), \quad (U, V)_{\xi=\lambda_1(u_l, v_l)} = (u_l, v_l) \tag{A.5}$$

where the functions R_1 and R_2 are respectively the first and second components of the eigenvector r, associated with the first eigenvalue λ_1, normalized as in A.4. let $(U(\xi), V(\xi))$ denote the unique solution of this ODE. Then for any $\xi_1 > 0$, the above describes a centered rarefaction wave connecting the left state $(u_l, v_l$ to the right state $(U(\xi_1), V(\xi_1))$. In this way we obtain a one parameter family of rarefaction solutions. Note that the characteristic speeds of a constant states are determined by the eigenvalues, and we can describe the full solution as

$$\begin{aligned} (u(x,t), v(x,t)) &= (u_l, v_l), \quad x < \lambda_1 t \\ (u(x,t), v(x,t)) &= (U(x/t), V(x/t)), \quad \lambda_1 t < x < \lambda_1(\xi_1)t \\ (u(x,t), v(x,t)) &= (U(\xi_1, V(\xi_1)), \quad \lambda_1(\xi_1)t < x \end{aligned}$$

where $\lambda_1(\xi_1)$ denotes the first eigenvalue for $(u, v) = (U(\xi_1), V(\xi_1))$. Varying ξ_1 gives a one parameter family of rarefaction waves.

Bibliography

[1] R. Mauri A. Acrivos and X. Fan. Shear induced resuspension in a couette device. *Int. Jour. of Multi. Flow*, 19:797–802, 1993.

[2] X. Fanton A. L. Bertozzi, A. ¨'Munch and A. M. Cazabat. Contact line stability and 'undercompressive shocks' in driven thin film flow. *Phys. Rev. Lett.*, 81(23):5169–5172, 1998.

[3] M. A. Scherer A. Engel A. Lange, M. Schröter and I. Rehberg. Fingering instability in a water-sand mixture. *Eur. Phys. J. B*, 4:475, 1998.

[4] R. A. Bagnold. *Proc. R. Soc. London, Ser. A*, 225:49, 1954.

[5] E. Barnea and J. Mizrahi. A generaized approach to the fluid dynamics of particulate systems: Part 1. genearal correlation for fluidization and sedimentation in solid multiparticle systems. *Chem. Eng. J.*, 5:171–189, 1973.

[6] G. K. Batchelor. Sedimentation in a dilute dispersion of spheres. *J. Fluid Mech.*, 52:245, 1972.

[7] A. L. Bertozzi and M. P. Brenner. Linear stability and transient growth in driven contact lines. *Phys. Fluids*, 9:530, 1997.

[8] M. P. Brenner. Instability mechanism at driven contact lines. *Phys. Rev. E*, 47:4597, 1993.

[9] W. Pesch C. Völtz and I. Rehberg. Rayleigh-taylor instability in a sedimenting suspension. *Phy. Rev. E*, 65:011404, 2001.

[10] R. E. Caflisch and J. H. C. Luke. Variance in the sedimentation speed of a suspension. *Phys. Fluids*, 28:259, 1985.

[11] I. C. Carpen and J. F. Brady. Gravitational instability in suspension flow. *J. Fluid Mech.*, 472:201–210, 2002.

[12] R. H. Davis and A. Acrivos. Sedimentation of noncolloidal particles at low reynolds numbers. *Annu. Rev. Fluid Mech.*, 17:91–118, 1985.

[13] J. R. de Bruyn. Growth of fingers at a driven three-phase contact line. *Phys. Rev. A*, 46:R4500, 1992.

[14] P. G. de Gennes. Wetting: Statics and dynamics. *Rev. Mod. Phys.*, 57:827, 1985.

[15] B. Deryagin. *Koloidn. Zh.*, 17:191, 1955.

[16] B. Dupuy. Instabilities in particle-laden flows down an inclined plane, 2004.

[17] E. B. Dussan. Spreading of liquids on solid-surfaces - static and dynamic contact lines. *Ann. Rev. Fluid Mech.*, 11:371, 1979.

[18] A. Q. Shen E. Fried and S. T. Thoroddsen. Wave patterns in a thin layer of sand within a rotating horizontal cylinder. *Phys. Fluids*, 10:10, 1998.

[19] A. Einstein. *Ann. Phys. lpz.*, 19, 1906.

[20] Y. Forterre and O. Pouliquen. Longitudinal vortices in granular flows. *Phys. Rev. Lett*, 86:5886–5889, 2001.

[21] F. A. Gadala-Maria. *The rheology of concentrated suspensions.* PhD thesis, Stanford Univ, 1979.

[22] J. Garside and M. R. Al-Dibouni. Velocity-voidage relationship for fluidization and sedimentation in solid-liquid systems. *Ind. Eng. Chem. Process Des. Dev.*, 16:206–214, 1977.

[23] R. Goodwin and G.M. Homsy. Viscous flow down a slope in the vicinity of a contact line. *Phys. Fluids A*, 3:5, 1991.

[24] H.P. Greenspan. Motion of a small viscous droplet that wets a surface. *J. Fluid Mech.*, 84:125, 1978.

[25] C. E. Brennen H. Ahn and R. H. Saversky. Measurements of velocity, velocity fluctuation, density, and stresses in chute flows of granular materials. *ASME J. Appl. Mech.*, 59:119, 1991.

[26] E. J. Hinch L. Oger H. Nicolai, B. Herzhaft and E. Guazzeli. Particle velocity fluctuations and hydrodynamic self-diffusion of sedimenting non-brownian spheres. *Phys. Fluids*, 7:12, 1995.

[27] P. J. Haley and M. J. Miksis. The effect of the contact line on droplet spreading. *J. Fluid Mech.*, 223:57, 1991.

[28] J. M. Ham and G. M. Homsy. Hindered settling and hydrodynamic dispersion in quiescent sedimenting suspensions. *Int. J. Multiphase Flow*, 14:533–546, 1988.

[29] J. Happel and H. Brenner. *Low Reynolds number hydrodynamics.* Prentice-Hall, 1965.

[30] L. Hocking. Spreading and instability of a viscous fluid sheet. *J. Fluid Mech.*, 221:373, 1990.

[31] C. Huh and S.G. Mason. Effects of surface-roughness on wetting (theoretical). *J. Colloid Interface Sci.*, 60:11, 1977.

[32] O. Hungr and N. R. Morgenstern. Experiments on the flow behaviour of granular materials at high velocity in an open channel. *Geotechnique*, 34:405, 1984.

[33] H. E. Huppert. Flow and instability of a viscous current down a slope. *Nature*, 300:427–429, December 1982.

[34] A. Indekina I. Veretennikov and H.-C. Chang. Front dynamics and fingering of a driven contact line. *J. Fluid Mech*, 373:81, 1998.

[35] L.Kondic J. Diez and A. L. Bertozzi. Global models for moving contact lines. *Phys. Rev. E*, 63:011208, 2001.

[36] A. L. Bertozzi J. Sur and R. Behringer. Reverse undercompressive shock structures in driven thin film flow. *Phys. Rev. Lett.*, 90(12), 2003.

[37] J. M. Jerret and J. R. de Bruyn. Fingering instability of a gravitationally driven contact line. *Phys. Fluids A*, 4:234, 1992.

[38] S. Kalliadasis. Nonlinear instability of a contact line driven by gravity. *J. Fluid Mech.*, 413:355, 2000.

[39] L. Kondic and J. Diez. Pattern formation in the flow of thin films down an incline: Constant flux configuration. *Phys. of Fluids*, 13:3168–3184, 2001.

[40] I. M. Krieger. Rheology of monodisperse lattices. *Adv. Colloid Interface Sci.*, 2:111–136, 1972.

[41] W. R. Debler L. M. Hocking and K. E. Cook. The growth of leading edge distortions on a viscous sheet. *Phys. Fluids*, 11:307, 1999.

[42] A. J. C. Ladd. Hydrodynamic screening in sedimenting suspensions of non-brownian spheres. *Phys. Rev. Lett.*, 76:1392, 1996.

[43] D. R. Leighton and A. Acrivos. Measurement of shear-induced self-diffusion in concentrated suspensions. *J. Fluid Mech.*, 181:415–439, 1987.

[44] R. A. Schluter M. F. G. Johnson and S. G. Bankoff. Experimental study of rivulet formation on an inclined plate by fluorescent imaging. *J. Fluid Mech.*, 394:339, 1999.

[45] L. W. Schwartz M. H. Eres and R. V. Roy. Fingering phenomena for driven coating films. *Phys. Fluids*, 12:1278, 2000.

[46] J. F. Morris and J. F. Brady. Pressure-driven flow of a suspension: buoyancy effects. *Intl J. Multiphase Flow*, 24:105–130, 1998.

[47] A. Mileo N, Tuirumkudulu and A. Acrivos. Particle segregation in monodisperse sheared suspensions in a partially filled rotating horizontal cylinder. *Phys. Fluids*, 12:1615, 2000.

[48] M. S. Nigam. *Numerical Modeling of Suspension Flows.* PhD thesis, Massachusetts Institute of Technology, 1999.

[49] P. R. Nott and J. F. Brady. Pressure-driven flow of suspensions: simulation and theory. *J. Fluid Mech.*, 275:157–199, 1994.

[50] J. Delour O. Pouliquen and S. B. Savage. Fingering in granular flows. *Nature*, 386:816–817, 1997.

[51] F. Melo P. B. Umbanhowar and H. L. Swinney. Localized excitations in a vertically vibrated granular layer. *Nature*, 382:793, 1996.

[52] M. J. Miksis P. G. López and S. G. Bankoff. Inertial effects on contact line instability in the coating of a dry inclined plane. *Phys. Fluids*, 9:2177, 1997.

[53] E. Herbolzheimer P. N. Segré and P. M. Chaikin. Long ranged correlations in sedimentation. *Phys. Rev. Lett.*, 79:2574, 1997.

[54] O. Pouliquen. On the shape of granular fronts down rough inclined planes. *Phys. Fluids*, 11:1956–1958, 1999.

[55] O. Pouliquen. Scaling laws in granular flows down rough inclined planes. *Phys. Fluids*, 11:542–548, 1999.

[56] J. F. Richardson and W. N. Zaki. Sedimentation and fluidization: Part i. *Trans. Inst. Chem. Eng*, 32:35–53, 1954.

[57] S. A. Safran S. M. Troian, E. Herbolzheimer and J. F. Joanny. Fingering instabilities of driven spreading films. *Europhys. Lett*, 10:25, 1989.

[58] S. B. Savage and C. K. K. Lun. Particle size segregation in inclined chute flow of dry cohesionless granular solids. *J. Fluid Mech.*, 189:311–335, 1988.

[59] L. W. Schwartz. Viscous flows down an inclined plane: Instability and finger formation. *Phys. Fluids A*, 18:443, 1989.

[60] N. Silvi and E. B. Dussan V. On the rewetting of an inclined solid surface by a liquid. *Phys. Fluids*, 28:5, 1985.

[61] M. A. Spaid and G. M. Homsy. Stability of newtonian and viscoelastic dynamic contact angles. *Phys. Fluids*, 8:460, 1996.

[62] J. W. Vallance. *Experimental and field studies related to the behavior of granular mass flows and the characteristics of their deposits.* PhD thesis, Michigan Technol. Univ., 1994.